Preliminary Design and Evaluation of Radial Inflow Turbines for a Small-scale Open Cycle Rocket Engine

Matthias Christiaens

Delft University of Technology

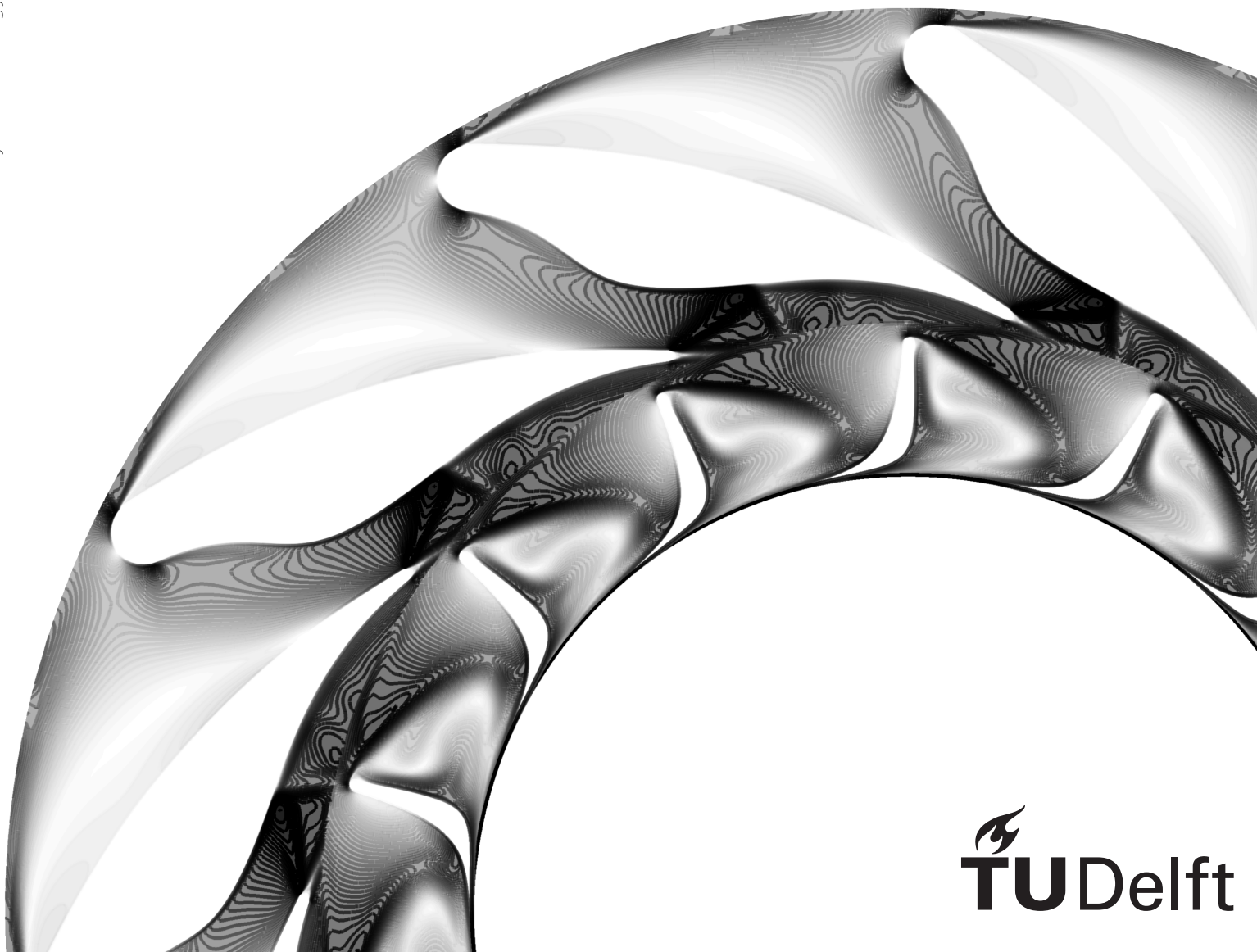

TU Delft

Preliminary Design and Evaluation of Radial Inflow Turbines for a Small-scale Open Cycle Rocket Engine

by

Matthias Christiaens

to obtain the degree of Master of Science

at the Delft University of Technology,

to be defended publicly on Monday, October 13th, 2025 at 14:00.

Student number:	4881826	
Thesis committee:	Dr. ir. M. Majer,	TU Delft, Daily Supervisor
	Dr. ir. M. Pini,	TU Delft, Responsible Supervisor
	Dr. ir. J. Bouwmeester	TU Delft, Chair
	Dr. A. Cervone	TU Delft, Examiner

An electronic version of this thesis is available at `http://repository.tudelft.nl/`.

TU Delft

Preface

This thesis marks the conclusion of my seven-year journey at TU Delft. During the second year of my Master's degree, I had the opportunity to spend a year working full-time in the Stratos V team of Delft Aerospace Rocket Engineering (DARE), where I was responsible for developing the feed and pressurisation system of the rocket. It was an intense but rewarding year, giving me the chance to grow both technically and personally, and ultimately became the inspiration for this thesis topic.

I would like to thank my daily thesis supervisor, Matteo Majer, for his continued support and advice throughout the thesis. Despite the constantly changing scope of the thesis, Matteo has always maintained a positive outlook on the project, keeping me motivated.

I am also grateful to Jaap van der Lee and Ihor Tertyshnyi from Van der Lee Turbo Systems for their valuable guidance, expertise and technical advice during the project. Their input provided an important industry perspective and helped me steer the project in the right direction.

Last but not least, I would like to thank all my friends and family who kept me motivated throughout my studies and, particularly, the thesis.

Summary

The Stratos V rocket, developed by Delft Aerospace Rocket Engineering (DARE), is powered by the Firebolt liquid rocket engine, using a pressure-fed cycle. While mechanically simple, this cycle scales poorly to higher thrust levels due to heavy tanks and complex pressurisation systems. Pump-fed cycles resolve these limitations: electric pump-fed systems are operationally simple but remain constrained by battery mass and scalability, whereas turbopumps provide higher performance. Radial inflow turbines (RITs) are of particular interest for small-scale open-cycle engines such as Firebolt, as they may be able to achieve high pressure ratios in a single stage, leading to high-power-density designs.

The objective of this thesis was to investigate whether a radial inflow turbine can be a suitable solution for a small-scale open-cycle rocket engine and whether it can provide a performance advantage compared to a typical axial turbine, in the context of a hypothetical Stratos VI rocket.

A methodology combining system-level trade studies, reduced-order turbine models, and CFD was applied. Candidate rockets were sized for different cycles, based on which turbine requirements were derived, after which vaned and vaneless RITs were designed in AxStream and evaluated using steady-state RANS simulations in Ansys CFX at nominal and off-design conditions. An axial turbine was also designed for comparison.

Both RITs satisfied the 24 kW shaft power requirement, with mass flows well below the 222 g/s limit needed to outperform the electric pump-fed rocket. As a result, the turbopump-fed rocket outperformed both pressure-fed and electric pump-fed configurations, though the margin over the latter was modest. However, CFD simulations revealed efficiencies far lower than predicted by AxStream, dominated by outlet swirl and flow separation losses due to mismatched stator and rotor flow angles.

At nominal conditions, the vaneless turbine achieved a lower mass flow of 72 g/s and higher thermodynamic power of 31 kW, benefiting from a larger rotor and higher tip speeds. The vaned turbine performed worse, at 104 g/s and 24 kW, but offers greater potential for optimisation through a redesigned stator with better flow guidance. A preliminary axial turbine design suggested significantly higher efficiency due to more favourable duty coefficients, but this was not validated against CFD. Off-design simulations confirmed the sensitivity of RITs to ambient pressure, reaching outlet Mach numbers up to 3.0 at near-vacuum conditions. The vaned turbine's efficiency and power increased, while the vaneless turbine gained power but lost efficiency, necessitating a choked nozzle to maintain constant performance throughout the flight. Simulations at double the shaft speed attained almost double the efficiency and power, indicating the need for higher tip speeds.

In conclusion, RITs are a viable solution for powering the Firebolt engine in Stratos VI, having met the power and mass flow requirements and enabling higher performance than both pressure-fed and electric pump-fed architectures. Yet, their advantages at this scale are not clear-cut. Axial turbines remain attractive due to their design flexibility, ease of manufacturing, staging potential, and extensive heritage. Further optimisation and CFD are needed to identify the most suitable architecture for DARE.

Contents

List of Figures

List of Symbols and Abbreviations

Symbols

Symbol	Definition
b	Blade height [mm]
C	Battery C-rating [-]
C	Flow velocity [m/s]
C_θ	Circumferential flow velocity [m/s]
C_0	Isentropic spouting velocity [m/s]
C_p	Specific heat at constant pressure [J/(kg K)]
c	Blade chord [mm]
D	Diameter [mm]
D	Depth of discharge [-]
h	Enthalpy [J/kg]
I	Current [A]
I_{sp}	Specific impulse [s]
k	Thermal conductivity [W/(cm K)]
K_V	Motor velocity constant [rpm/V]
L_{ax}	Axial rotor length [mm]
M	Mach number [-]
M	Molar weight [g/mol]
m	Mass [kg]
$\dot{m}$	Mass flow [kg/s]
N	Number of batteries [-]
N_S	Specific speed [-]
N_θ	Swirl coefficient [-]
P	Power [W]
p	Pressure [bar]
Pr	Prandtl number [-]
Q	Battery capacity [Ah]
Q	Volumetric flow rate [m^3/s]
Q	Q-criterion [$1/s^2$]
R	Resistance [Ω]
R	Specific gas constant [J/(kg K)]
S	Number of battery cells in series [-]
S_{ij}	Strain rate tensor [1/s]
SF	Safety factor [-]

Symbol	Definition
T	Temperature [K]
U	Tip speed [m/s]
V	Voltage [V]
β	Metal angle [deg]
η	Efficiency [-]
γ	Specific heat ratio [-]
μ	Viscosity [cP]
ϕ	Flow coefficient [-]
ψ	Work coefficient [-]
ρ	Density [kg/m^3]
Ω_{ij}	Vorticity rate tensor [1/s]
ω	Rotational velocity (shaft speed) [rpm]

Abbreviations

Abbreviation	Definition
BEP	Best Efficiency Point
BLDC	Brushless Direct Current Motor
CDV	Convergent Divergent Vaned
CFD	Computational Fluid Dynamics
CG	Center of Gravity
COPV	Composite Overwrapped Pressure Vessel
DARE	Delft Aerospace Rocket Engineering
DLR	Deutsches Zentrum für Luft- und Raumfahrt
ESC	Electronic Speed Controller
FA	Full Admission
FE	Full Emission
FOSU	Factor Of Safety Ultimate
FOSY	Factor Of Safety Yield
FTP	Fuel Turbopump
GG	Gas Generator
GOx	Gaseous Oxygen
ITS	Inter-tank Structure
LD	Length-to-Diameter ratio [-]
LNG	Liquid Natural Gas
LOx	Liquid Oxygen
NPSH	Net Positive Suction Head [m]
OF	Oxidizer-to-Fuel ratio [-]
ORC	Organic Rankine Cycle
OTP	Oxidizer Turbopump

Abbreviation	Definition
PA	Partial Admission
PE	Partial Emission
PR	Pressure Ratio
RANS	Reynolds-averaged Navier Stokes
RC	Radio Control
R&D	Research and Development
RIT	Radial Inflow Turbine
ROT	Radial Outflow Turbine
SFC	Specific Fuel Consumption [g/(kW s)]
SSME	Space Shuttle Main Engine
SST	Shear Stress Transport
TEV	Tower Exit Velocity [m/s]

1

Introduction and Research Context

Rocket propulsion systems are central to the performance of launch vehicles. As such, the choice of propellant feed cycle has a major influence on the overall architecture and performance of the rocket. For Delft Aerospace Engineering (DARE), this choice has become increasingly more important, as the Stratos project has evolved to use a more advanced and complex bi-propellant liquid rocket engine and continues to seek increased performance, ultimately leading to the development of turbomachinery.

This chapter provides the research context for this thesis and explains the necessity for turbomachinery research within DARE. In Section 1.1, an introduction to DARE and the Stratos V project is given. This is followed by a brief overview of the current architecture and its limitations in Section 1.2. Section 1.3 explains how turbomachinery can provide a feasible solution to these limitations and how it can be implemented. Finally, Section 1.4 introduces the current state of turbomachinery development in DARE.

1.1. DARE and Stratos V

Delft Aerospace Rocket Engineering (DARE), founded in 2001, is a student rocketry organisation at TU Delft focused on the design and testing of advanced rocketry systems, providing hands-on engineering experience [1].

Stratos, DARE's flagship project, reflects these efforts by designing high-performance rockets. With the overarching goal of *"Breaking Boundaries"*, Stratos has always aimed higher, breaking altitude records with Stratos I and II+, powered by a solid and hybrid[1] rocket engine respectively [1].

In parallel, Project Sparrow was founded in 2020 in an effort to explore new advanced propulsion technologies. Within two years, the team designed and successfully tested Firebolt, a regeneratively cooled, 3D-printed liquid rocket engine operating on Liquid Oxygen (LOx) and an 80/20 ethanol-water mixture, producing up to 10 kN of thrust at a 30 bar chamber pressure.

Following these achievements and the cancellation of Stratos IV, the Firebolt engine became the foundation of a new, liquid bi-propellant rocket: Stratos V. Whereas previous rockets aimed for increasingly higher altitudes and breaking records, Stratos V's main goal[2] is to demonstrate reusability

[1] A hybrid rocket engine is powered by both a solid propellant (typically the fuel) and a liquid propellant (typically the oxidizer), as opposed to fully solid or liquid propellants.

[2] At the time of writing.

by recovering the rocket with a parachute and re-launching it. This is partly made possible by the Firebolt rocket engine, which allows for multiple hotfires with minimal refurbishment, as opposed to most solid or hybrid rocket engines.

Despite this shift in focus to technology demonstration, the long-term plan for future iterations of the rocket is still to reach higher. As became clear during the design phase, the current architecture does not scale well for higher altitudes and more powerful engines. This is primarily due to the use of the pressure-fed cycle, as explained in Section 1.2, which limits the design in several significant ways.

1.2. Limitations of the Pressure-Fed Cycle

A rocket engine cycle is the method by which the propellants are fed to a rocket engine. The current design of Stratos V uses a pressure-fed cycle, in which the propellant tanks are pressurized by an inert gas (in this case Helium) to a pressure higher than the chamber pressure, allowing the propellant to flow from the tanks to the chamber. While a relatively simple system on the surface, it has some significant drawbacks. In fact, while Firebolt was initially designed for a 50 bar chamber pressure, providing ~15 kN of thrust, the team has decided to limit it to 30 bar and ~10 kN due to these limitations, which are as follows.

Due to the high pressure, in the order of 40-45 bar, the propellant tanks are required to be very thick and heavy. Additionally, design and manufacturing become more challenging because of the need for high-quality welds. Longitudinal welds are generally avoided, instead requiring seamless cylinders which are difficult to source or manufacture in the required dimensions [2]. Unfortunately, DARE does not have the capability to manufacture lightweight, high-pressure and cryogenic composite tanks and is therefore limited to using heavier, fully metallic tanks.

To supply the inert pressurant gas, a separate high-pressure tank is required. The first design iteration of Stratos V used a 40-litre composite overwrapped pressure vessel (COPV) from Safer Cylinders; the largest reasonably priced, commercially available option [2]. Despite this, the tank's volume still limited the rocket's burntime. With a dry mass of 18.5 kg and a length of 1.4 m, the COPV significantly impacted the rocket's efficiency and design [3]. To maximize gas storage, the tank operated at 400 bar, requiring an expensive gas booster system and introducing leakage and safety concerns.

In addition, the weight of the gas is not negligible. Using Nitrogen as pressurant, the pressurant mass inside the COPV at lift-off amounts to approximately 18.0 kg. This excludes the ullage gas inside the propellant tanks. Helium (Stratos V's pressurant of choice) is more efficient and lightweight, resulting in a pressurant mass of 2.6 kg, but has its own drawbacks, such as significantly higher cost and leakage rates.

Lastly, this system requires a large and complex pressurization system, using heavy pressure regulators and active control.

At the higher engine chamber pressure of 50 bar, many of these limitations are further amplified and, while a higher chamber pressure increases the efficiency of rocket engines, the mass increase of the system far outweighs the benefits for this particular rocket [4], [5].

1.3. Turbomachinery

A possible solution to the limitations described in Section 1.2 is the pump-fed cycle. In this cycle, propellant is pumped from low-pressure tanks to the high-pressure combustion chamber by increasing the pressure of the propellant at the discharge side of the pump.

Historically, most pump-fed rocket engines have used turbopumps, in which the pump is driven by a turbine [6]. This turbine can be powered in various ways, corresponding to different rocket engine cycles.

Robert H. Goddard's first turbopump featured two turbines (one per pump), placed partially in the engine's exhaust stream [6]. Due to the high temperature of the exhaust gases, the steel turbine blades melted. His solution was the gas generator (GG) cycle, also called the open cycle: a smaller "rocket engine" produces high-energy warm gas for the turbines, keeping the temperature low enough to avoid melting of the turbine [6]. After passing through the turbine, the gas is bled off outboard.

Other rocket cycles exist which can increase the efficiency, power or simplicity of the system, such as:

- **Tap-off cycle:** hot gas is tapped off from the main combustion chamber instead of a GG [7].
- **Staged combustion cycle:** turbine exhaust is injected into the main combustion chamber instead of being discarded. As this forms a closed circuit, this cycle is called a closed cycle. In this case, the GG is called a preburner.
- **Expander cycle:** propellant, heated by the combustion chamber's regenerative cooling circuit, drives the turbine[3]. The turbine exhaust can be discarded, or injected into the main chamber, resulting in an open or closed cycle.

Recent advancements in battery and electric motor technologies have led to the electric pump-fed cycle, where an electric motor powers the pumps. This may lead to a less complex and possibly more reliable system, a simpler start-up sequence and easier throttling by changing the motor's rotational speed (in case of a dual shaft system). A prominent example is Rocket Lab's Rutherford engine, which is the first battery-powered, electric pump-fed engine to have flown [8].

1.4. Turbomachinery in DARE

In 2021, a small DARE team, initially part of project Sparrow, recognized the aforementioned limitations of pressure-fed systems and began developing an electric fuel pump. Its design is detailed in Subsection 2.6.1. The pump has been successfully demonstrated with water at lower power, paving the way for further turbomachinery development in DARE.

However, more work is needed to achieve a flight-ready system. A new design revision is necessary to improve the performance and reliability, and a new pump needs to be designed for LOx, which poses additional challenges related to its cryogenic and oxidizing properties. Additionally, the electric drive system needs to be upgraded in order to reach the pumps' design point.

During the development, the limitations of electric-powered pumps became clear, particularly the availability of compact, high-power electric motors and the need for large battery packs. Therefore, it

[3] Typically, this involves heating a cryogenic propellant enough to change it to its gaseous or supercritical state.

was recommended to commence the development of turbine-powered propellant pumps to achieve a high-performance, yet efficient and compact propulsion system.

To support this, a literature review was performed, with the goal of identifying the key design elements of small-scale rocket engine turbopumps, and to provide a foundation for the development of reliable and efficient turbine-powered pumps for the DARE Stratos rocket family. This review is summarised in Chapter 2.

2

Literature Review

A literature review is performed, which aims to identify key design elements of small-scale rocket engine turbopumps and lay the groundwork for reliable and efficient turbine-powered pumps for the DARE Stratos rocket family. Emphasis is placed on turbines and turbopump architectures commonly used in rocket engine turbopumps, for small-scale applications in particular, while other elements such as pumps and mechanical aspects are briefly discussed to provide additional context.

In Section 2.1, different configurations of turbopump assemblies are introduced. Section 2.2 and Section 2.3 go into more detail on pumps and turbines, respectively. Section 2.4 explains the decision-making of the turbopump's rotational velocity. Section 2.5 introduces the gas generator and its influence on the turbine design. Finally, several case studies are presented in Section 2.6.

2.1. Turbopump Configurations

Turbopumps can come in many forms, whether it be electric-driven, turbine-driven, single-shaft, multi-shaft, etc. This section introduces some of the more common turbopump configurations and their advantages and disadvantages.

2.1.1. Electric and Turbine Driven Pumps

As mentioned in Chapter 1, historically most rocket engine pumps have been driven by a turbine, whereas pumps driven by electric motors have seen a surge in popularity in recent times. Both architectures have their own distinct advantages and disadvantages and are suitable for different design points. A simplified schematic overview of single-shaft electric pump-fed and gas generator cycle engines is shown in Figure 2.1.

One of the main advantages of electric pumps is their relative simplicity and flexibility. From an operational standpoint, the startup and shutdown of an electric pump-fed engine are relatively straightforward, as the pumps can be started on demand and regulated to any desired rotational speed. The startup sequence of a turbopump-fed engine is significantly more complicated, as it typically requires a spinstart of the TPA to achieve some initial fluid flow to the gas generator or preburner, which is then ignited to drive the turbine and supply power to the pumps[1]. The development of a start-up sequence is a non-trivial problem and requires a significant amount of analysis and experimentation,

[1] Turbopumps may be bootstrapped as well, which has its own complications.

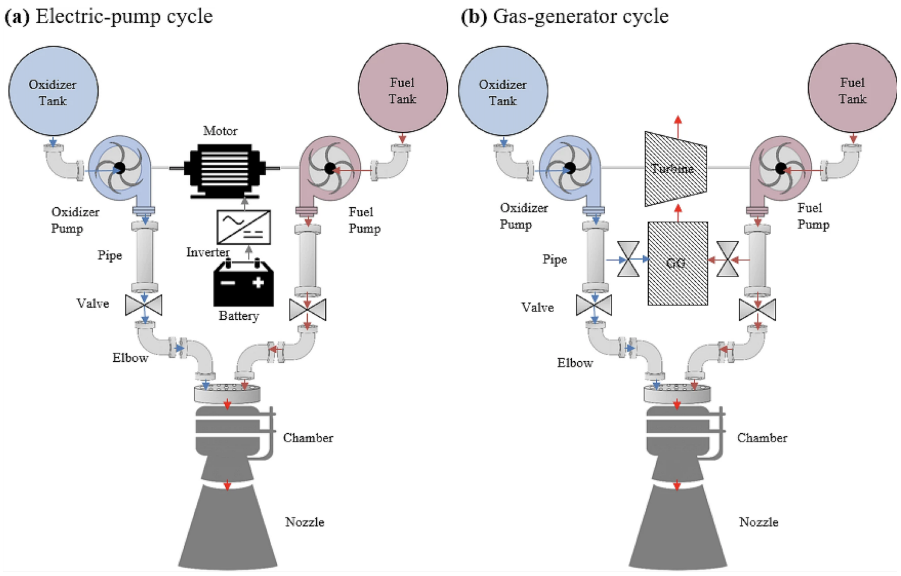

Figure 2.1: Schematic overview of rocket engine cycles. a) Single-shaft electric pump cycle, b) single-shaft gas generator cycle. Source: [9].

particularly in closed-cycle engines.

Throttling and (active) flow regulation are also much simpler in electric-driven pumps, where the rotational speed of the motor can be easily controlled. This is not the case for (GG cycle) turbine-driven pumps, where throttle valves are used to regulate the GG and thrust chamber mass flows. The GG itself is fed by the same pumps it is powering, resulting in a coupled system that requires careful tuning.

Another significant difference is the influence of the engine cycle on the mass of the rocket. The drive systems of both electric pumps and turbopumps come with a certain fixed mass and burntime-dependent mass. In electric pump systems, the electric motor, electronic speed controller (ESC) and battery management system (i.e. the electronics that monitor and control battery operation) are components with a fixed mass, as they are independent of the burntime, while the required battery mass does scale with burntime. The batteries maintain a constant mass throughout the burn duration and, once depleted, essentially become dead weight. It is for this reason that Rocket Lab's Electron launch vehicle ejects some of its used battery packs during take-off, allowing it to gain some performance [10].

In the case of turbopumps, the turbine, gas generator and control valves have a fixed mass. However, open-cycle engines consume a portion of the total engine mass flow to drive the turbines, which negatively affects engine performance. A common metric for rocket engine efficiency is the specific impulse, or I_{sp}, which represents the total propellant consumption (mass flow, $\dot{m}$) for a given thrust level (F_T), see Equation 2.1. The increased engine mass flow therefore results in a lower engine I_{sp} compared to electric pump-fed engines. The total propellant mass consumed by the turbines increases proportionally with burntime. Unlike batteries, this propellant mass is automatically expelled overboard, reducing the vehicle's total mass as the mission progresses.

$$I_{sp} = \frac{F_T}{g_0 \dot{m}} \tag{2.1}$$

The solution to the reduced I_{sp} of open cycle engines is to use a closed cycle, such as the staged combustion or expander cycle, where the propellants driving the turbine are injected back into the combustion chamber. Open cycles generally increase the complexity significantly and are not recommended for a student-developed rocket engine.

Combined with the high power requirements for large TPAs, this means electric pump-fed engines are not very scalable. It is most likely for this reason that Rocket Lab decided to switch from an electric pump-fed cycle to a staged combustion cycle for their more powerful Archimedes engines [10].

2.1.2. Turbopump Arrangements

Many different arrangements exist for turbopump assemblies, each with their own set of advantages and disadvantages, the most common and relevant ones of which are discussed here. An overview of common shaft configurations is shown in Figure 2.2.

In rocket engines where a different shaft speed is desired for each pump to achieve maximum efficiency, e.g. in case of considerably different densities and/or flow rates, it is common to use a dual shaft system, such as the oxidizer-rich staged combustion cycle Rocketdyne RS-25 Space Shuttle Main Engine (SSME) and gas generator cycle Rocketdyne RS-68 (a simplified version of the RS-25) [11]. In this case, each pump is driven by its own turbine, which in turn can each be powered by either one common gas generator or two separate ones. This is also the case in full-flow staged combustion engines, such as the SpaceX Raptor engine. Alternatively, geared pumps can be used, in which a gearbox allows for a difference in shaft speed between both pumps. This increases the complexity of the system and adds additional failure points.

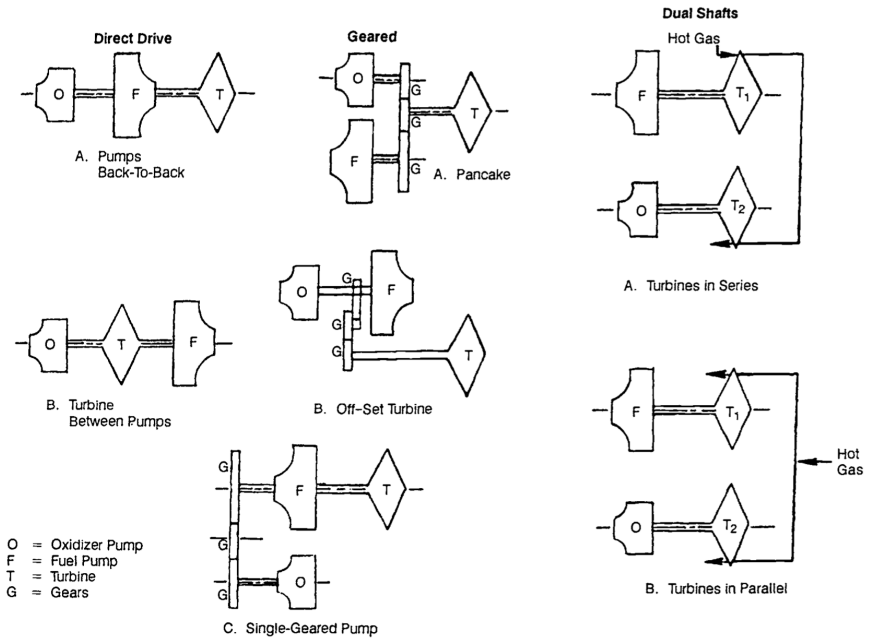

Figure 2.2: Different turbopump assembly configurations. Source: [4].

Similar configurations apply to electric pumps, where each pump can be powered by separate motors or by a singular motor, with optional gearing. That being said, using separate motors for each pump allows for an operational advantage: the ability to easily and accurately control the mass flows individually without the need for throttle valves, as well as easier testing of each pump as a stand-alone unit. Additionally, with the lack of affordable high-power commercial off-the-shelf (COTS) brushless direct current (BLDC) motors and electric speed controllers (ESC), a dual shaft system would be recommended for the DARE's electric pumps, as the lower power requirement for separate motors makes it easier to find an acceptable solution [12].

In a single shaft system, there are three main ways in which the turbine and pumps can be arranged, two of which are shown in Figure 2.2 [4]. In the first configuration, the turbine is placed between the oxidizer and fuel pump. One of the advantages of this system is the separation of the fuel and oxidizer, reducing the risk of inter-propellant leakage (this same advantage is true for dual shaft systems). This does mean that the turbine needs to be sealed off from both the fuel and oxidizer. Another advantage is that both propellants can directly enter the pumps axially and do not require additional considerations to straighten the flow path. In the two other configurations, sometimes called direct-drive, the turbine is located at one end of the shaft, followed by either the oxidizer pump and then the fuel pump, or vice versa. The latter configuration would be preferred for the DARE turbopump, as it reduces the temperature difference between the turbine and the neighbouring pump, since the ethanol fuel is kept at room temperature while the LOx oxidizer is cryogenic.

It is important to take into account the possible leakage from the pumps to the turbine. For example, in the case of a fuel-rich gas generator or preburner, a small amount of leakage from the fuel pump to the turbine can be tolerated, as it will only slightly lower the temperature of the fuel-rich mixture, which the increased mass flow may compensate for. However, leakage from the fuel pump to an oxidizer-rich preburner can have larger implications, as this will shift the oxidizer-to-fuel ratio in the turbine towards a more stoichiometric ratio, increasing the temperature of the gaseous oxygen (GOx) and potentially significantly increasing the shaft power, which can be catastrophic in some cases. The same goes for leakage from an oxidizer pump to a fuel-rich GG/preburner.

2.1.3. Staging

It is common for rocket engine turbopumps to employ multi-stage systems (not to be confused with staged combustion), where the fluids pass through multiple turbines or pumps in series [7].

For turbines, this allows more energy to be extracted from the gas and can increase the efficiency, or reduce the required diameter. In rocket engine turbopumps, this is most commonly done with axial turbines, as the length of the assembly can be relatively easily extended to integrate more stages. Radial turbines are more difficult to stage and are restricted by the diameter of the assembly. When a cantilever radial turbine (see Subsection 2.3.1) is used, multiple blade rows can be integrated onto the same blisk. An example of this is the Ljungström turbine, shown in Figure 2.3, which features counter-rotating rotor stages [13]. A typical ("3D") radial inflow turbine, where the outlet flow is axial, is more difficult to stage due to its geometry. Alternatively, an axial stage can be placed in series with a radial stage.

Pumps also commonly employ multiple stages when a large head rise is needed. In some engines, these pump stages can be separated onto different shafts, typically operating at different speeds. In this case,

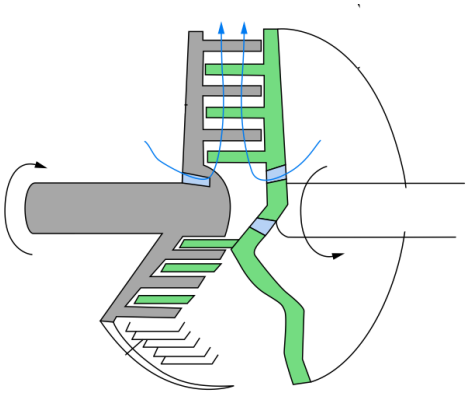

Figure 2.3: Diagram of a Ljungström turbine. Adapted from [13].

the separate low-speed "boost pumps" increase the available net positive suction head ($NPSH_A$) of the main pumps, allowing them to operate at a much higher RPM without cavitating [6]. This seems to be most common in staged combustion engines. An example of such systems is the fuel-rich staged combustion RS-25 engine, used in the Space Shuttle, which features four TPAs: a low-pressure and high-pressure one, for each propellant [14].

In staged combustion engines, additional stages are also often used in the form of "kick pumps" (sometimes also called "boost pumps", not to be confused with the aforementioned type of boost pumps) and increase the head of only a portion of the propellant flow, after it has passed through the main pump, in order to be used in the high-pressure preburner [6]. Less commonly, these can be powered by separate turbines.

The main disadvantage of multi-stage systems is the increase in mass and complexity.

2.2. Centrifugal Pumps

Arguably the most important part of the turbopump, the pumps produce the mass flow and pressure increase of the propellants. Several types exist, of which centrifugal pumps are the most prevalent in rocket engine turbopumps. They generate pressure by accelerating the flow radially outwards using a rotating impeller, after which it is decelerated in a volute and diffuser [15].

As seen in the Baljé chart, Figure 2.4, centrifugal pumps typically operate in the lower range of specific speeds of roughly 10-150 (imperial units) or 4-60 (metric units) and are commonly used for low flow rate and high head rise applications, making them well-suited for rocket engine turbopumps. Staging is possible but is typically avoided as it requires a more complicated assembly with an inter-stage flow passage, resulting in an overall less compact design.

Because of their suitability for low specific speeds, the simplicity of a single stage and the extensive use and documentation of centrifugal pump designs in rocket engines, the DARE pump was also chosen to be of the centrifugal type.

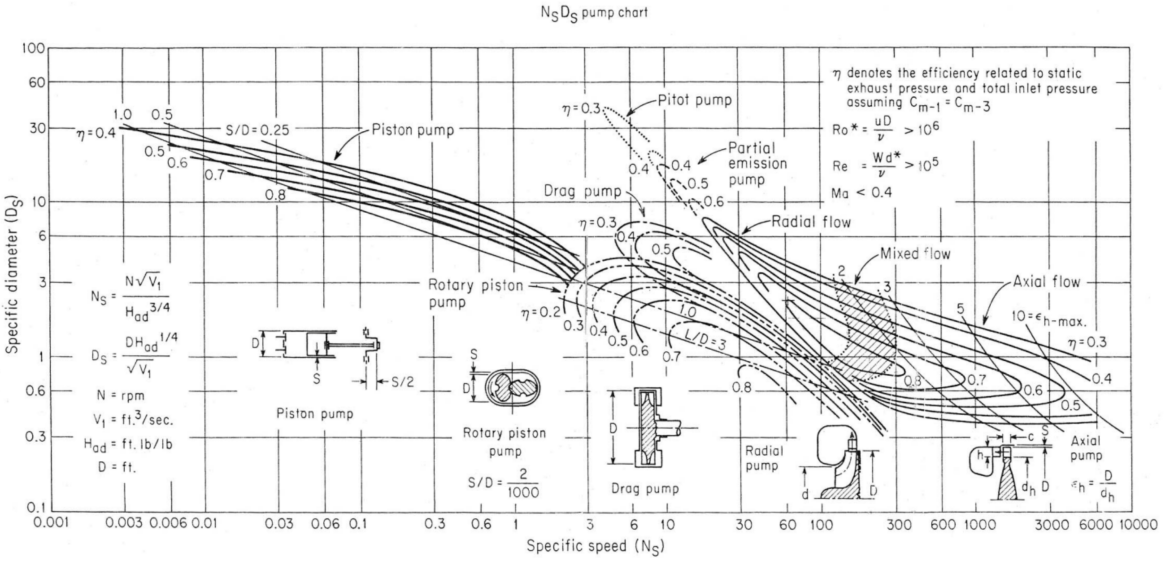

Figure 2.4: Pump Baljé diagram. Source: [16].

2.3. Turbines

Similarly to pumps, many different turbine designs exist. Some of these design options and elements are introduced in this section. A Baljé chart of different turbine types is shown in Figure 2.5.

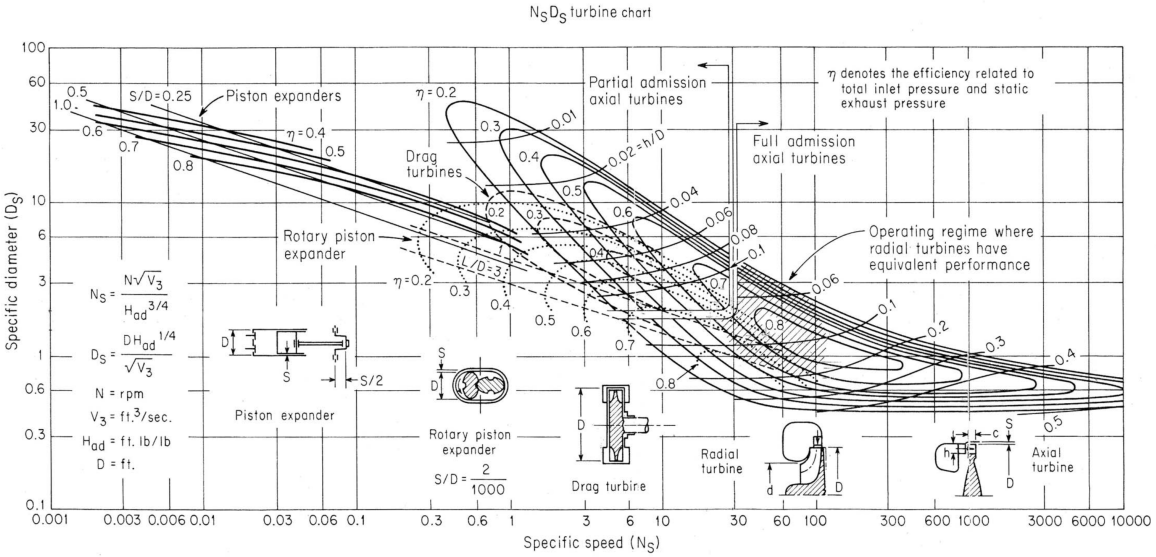

Figure 2.5: Turbine Baljé diagram. Source: [16].

2.3.1. Radial Turbines

As the name implies, radial turbines are characterized by the radial flow of the gas in the turbine.

Two main types of radial turbines can be distinguished: radial inflow turbines (RIT) and radial outflow turbines (ROT), examples of which are seen in Figure 2.6 and Figure 2.7. RITs are a common choice in automotive turbocharger systems and some aircraft engines [17]. Additionally, they are gaining traction in waste heat recovery systems, particularly those using the Organic Rankine Cycle (ORC).

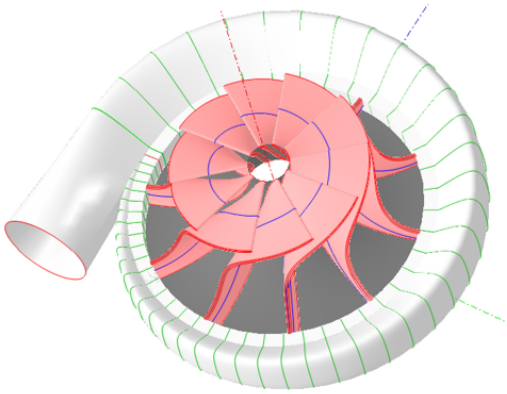

Figure 2.6: Radial inflow turbine and volute. Source: [18]

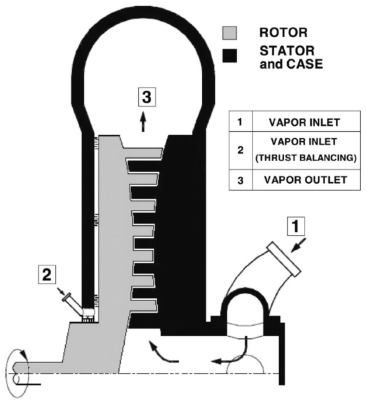

Figure 2.7: Radial outflow turbine. Source: [19]

Advantages of RITs include a high expansion ratio and high work produced by a single-stage design. According to Boyce [13, p. 359-361], RITs can produce as much work as two or more axial turbine stages due to the higher tip speeds. Baljé [16, p. 96] also identifies a specific speed regime of roughly 30-100 (imperial units) or 12-40 where radial turbines can provide equivalent performance to axial turbines, as indicated in Figure 2.5. In partial admission radial turbines, however, the efficiency is likely to be reduced due to pumping losses. NASA [7, p. 44] on the other hand, indicates a slightly lower efficiency of RITs compared to single-stage impulse and 50% reaction turbines, as seen in Figure 2.8 (a).

RITs can have a more compact and lightweight form factor compared to axial turbines, depending on the design point [20]. Additionally, they are sometimes considered to be more affordable and easier to manufacture, as is made clear by large-scale automotive turbocharger production. NASA [7, p. 44], however, claims RITs to be heavier than axial turbines for the same ratio of turbine pitchline velocity to isentropic spouting velocity (U/C_o).

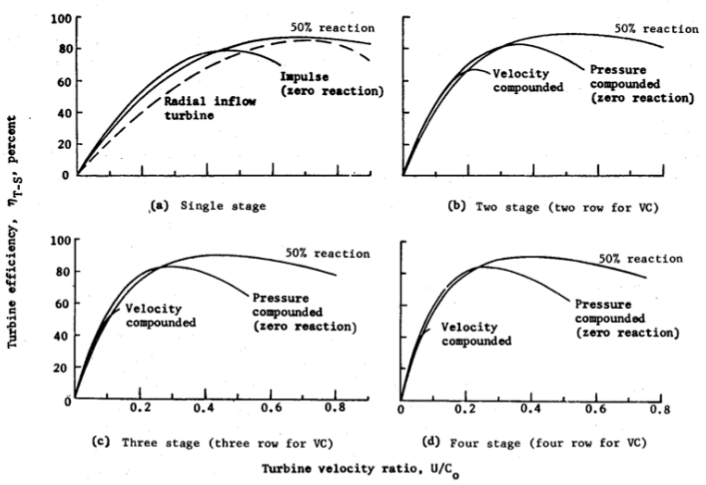

Figure 2.8: Efficiency versus velocity ratio for various turbine designs and stage numbers. Source: [7].

RITs seem to be relatively insensitive to off-design conditions and are especially suited for use with variable stators, as the total efficiency remains high with varying flow rates, posing a significant advantage in applications requiring high efficiency at different operating points, such as ORC plants [17]. On top of that, the implementation of variable geometry stators in RITs is likely mechanically less

complicated compared to axial turbines.

There are two common ways radial turbines are designed: planar/cantilever designs, and "3D" radial turbines [13], [21]. Radial inflow turbines are typically of the 3D type, which feature thin, curved blades and discharge the gas axially, as seen in Figure 2.6, meaning the flow turns 90°inside the turbine. Cantilever turbines feature blades akin to axial impulse turbine blades and are typically two-dimensional. Cantilever RITs are much less common. An example of this is Mario Hernández's turbine, the design of which is discussed in Subsection 2.6.2. They can have several advantages, such as ease of manufacturing due to their planar design, and the possibility of adding multiple turbine stages onto the same blisk, as explained in Subsection 2.1.3. This increases the amount of power extracted from the turbine, without requiring additional parts and while maintaining a very compact system. However, they suffer from lower efficiencies and flutter issues, and have a higher moment of inertia, resulting in a structural disadvantage.

RITs may be configured with or without stator vanes/nozzles. The former configuration is being studied for ORC applications while the latter is commonly used in automotive turbochargers. While a stator stage results in a more complex system, it allows for better control of the flow angles at the rotor inlet and allows for the use of supersonic flow expansion for high pressure impulse turbine configurations.

Despite their possible advantages, RITs are not commonly used in rocket engine turbopumps, with only a handful of examples in small-lift launcher start-ups. This includes Latitude's open cycle engine, whose turbine is shown in Figure 2.9, and Astron Systems' hybrid electric expander cycle engine, whose turbine is shown in Figure 2.10 [22], [23], [24]. Another example is Mario Hernández Méndez' aforementioned turbine, but it is untested as of yet. Additionally, Sidereus Space Dynamics investigated the potential of RITs for their 25 [kN] open-cycle engine by comparing preliminary radial and axial turbine designs. The RIT was found to provide similar performance to the axial turbine, in a more compact form-factor [25].

More research is done on the use of RITs for expander cycle engines, where large mass flows and low pressure ratios and temperatures are available. Results are promising, showing potential increased efficiency and reduced pressure drop, compared to axial turbines. Specifically, Leto et al. [26, p. 742] predicted an increase in efficiency of up to 13 percentage points with a pressure drop reduction of 3.15 bar for the Aerojet Rocketdyne RL10A-3-3A engine, and up to 8 percentage points and 8.4 bar for the ArianeGroup Vinci engine.

ROTs do not seem to be nearly as common as RITs. Nonetheless, they have some advantages and use cases, where they can have higher efficiency and a wider operating range [27]. One such use-case being researched is ORC turbomachinery [28], [29]. ROTs typically have a cantilever design and are therefore often staged. No research or experimentation related to ROTs for rocket engine applications is found.

The motivation behind the lack of radial turbines is not well documented but may be attributed to the general lack of research and development into radial inflow turbines, causing engineers to stick to what is historically the most tried and tested. Additionally, the specific turbopump requirements of large rocket engines, such as specific speeds and pressure ratios, may cause the design to converge to axial turbines.

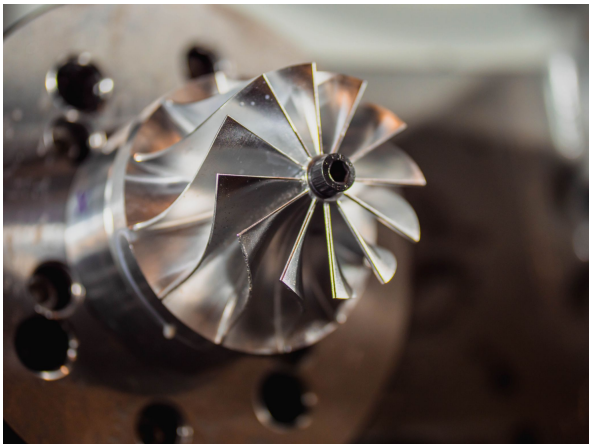

Figure 2.9: Latitude's Navier engine turbine. Source: [22].

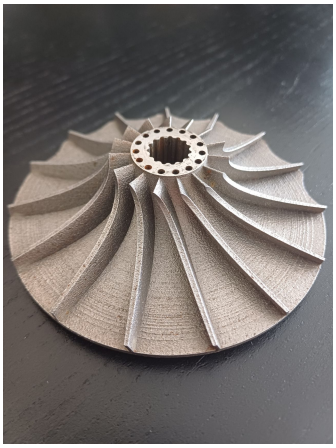

Figure 2.10: Astron Systems' RELIANT engine turbine. Source: [24].

2.3.2. Axial Turbine

In axial turbines, the gas enters and exits axially. Compared to radial turbines, axial turbines are much more prevalent in rocket turbopumps. In rocket engine turbopumps, the rotor disk and blades are typically manufactured as a single part, called a "blisk".

To maximise energy extraction from the gas and increase efficiency, multiple stages are often used. However, multi-staging of axial turbines significantly increases system complexity and should be avoided unless necessary or considered worth the added complexity.

Two main types of turbine stages are distinguished: impulse turbines and reaction turbines. In the latter, enthalpy is converted to kinetic energy upstream of the blades by expanding the flow (through the stators or nozzles) [30], [31]. Impulse turbines can be staged velocity-compounded, where all the fluid is expanded in the first-stage stator row, or pressure-compounded, where the pressure drops are distributed over the different stages' stators. A small degree of reaction is recommended in the other stages due to adverse pressure gradients.

In reaction turbines, some of the kinetic energy is produced in the rotor, caused by a pressure drop across the blades [30], [31]. The ratio of enthalpy drop in the rotor to the total enthalpy drop in the stage is called the stage reaction, R_s, and is typically limited to 25-50%. In multi-stage reaction turbines, the pressure drop is usually distributed roughly equally over the rotors.

A comparison of typical turbine stage efficiencies for different velocity ratios can be seen in Figure 2.8. Impulse turbines are more efficient at velocity ratios below around 0.4 and are common in systems with high energy fluids and high pressure ratios, such as (open cycle) rocket engines, where supersonic flows are achieved and high specific work can be reached. While pressure-compounded turbine stages typically have a higher efficiency, velocity-compounded turbine stages can come very close (as shown in Figure 2.8), with the benefit of being slightly more compact. According to NASA, [7, p. 26], "... GG and tapoff cycles generally incorporate two-row velocity-compounded turbines, and expander and staged-combustion cycles generally incorporate either two-stage pressure-compounded or reaction turbines".

2.3.3. Mixed Flow Turbine

Mixed flow turbines are an intermediate form of turbines and have operational points somewhere between axial and radial turbines. The flow enters diagonally and exits axially. They are not common in rocket engine turbopumps.

2.3.4. Turbine Stators

Turbines can make use of stators or nozzles to guide the flow before entering the rotor stage. These can be subsonic or supersonic, depending on the type of turbine. Open cycle designs, which commonly feature high pressure ratios, will often employ supersonic stator vanes or nozzles whereas expander or closed cycle designs, featuring lower pressure ratios but high mass flows, may opt for subsonic stators.

In some designs, it may be beneficial to reduce the amount of stators or nozzles, which may only be distributed along a section of the circumference, for example in case too short blade heights are required for a conventional design [30]. Such turbines are called partial admission (PA) turbines. An example of a PA turbine is the turbopump introduced in Subsection 2.6.2, which features only four nozzles. If this turbine were made full admission (FA), both the nozzles and blades would likely be too small to manufacture using the available methods and the clearance-to-blade height ratio may be too large, resulting in significant losses.

2.4. Shaft Speed

An important choice in the design of turbopumps is the shaft speed, or rotational velocity. This choice influences and is influenced by many factors, some of which are explained here.

2.4.1. Size

An important factor to consider is the influence of shaft speed on the size of the system, in particular the diameter. The Baljé pump chart in Figure 2.4 shows the relationship between the ratio of the pump rotor diameter to suction diameter, also known as the diameter coefficient or specific diameter D_S, and the pump specific speed N_S. Here it can be seen that, as N_S increases, D_S decreases. This is advantageous, as it results in a more compact design.

A similar relationship is found for turbines, as shown in Figure 2.5.

2.4.2. Efficiency

A significant effect of the shaft speed is the efficiency of the system. As the shaft speed affects different parts of the turbopump differently, no general statement can be made about whether or not a higher shaft speed will result in a more efficient design, as seen by the efficiency islands in the Baljé charts. Instead, this is very design dependent and will need to be investigated on a case-by-case basis.

While a higher specific speed pump can achieve higher hydraulic efficiencies, this is quickly negated by hydraulic and volumetric losses. This includes secondary losses such as disk friction losses and leakage losses [15].

Another form of losses due to high shaft speed is mechanical losses. As the shaft speed increases, the

surface speed of contacting elements increases. Examples of this are the dynamic seals, where the rotating and stationary surfaces may rub against each other, and the bearings. Therefore, an increased shaft speed will increase the friction and have a negative impact on mechanical efficiency.

Similarly for the turbine, the shaft speed influences many factors which can have varying effects on the turbine efficiency, such as tip clearance losses, the ratio between the rotor tip speed and isentropic spouting velocity (also called the velocity ratio) etc.

2.4.3. Mechanical Considerations

The primary mechanical consideration is the centrifugal loading of the pumps and turbines, which increases with the shaft speed. This is compensated for by the smaller required diameters.

High shaft speeds can also increase friction on rotating components such as seals and bearings. This not only reduces the mechanical efficiency, but also accelerates the wear on those components, shortening their lifespan. As a result, some parts need to be replaced more often, and additional bearing cooling may be necessary.

Finally, the shaft speed influences the axial thrust on the assembly, as it affects the diameters of the pumps and turbine.

2.4.4. Electric Drive Considerations

Another important factor is the electric drive system. As explained in Subsection 2.6.1, the choice of affordable COTS BLDC motors and ESCs is very limited, which influences the design space of the pumps. Even if a turbine-powered design is chosen, it is likely that early pump prototypes will be tested with electric motors. For this reason, it is beneficial to ensure the compatibility of the pumps with the existing electric drive systems.

While this poses a limiting factor to the design, this must be traded off against the significant advantage of being able to easily and safely test the pumps separately from the turbine. More operational advantages include the ability to more easily test the pumps at varying shaft speeds in order to generate pump curves.

2.4.5. Shaft Speed Selection

As the turbine and pumps have different requirements in terms of working fluids, mass flows and pressures, it is very likely that each component will have its own ideal shaft speed design point. However, for practical reasons, it is beneficial for all components to share the same shaft speed, especially in a single shaft system. Therefore, it is advantageous for the pumps and turbines to be designed simultaneously and to optimize the system as a whole. However, as the pumps are already being designed by DARE, the current shaft speed of 40 krpm can be used as a starting point.

2.5. Gas Generator

An essential element of a turbopump assembly is the gas generator or preburner (in the case of a staged combustion engine), which provides the warm gas for the turbine. Due to the high risk and complexity involved in closed cycles, it is recommended to use the most common and simplest cycle for Firebolt: the open (gas generator) cycle.

Designing a gas generator is an extensive topic on its own and falls outside the scope of this thesis and literature review. However, it is still important to consider the important design elements and their implications on the turbopump. This includes factors such as the oxidizer-to-fuel ratio and chamber pressure of the GG, which directly influence the exhaust gas temperature, gas composition and other critical properties. Because the turbine housing and blades/blisk are typically not actively cooled, it is important for the gas temperature to stay low enough. This can be achieved by running the gas generator (or preburner) either very fuel-rich or very oxygen-rich. In GG systems, the former option is nearly always used, as a high temperature oxidizer can be detrimental to the system without the use of highly specialised alloys.

2.6. Case Studies

This chapter presents the design of the DARE electric pump, as well as two turbopump designs. While many examples of turbopumps exist, a small selection is made of well-documented, recent designs made for similar requirements as the DARE Firebolt engine. The first design, DARE's current electric pump, is presented in Subsection 2.6.1. In Subsection 2.6.2, an amateur turbopump with similar specifications is shown. Finally, LUMEN, a liquid rocket engine demonstrator platform, is presented in Subsection 2.6.3.

2.6.1. DARE DTP-E74 Fuel Pump

The first example is DARE's own DTP-E74 fuel pump prototype. The design is documented in more detail in [5] and [12]. All information in this chapter is taken from these sources as well as from internal communications within the team unless specified otherwise. While this pump does not currently use a turbine, it is important to establish the context for the turbine, as well as outline its interfaces and specifications.

It is worth noting that at the time of writing, a new pump design is already being worked on. However, all information presented in this chapter only concerns the original iteration of the pump design, DTP-E74.

This design is shown in Figures 2.11-2.13. The pump was initially designed for the 50 bar version of the Firebolt engine and is powered by BLDC motor. To lower the risks during the first tests, along with the high power requirements and the fact that Firebolt is currently run at a lower chamber pressure, it was decided to lower the rotational velocity (also denominated as shaft speed) from 50 krpm to 30 krpm for the first iteration of the pump, while keeping the same geometry. This is because the impeller and volute were already manufactured when this decision was made.

Overview and Specifications The pump features a full emission (FE), closed centrifugal impeller and volute, 3D printed out of Titanium Ti 64. The parts were post-processed in-house, which proved to be non-ideal and resulted in precession and imbalance of the rotor, as well as large clearance requirements. This can be largely attributed to improper fixturing during machining, the high surface roughness of the printed parts, and the difficulty of machining Titanium.

The specifications for the pump, as originally designed, can be found in the first column of Table 2.1. The specifications for the pump at reduced shaft speed are presented in the second column. These are found by using the Affinity Laws, which relate pump or turbine parameters for geometrically similar designs.

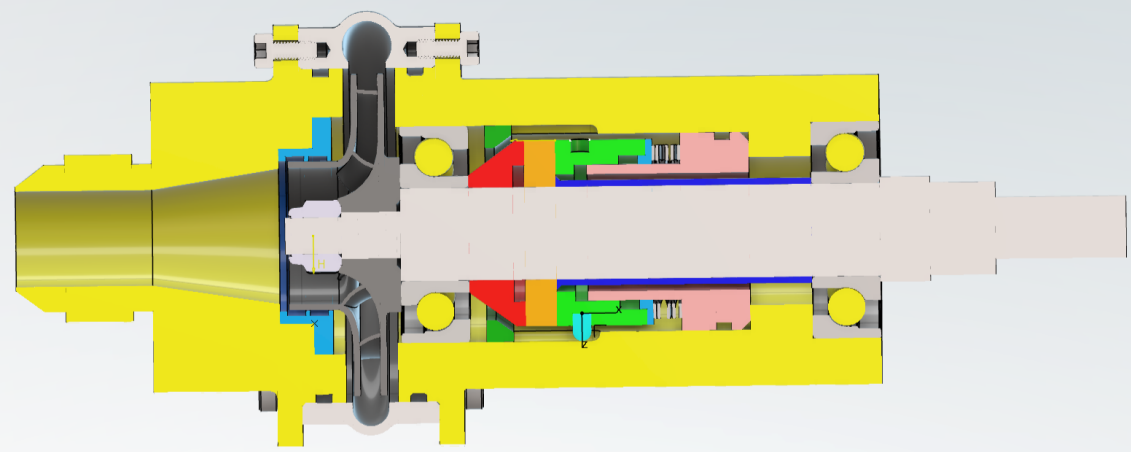

Figure 2.11: Current DARE fuel pump design. Image courtesy of DARE.

Figure 2.12: Assembled DARE fuel pump. Image courtesy of DARE.

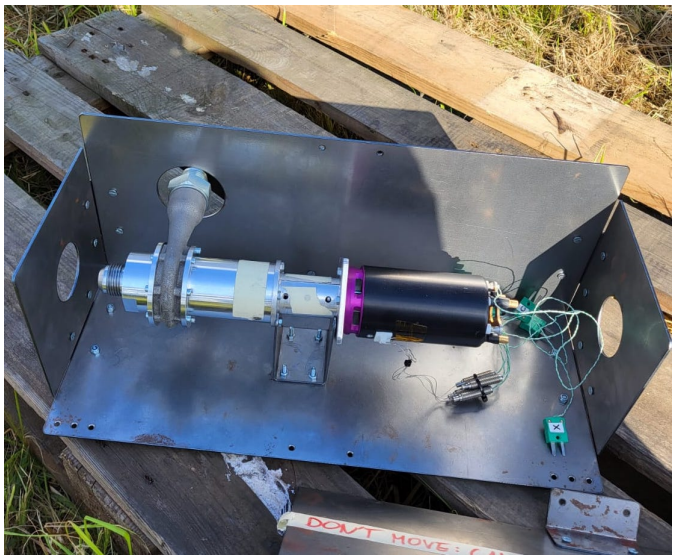

Figure 2.13: Assembled DARE fuel pump with motor and (partially disassembled) shrapnel box. Image courtesy of DARE.

These relations, in this case for identical diameters, are shown in Equation 2.2. For both cases, the specific speed of the pump, N_s, is 18.98 (metric units). Note that these are predicted parameters, based on results from empirical calculations, computational fluid dynamics simulations (CFD) or *CFturbo*[2] and do not necessarily represent the reality.

$$\frac{Q_1}{Q_2} = \frac{N_1}{N_2} \tag{2.2a}$$

$$\frac{H_1}{H_2} = \left(\frac{N_1}{N_2}\right)^2 \tag{2.2b}$$

$$\frac{p_1}{p_2} = \left(\frac{N_1}{N_2}\right)^3 \tag{2.2c}$$

[2]CFturbo is a turbomachinery design and analysis tool and was used to design the DARE fuel pump [5], [32].

where Q is volumetric flow rate, N is rotational velocity (or shaft speed), H is head and P is power.

Table 2.1: Specifications of the DARE DTP-E74 pump.

Property	As designed	Lower RPM	Unit
Shaft speed	50k	30k	[rpm]
Hydraulic Power	21.9	4.73	[kW]
Shaft Power	34.33	7.42	[kW]
Massflow	2.74	1.65	[kg/s]
Volumetric Flow	3.35	2.01	[l/s]
Inlet Pressure	8.42	~8	[bar]
Pressure Rise	65.43	23.54	[bar]
Head	815	293	[m]
Specific Speed (metric)	18.98	18.98	[-]

As can be seen in Table 2.1, the shaft power as designed is very high, which has serious implications on the system, such as the need for a much larger power pack, high current and/or voltage, and the need for a more capable and more expensive electronic speed controller (ESC). Due to the affinity laws, the shaft power required at a lower RPM is significantly lower, making it easier, cheaper and safer to perform the initial tests. This also presented DARE with the possibility to use a more affordable BLDC motor and ESC. Additionally, the lower RPM decreases the mechanical strain on the system. This includes lower friction between the ceramic surfaces of the mechanical seal, lower bearing friction and less radial force acting on the shaft and bearings due to an imbalance in the rotating assembly.

Nonetheless, the mechanical design of the system is made to be compatible with 50 krpm to ensure compatibility with future design iterations. The design can also relatively easily be adapted for use with cryogenic LOx.

Due to the new operating point of the Firebolt engine, the geometry of the fuel pump needs to be redesigned to provide the correct pressure rise and flow rate at the best efficiency point (BEP).

The approximate mass of the pump assembly is summarised in Table 2.2. This excludes the sensors or other hardware required.

Table 2.2: Approximate masses of the 30 rpm DARE pump assembly for a 30 [s] burntime[33], [34].

Component	Mass [kg]
Pump assembly	1.35
Motor	1.25
Batteries	1.06
ESC	0.52
Total	4.18

Electrical Drive System High-power electric motors and ESC are not affordable. Fortunately, the reduced RPM eases some of the requirements, allowing more affordable options to be used.

A BLDC by [33] is used, configured with a motor velocity constant K_V of 809.2 rpm/V. At 30 krpm, the

system is expected to run at 37.1 V and 200 A, ignoring any efficiencies. To control the motor, a Radio Control (RC) ESC was borrowed from [34] has been purchased.

At the time of writing, the DARE Turbomachinery team has not performed any analysis or preliminary design on the power delivery system of the pump at the 30 and 50 krpm design points. However, using the methods presented in [5] and [35], which are further explained in Subsection 4.3.2, an estimate can be made of the required battery pack, assuming a 30 s burntime.

In order to provide the required voltage and account for voltage sag, two 6S batteries can be used in series for the 30 krpm pump, amounting to an available voltage of 44.4 V. Each battery requires a capacity of 3898 mAh and a C-rating of 57 for the specified burntime. Two 6S Li-Po batteries from [36] are used, weighing 1.056 kg in total.

To run the pump at 50 krpm for 30 seconds, a combination of three 7S batteries in series times three in parallel is required. With a required 5273 mAh, nine batteries from [36] can be used, weighing 6.651 kg in total.

2.6.2. Mario Hernández Méndez' Turbopump

The second representative design is an "amateur" turbopump designed by Mario Hernández Méndez, who is a Pump Thermo-Mechanical Engineer at The Exploration Company and an advisor for the DARE Turbomachinery team (LinkedIn: [37]). His goal is to develop an open-source, low-cost and simple turbopump. This is done by cutting some corners to simplify the design - albeit with a reduction in efficiency or long-term reliability - and outsourcing manufacturing to affordable companies overseas. The design is shown in Figure 2.14.

Note that, as of writing, this design has not been tested, formally documented or officially published. As such, although Mario is an experienced turbomachinery engineer, this design should be considered with due scepticism, especially considering the unconventional design decisions. Nonetheless, it can serve as a source of inspiration for the turbopump design. All information here is sourced from X (formerly Twitter), a public Discord thread (r/rocketry) or directly from Mario unless specified otherwise [38].

Overview and Specifications Instead of fuel or oxidizer, the turbopump assembly (TPA) is designed to pump water due to its low cost, ease of use and safety for initial testing. The expected specifications of the TPA are listed in Table 2.3. Note that some of these specifications, such as specific speed and head, were derived from other properties and are subject to rounding errors. Additionally, due to the iterative nature of the design and its documentation, some values may be outdated. Unfortunately, no mass estimate is available for this system.

The TPA features a partial emission (PE) centrifugal impeller, also known as a Barske pump, with a specific speed of ~16.7 (metric definition), which greatly simplifies the geometry, allowing for affordable outsourced manufacturing. The impeller is open, which limits the axial thrust on the shaft.

The pump is driven by a partial admission (PA), supersonic 2D radial inflow turbine. Similarly to the pump, this turbine can be easily machined on a 3-axis CNC. Four supersonic nozzles each deliver approximately 10-11 g/s of warm gas. The turbine features an open back, allowing the hot gas to be discharged directly outwards during testing.

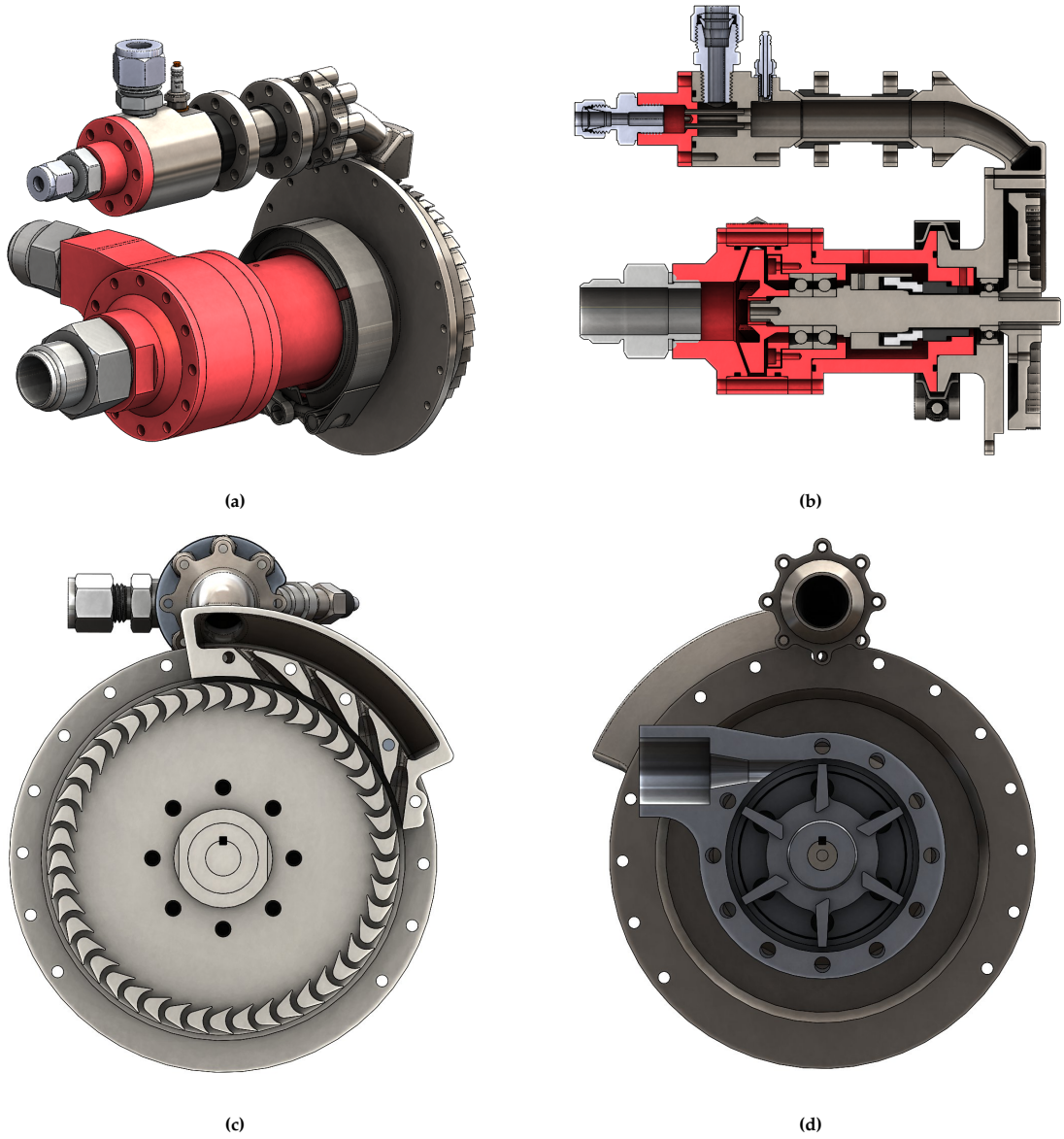

Figure 2.14: CAD renders of Mario's amateur turbopump design. a) Isometric view, b) Cross sectional view, c) Turbine cross sectional view, d) Pump side cross sectional view. Images courtesy of Mario Hernández Méndez [38]

The turbine is powered by a gas generator, which uses gaseous Oxygen (GOx) and gaseous Methane at a total mass flow of ~40 g/s. A shear coaxial injector is used, which is gaining popularity in amateur rocket engines because of its simplicity and good performance [39], [40]. The chamber pressure is 15 bar.

All parts indicated in red are CNC machined in Aluminium (unknown grade). The inlet and four nozzles of the turbine are 3D printed in 316L stainless steel. The turbine blisk is machined in 304 stainless steel and all remaining parts (excluding the COTS components, like seals and fittings) are a mix of 201 and 304 stainless steel, also CNC machined.

Rotordynamics analysis is performed using an open-source Python library called ROSS [41]. The TPA will not be balanced for the initial tests.

Table 2.3: Specifications of Mario's TPA.

Property	Value	Unit
Shaft Speed	25k	[rpm]
Shaft Power	12.4	[kW]
Pump Mass Flow	1.5	[kg/s]
Pump Volumetric Flow	1.5	[l/s]
Pump Inlet Pressure	3-4	[bar]
Pump Pressure Rise	22	[bar]
Pump Head	224	[m]
Pump Specific Speed	16.71	[-] (metric)
Turbine Mass Flow	41.3	[g/s]
Turbine Gas Temperature	900	[K]
Gas Generator Chamber Pressure	15	[bar]

Takeaways As mentioned before, while this design is meant as a simplified and affordable path to developing a turbopump, some inspiration can be drawn from this design. In particular, the main advantage of this design is its simplicity and manufacturability, as most parts can be machined and do not require high-performance materials, like Inconel. Notably, the radial inflow turbine is a promising alternative to the more common axial turbines and, in the case of the cantilever design used here, can be easier to manufacture than the axial type. This low-cost design also allows for rapid prototyping and is ideal for a research and development (R&D) style turbopump.

2.6.3. LUMEN

LUMEN (liquid upper stage demonstrator engine) is a liquid upper-stage rocket engine development project led by the German Aerospace Center, (Deutsches Zentrum für Luft- und Raumfahrt, DLR) [42]. Its goal is to provide a platform for research and demonstration of new technologies in a fully integrated testbed system. According to Traudt et al. [42, p. 1], the primary objectives of LUMEN are to be a "breadboard rocket engine for research purposes" and to have a "modular design to be able to test new components in a representative environment".

Design The 25 [kN] LOx-LNG (liquid natural gas) engine uses the expander *bleed* cycle [42]. This means that, after having regeneratively cooled the engine, only a portion of the fuel is used to power the turbines and is bled off afterwards, making it an open cycle. This is different from a closed expander cycle, where all of the fuel powering the turbines is injected into the main combustion chamber, similar to a staged combustion engine.

LUMEN features a dual-shaft turbopump system, with single-stage pumps and turbines [42], [43]. This decision was made to increase the simplicity and modularity of the system, allowing components to be easily replaced. The turbopumps use COTS angular contact bearings, cooled by oil rather than the propellants, in order to enhance their lifespan.

A CAD cross-section of the oxidizer turbopump (OTP) can be seen in Figure 2.15. The TPAs feature 3D printed components, such as Inconel 718 housings/volutes and Titanium impellers [42]. The turbine blisks are machined out of Inconel 718. Both the OTP and fuel turbopump (FTP) use supersonic partial

admission axial impulse turbines with a total-to-static pressure ratio of 13 and 12.5, respectively [43], [44]. With an inlet pressure of 30 bar, this ensures choked flow at the turbine exhaust in order to decouple it from the downstream conditions. The OTP and FTP feature three and five circular nozzles, respectively, due to the different power requirements. The turbine drive gas temperature is kept below 500 K. This reduces the power density of the turbine but allows the Inconel to retain a high E-modulus and yield strength, significantly reducing the fatigue and increasing its lifespan [45].

Both the OTP and FTP use closed, full emission centrifugal impellers. No inducers are used, in order to limit the risk of contact with the wall. Instead, the inlet pressure is increased.

The specifications of the turbopumps are shown in Table 2.4. Unfortunately, no mass estimate is available for this system.

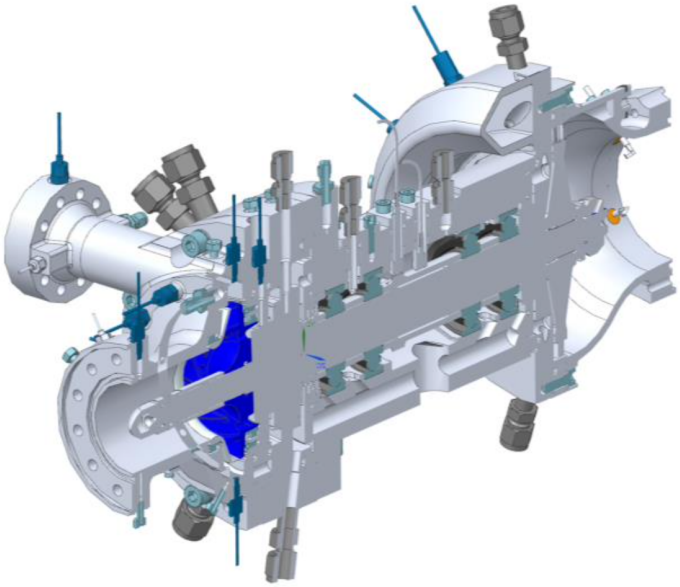

Figure 2.15: CAD cross-section of the LUMEN oxidizer turbopump (OTP). Source: [42].

Table 2.4: Specifications of the LUMEN OTP and FTP [42], [43], [45], [44].

Property	OTP	FTP	Unit
Shaft Speed	24	42	[krpm]
Shaft Power	85	100	[kW]
Pump Mass Glow	5.8	2.8	[kg/s]
Pump Outlet Pressure	77	83	[bar]
Turbine Mass Flow	1.046	1.046	[kg/s]
Turbine Pressure Ratio (t-s)	13	12.5	[bar]
Turbine Inlet Pressure	30	30	[bar]
Turbine Gas Temperature	488.36	487.4	[K]
Turbine Admission	0.229	0.356	[-]

According to Traudt et al. [46, p. 3], the first iteration of LUMEN will use floating ring seals; however, other sealing solutions such as stepped seals are being developed.

Takeaways The LUMEN turbopump is another R&D-oriented design. As such, a modular dual shaft system is used, with externally cooled bearings and low turbine temperatures, in order to increase its lifespan. These features are applicable to turbopump prototypes within DARE, but result in an inefficient design for flight.

It is advisable to keep the turbine exhaust pressure above $p_{out,min}$, as per Equation 2.3 (where γ is the heat capacity ratio of the turbine gas), to maintain choked flow at the outlet. This decouples the turbine from ambient conditions [44], [47], which is especially important for a flight version of the turbine, where the ambient pressure varies significantly throughout the flight trajectory.

$$p_{out,min} \geq p_{ambient} \left(\frac{\gamma + 1}{2} \right)^{\frac{\gamma}{\gamma - 1}} \tag{2.3}$$

Lastly, at Firebolt's scale, it is likely that a partial admission turbine is required if an axial turbine is used.

3

Research Framework

As established in Chapter 1, the transition to a pump-fed system is essential to overcome the limitations of the pressure-fed cycle and achieve higher-performing rocket architectures. While pump-fed systems are commonplace in large-scale launch vehicles, the use of a pressure-fed system for DARE's Stratos V rocket has highlighted the importance of advancing such technologies within DARE. While developing an electric fuel pump prototype for the bi-propellant Firebolt engine family, the limitations of the electric drive system were found to be too restrictive when scaling up to more powerful engines and the recommendation was made to develop turbine-powered pumps for future generations of the Firebolt engine and Stratos rockets.

To support this development, Chapter 2 reviewed the most important design elements and considerations of rocket engine turbopumps and presented several case studies. Additionally, a research gap was identified in the underexplored potential of radial turbines for rocket engine turbopumps, as presented in Section 3.1. This leads to the research questions and scope of the thesis, presented in Section 3.2. Finally, Section 3.3 outlines the structure of the thesis.

3.1. Research Gap

The vast majority of rocket engine turbopumps use axial turbines. Radial inflow turbines remain largely unused in rocket engines, despite their wide use in automotive applications, among others, and showing significant potential in waste heat recovery and energy production, such as Organic Rankine Cycle turbines. The motivation behind this prevalence of axial turbines in rocket engines is not well documented, but can likely be attributed to the lack of research and development into radial inflow rocket engine turbines, as well as the specific turbine requirements of large rocket engines. Nonetheless, radial inflow turbines may be a suitable solution for small rocket engines, where they may be able to provide equivalent or better performance compared to axial turbines while maintaining a small form factor and reduced complexity.

Therefore, the research objective of this thesis is:

> *To investigate whether a radial inflow turbine can be a suitable solution for a small-scale open-cycle rocket engine and whether it can provide a performance advantage compared to a typical axial turbine.*

In this thesis, small-scale engines are defined as 10-kilonewton-class engines. DARE's Firebolt DLX-150C

engine will be used as a design point for the turbine, in the context of a *hypothetical* successor to the Stratos V rocket, hereafter referred to as Stratos VI, for which the aim is to reach the highest altitude possible.

3.2. Research Questions and Scope

The following main research question and sub-questions are identified:

> ***Are radial inflow turbines a viable solution for powering the Firebolt engine in the DARE Stratos VI rocket?***

1. *What turbine performance is required to outperform electric pump-fed systems in terms of apogee for Stratos VI?*
2. *Can radial inflow turbines meet the performance requirements under the geometric and operational constraints of Stratos VI?*
3. *How do vaned and vaneless radial inflow turbines compare in terms of performance and aerodynamic flow behaviour?*
4. *How do radial inflow turbines compare to single-stage axial turbines in the context of small-scale open-cycle rocket engines?*
5. *How sensitive is the performance of radial inflow turbines to the changing atmospheric conditions during a rocket launch?*

Sub-question 5 pertains to the fact that, as the rocket ascends, the atmospheric pressure decreases. As this can influence the performance of the turbine, its effect needs to be taken into account and quantified. This is further explained in Section 4.2.

3.3. Approach and Thesis Outline

The thesis is structured as follows:

- Chapter 4 presents the methodology used to address the research questions. This includes the system-level trade study to determine the turbine design point and requirements, the design methodology of the turbines, and the CFD verification.
- In Chapter 5, the outcomes of the system-level trade study are presented, the final turbine designs are presented and the CFD results are discussed.
- Chapter 6 summarises the findings and answers the research questions.
- Chapter 7 provides suggestions for further optimisation of the turbine designs and the development of turbines within DARE.

4

Methodology

This chapter describes the full methodology adopted in this thesis. First, an overview of the general workflow is presented in Section 4.1, followed by the turbopump requirements in Section 4.2. Next, the system-level trade study methodology is explained in Section 4.3, after which the turbine design methodology is explained in Section 4.5. Finally, the CFD performance assessment methodology is described in Section 4.6.

4.1. Workflow

The methodology workflow used in this thesis is summarised graphically in Figure 4.1.

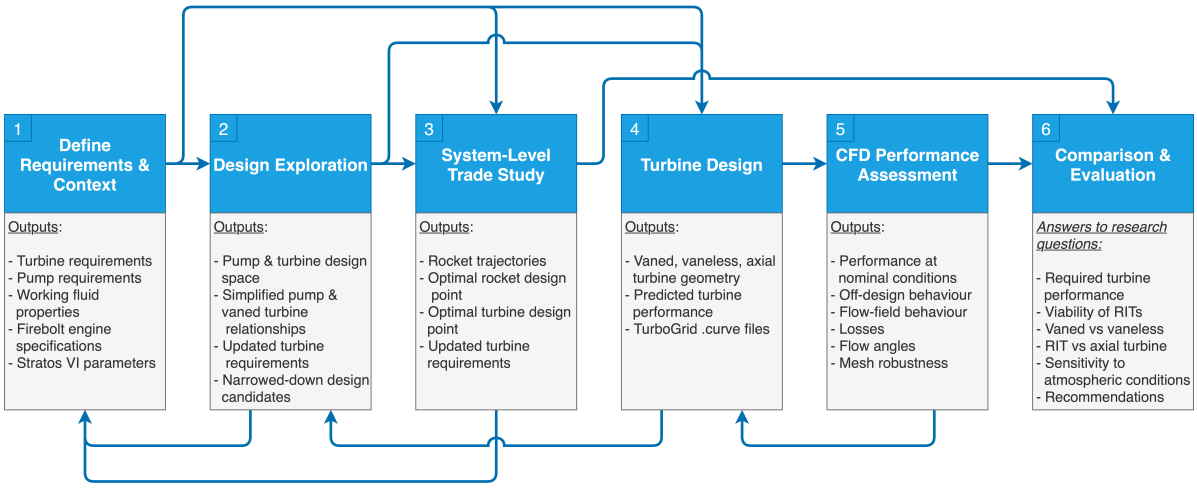

Figure 4.1: Flowchart of the methodological approach for the system-level trade study, turbine design and performance evaluation.

Before designing the turbines, the requirements and context of the system first need to be established (diagram block 1). This involves collecting the key parameters of the Firebolt engine, the propellant pumps and the Stratos VI rocket, which are later used in the system-level trade study and influence the design space of the turbines. Additionally, the turbine parameters are placed into context. Particularly, the influence of turbine performance on the overall rocket engine performance is explained, as well as the influence of the chosen inlet and outlet pressures on the turbine performance. Additionally, the properties of the working fluid are defined, based on the used propellant combination and maximum

turbine inlet temperature. This process is documented in Section 4.2.

Based on these requirements, initial design explorations are conducted in SoftInWay AxStream (diagram block 2), a commercial turbomachinery design and analysis software [48]. It features a Preliminary Design module, which generates thousands of turbomachinery geometries based on a set of requirements, after which an inverse solver calculates the performance based on reduced-order and semi-empirical loss models. Afterwards, the design space is explored using various filters, through which the design parameters are further refined. These initial design explorations serve as a way to establish the design space of the turbines and create simplified correlations between the rotor diameter of the turbines and their mass and mass flow. These are based on vaned radial inflow turbines (RITs), as this was initially assumed to be the most feasible configuration. The general design generation and exploration process is documented in Section 4.5.

A system-level trade study is then performed (diagram block 3), trading off several high-level rocket design decisions, such as burntime and rocket diameter, to achieve maximum altitude while maintaining sufficient stability during ascent. The rockets are sized using a combination of empirical methods and models developed within DARE, and are largely based on the design of the Stratos V rocket. Trajectory simulations are then carried out to compare the pressure-fed, electric pump-fed and turbopump-fed architectures and to determine the optimal mission profile and turbine design point. From these results, updated turbine requirements (diagram block 1) are obtained, including the maximum physical envelope and required mass flow. This process is explained in Section 4.3.

Due to the highly constrained design space and low efficiencies estimated by AxStream, an RPM selection procedure is carried out using design explorations (diagram block 2), in which the optimal rotational velocity of the turbine is selected, taking into account its influence on the propellant pumps. This process is explained in Section 4.4.

With these updated requirements, also presented in Section 4.2, the final turbine designs are then generated in AxStream (diagram block 4). While only vaned RKTs were considered before, the design explorations showed that vaneless RITs could be a feasible contender. Therefore, three turbine designs are made: a vaned RIT and a vaneless RIT, both studied in detail, as well as a preliminary axial turbine design. Since the axial turbine is not further optimised nor validated, no formal comparison can be made. However, it provides a preliminary indication of what may be achieved with an axial design, and whether or not the RITs are worth pursuing in future work. The turbine exploration and design process is explained in Section 4.5

The selected designs are subsequently evaluated using computational fluid dynamics simulations (CFD) in Ansys CFX (diagram block 5). Steady-state RANS simulations are performed to analyse the flow behaviour to greater detail than AxStream's preliminary performance estimates. Off-design analyses are carried out to assess the turbines' performance at other operating conditions, including sea-level and near-vacuum pressures, as well as at a higher shaft speed. A mesh refinement study is performed to ensure sufficient robustness of the CFD results. While a full sensitivity analysis of turbulence models and boundary conditions is not conducted in this thesis, the influence of operating conditions is assessed through the off-design cases. Due to the inherent limitations of CFD modelling, the results presented in this thesis can be regarded as verified within the CFD methodology, but not fully validated against experimental data, which is beyond the scope of this work. The CFD simulation methodology is

explained in Section 4.6.

Finally, the CFD and system-level trade study results are analysed (diagram block 6) to evaluate the turbine performance, compare the configurations, answer the research questions, and propose recommendations for further optimisation.

The turbines are evaluated at several locations, shown schematically in Figure 4.2a and Figure 4.2b for the vaned RIT and axial turbine, respectively. Subscripts *h* and *s* denote the hub and shroud, while the streamwise stations are denoted as below. The definitions for the vaneless RIT are equivalent to the vaned RIT, but exclude the stator. Unless specified otherwise, the calculated flow quantities at each station are mass-flow averaged along that station.

- *in*: Volute inlet
- *0*: Volute outlet, stator inlet
- *1*: Stator outlet
- *2*: Rotor inlet
- *3*: Rotor outlet, duct inlet
- *out*: Duct outlet

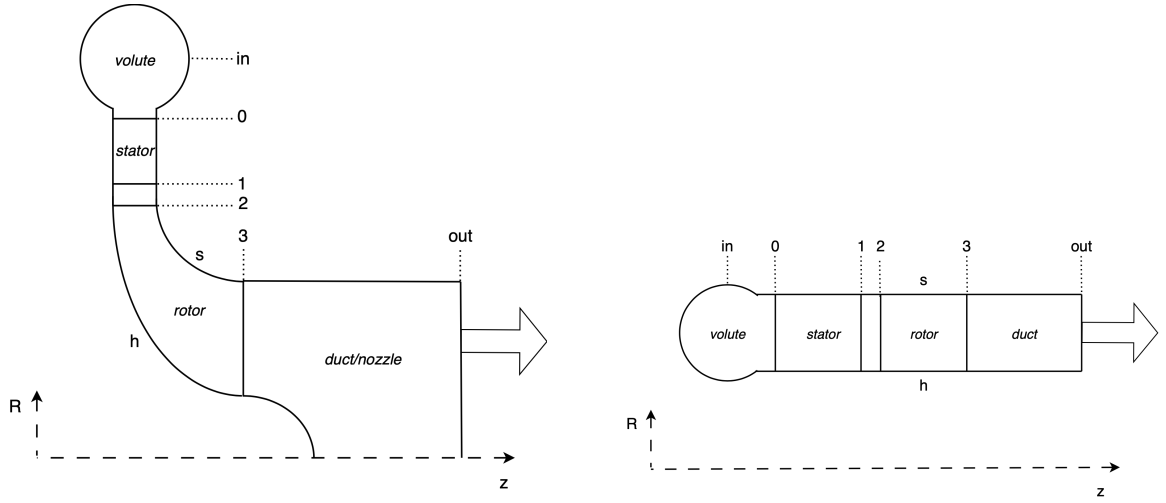

(a) Vaned radial inflow turbine.

(b) Axial turbine.

Figure 4.2: Meridional view of the vaned radial inflow turbine. *in* and *out* represent the volute inlet and duct/nozzle outlet. Numbers represent the different stream-wise stations. *h* and *s* indicate the hub and shroud. The arrow indicates the flow direction.

4.2. Turbopump Requirements

Before designing the turbines, a set of requirements and constraints must be established, which form the basis for the AxStream input parameters. First, Subsection 4.2.1 presents the pump requirements, based on which the preliminary pump design exploration is performed.

Then, several design parameters of the turbine are placed into context. Particularly, the influence of turbine performance on the overall rocket engine performance is explained in Subsection 4.2.2, as well as the influence of the chosen inlet and outlet pressures on the turbine performance in Subsection 4.2.3. Additionally, the properties of the working fluid are defined in Subsection 4.2.4, based on the used

propellant combination and maximum turbine inlet temperature. Finally, the turbine requirements themselves are presented in Subsection 4.2.5.

4.2.1. Pump Requirements

As explained in Section 4.1, the preliminary turbine design explorations used for the rocket model were performed based on a preliminary shaft power estimate of 21.4 kW, provided by DARE [49]. For the final turbine designs, a pump design exploration is performed to obtain a more optimal design point for the turbopump.

This design exploration is performed based on the pump requirements and fluid properties listed in Table 4.2 and Table 4.1. The shaft speed is limited to 80 krpm to avoid complications with friction, mechanical stresses and the availability of COTS bearings. Particularly, the seals are sensitive to friction and may wear down rapidly at high speeds. The rotor outlet diameter is constrained to 45 mm, so as not to exceed the size of the existing pump, and the pump inlet pressure is increased to 8 bar.

Table 4.1: Relevant fluid properties for the preliminary design exploration of the propellant pumps [49], [50].

Property	Fuel (80% ethanol, 20% water)	Liquid Oxygen
Density [kg/m^3]	819	1141
Temperature [K]	293.15	90.00
Specific Heat at Constant Pressure [J/(kg K)]	2855	1700
Kinematic Viscosity [m^2/s]	2.515e−6	2.0e−6
Vapour Pressure [Pa]	101325	7470

Table 4.2: Pump design requirements [49], [51].

Property	Fuel Pump	LOx Pump
Rotational velocity range [krpm]	40-80	40-80
Inlet total pressure [bar]	8	8
Outlet total pressure [bar]	45	45
Mass flow [kg/s]	1.696	2.509
Maximum NPSH$_r$ [m]	79.7	57.2
Minimum hub diameter [mm]	12	12
Maximum rotor diameter [mm]	45	45

4.2.2. Influence of Turbine Performance on Engine Performance

Before designing the turbines, it is essential to understand their influence on the efficiency of the rocket engine as a whole. As explained in Subsection 2.1.1, a common metric for rocket engine efficiency is the specific impulse, or I_{sp}, which represents the total propellant consumption (mass flow, $\dot{m}$) for a given thrust level (F_T), see Equation 2.1. In an open cycle rocket engine, a higher turbine mass flow results in a higher overall engine mass flow, and therefore a lower engine efficiency, as shown graphically in Figure 4.3 for DARE's Firebolt engine. The distinction between turbine efficiency (η) and engine efficiency is critical, as a more efficient turbine does not necessarily translate to a more efficient engine. In fact, as identified in the design explorations (see Section 5.2), turbines with higher turbine efficiency frequently feature higher mass flows, for this particular design point.

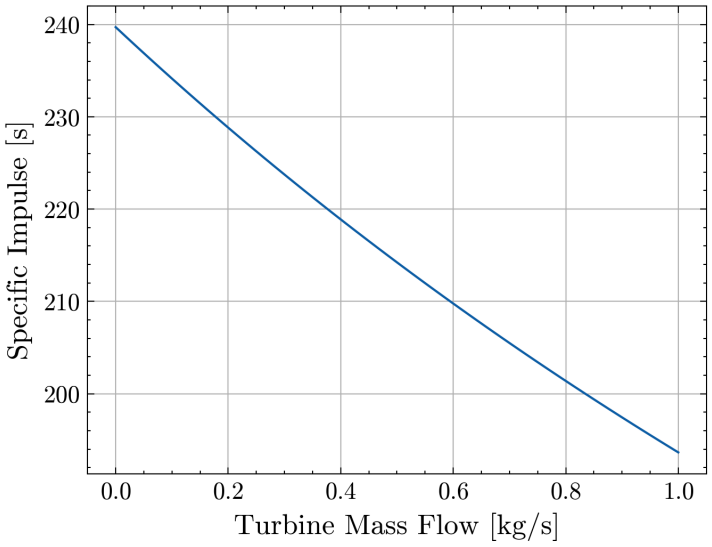

Figure 4.3: Specific Impulse I_{sp} of DARE's Firebolt engine as a function of gas generator mass flow.

Consider two geometrically identical turbines, operating at the same rotational velocity (ω) with the same working fluid. Turbine A operates at the ideal pressure ratio (PR), whereas turbine B operates at a higher pressure ratio than designed for. While turbine A will by definition achieve a higher efficiency at its ideal PR, turbine B will obtain a lower isentropic outlet temperature, as per Equation 4.1, allowing it to generate the same amount of work with a lower mass flow. Note that this is not universally true, as the actual outlet static temperature (T_{out}) and therefore the change in enthalpy still depends on the total-to-static efficiency η_{ts}, see Equation 4.2.

$$T_{out,is} = T_{t,in} \left(PR^{\frac{1-\gamma}{\gamma}} \right) \tag{4.1}$$

$$T_{out} = T_{t,in} - \eta_{ts} \left(T_{t,in} - T_{out,is} \right) \tag{4.2}$$

Nonetheless, the turbine η_{ts} still remains a good indicator of turbine performance. A low efficiency indicates significant losses within the stage, implying that either the turbine design can be improved, or the turbine is not operating at the ideal design point.

4.2.3. Influence of Pressures on Turbine Performance

As hinted at, the pressures at the inlet and outlet have a great influence on the overall design and performance of the turbine.

The total-to-static pressure ratio (PR_{ts}) of the turbine is one of the more important parameters in turbine design. As mentioned in Subsection 4.2.2, a higher pressure ratio results in a lower isentropic outlet temperature, which theoretically allows more work to be extracted from a fluid. In reality, this has its limits, as a high stage PR will typically result in a significant decrease in efficiency and may therefore require a higher mass flow.

The inlet total pressure $p_{t,in}$ is often dictated by the PR and outlet pressure. Here, the $p_{t,in}$ is generated by the gas generator, and is therefore limited by its capabilities. Its maximum combustion

chamber pressure $p_{c,GG} = p_{t,in}$ is subject to the same limitations as the engine's main chamber pressure $p_{c,engine} = 30$ bar, i.e. the outlet pressure of the pumps. To account for the pressure drop across the GG's throttle valves and provide a margin for increased turbine PR if performance is lower than expected, the maximum $p_{t,in}$ is reduced to 25 bar.

Also worth noting is the influence of the inlet pressure on the turbine geometry. As the inlet pressure increases, so does the density. As a result, for the same mass flow and rotor diameter, a smaller volute can be used, reducing the stage's overall size. This also results in lower blade heights at the stator and rotor, and therefore a higher clearance-to-blade-height ratio, which can lead to higher losses. Furthermore, the higher density requires smaller stator throats, posing manufacturing concerns in small, low mass flow turbines such as the ones considered here.

The outlet static pressure p_{out} may be kept the same as the ambient pressure, i.e. 1 atm, as the turbine simply exhausts to its environment. However, as the rocket ascends, the atmospheric pressure approaches near-vacuum conditions. In order to maintain constant and predictable performance, the turbine mass flow and pressure ratio are ideally kept constant.

One way to achieve this is to choke the flow in the turbine. As follows from Equation 4.3, valid for ideal gases, the mass flow through a choked nozzle is independent of the downstream pressure.

The minimum pressure ratio for which the flow is choked, also called the critical pressure ratio PR_{crit}, is given by Equation 4.4. For this turbine's driving gas (see Subsection 4.2.4), $PR_{crit} = 1.809$.

$$\dot{m} = C_d A \sqrt{\gamma \rho_0 p_0 \left(\frac{2}{\gamma+1}\right)^{\frac{\gamma+1}{\gamma-1}}} \tag{4.3}$$

$$PR_{crit} = \left(\frac{2}{\gamma+1}\right)^{\frac{\gamma}{\gamma-1}} \tag{4.4}$$

where C_d is the discharge coefficient of the nozzle, A is the throat area of the nozzle, and ρ_0 and p_0 are the gas density and total inlet pressure.

In vaned turbines, the stator row is often used as the choking point, particularly in rocket engine turbines. This results in supersonic flow in the rotor and is therefore more applicable to impulse turbines. In vaneless turbines, the flow can be choked in or before the volute, or a choked nozzle can be installed downstream of the rotor. The latter is common in rocket engines, even in those that use choked stators. Examples include SpaceX's Merlin engine and Ariane 5's Vulcain 2 engine, see Figure 4.4-4.5 [52]. These have the added benefit of recovering some potential and kinetic energy in the form of additional thrust [53].

In this thesis, both a vaned (supersonic) turbine and a vaneless turbine are designed. For the vaneless turbine, a converging choked nozzle is used downstream of the rotor.

4.2.4. Turbine Driving Gas

The driving gas for the turbine is provided by the gas generator (see Section 2.5), which combusts the same propellants as the engine, i.e. Liquid Oxygen (LOx) and 80% ethanol. To maximise power density, the turbine inlet total temperature should be as high as the material allows. Following the

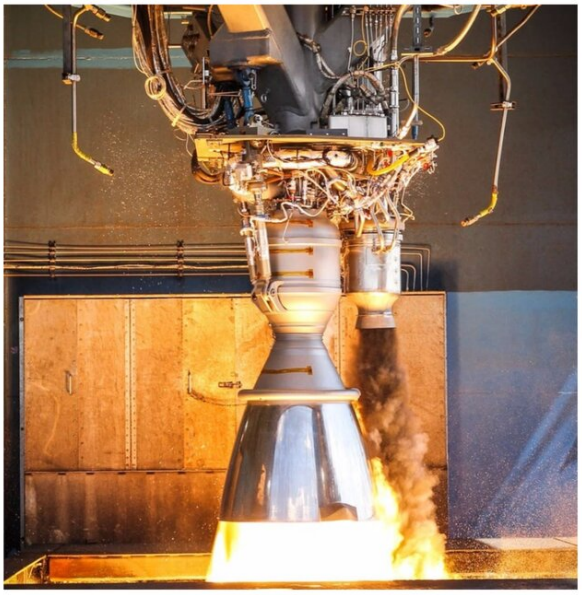

Figure 4.4: SpaceX's Merlin 1D engine with visible turbine outlet nozzle and sooty exhaust. Image courtesy of SpaceX [54].

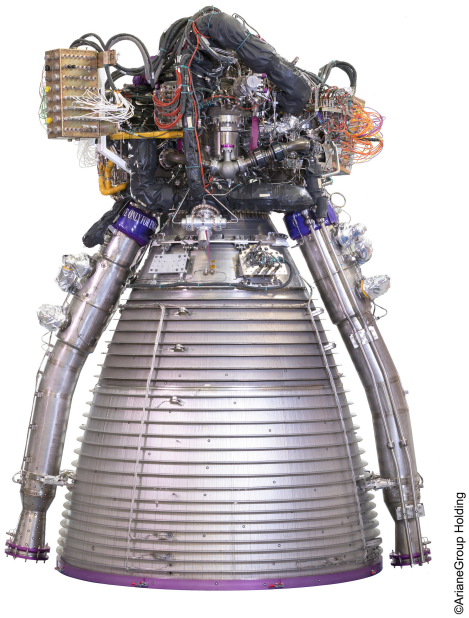

Figure 4.5: Ariane 5's Vulcain 2 engine with visible oxidizer and fuel turbine outlet nozzles. Image courtesy of ESA [55].

recommendation of *Van Der Lee Turbo Systems* [56], the selected turbine material is Inconel 713C, with a maximum operating temperature of 980 °C (1253.15 K).

The required mass fraction between the oxidizer and fuel, also called the OF ratio, and the resulting properties of the driving gas are determined using the RocketCEA Python library. This is a wrapper for NASA's CEA software, which calculates chemical equilibrium and gas properties of chemical mixtures, such as those found in rocket engine thrust chambers or gas generators [57], [58]. The frozen flow assumption is used, where the reaction products are considered to remain chemically frozen as opposed to continuously reacting. While the real flow behaviour lies somewhere between the frozen and equilibrium conditions, the frozen flow assumption yields a significantly lower heat capacity compared to the equilibrium flow assumption (2316.23 J/(kg K) vs. 3684.76 J/(kg K)) and thus less available total enthalpy at the inlet of the turbine. This results in a conservative lower bound on the estimated turbine performance to avoid overpredicting its power density.

The relationship between OF ratio and adiabatic flame temperature in the gas generator for low OF ratios is shown in Figure 4.6. The required ratio for the desired temperature is 0.57. The gas properties calculated by RocketCEA are summarised in Table 4.3. The species of the turbine driving gas and their respective mass fractions are given in Table 4.4.

4.2.5. Turbine Requirements

The final requirements for the RITs, which are used as inputs for the design explorations in AxStream, are summarised in Table 4.5. The maximum turbine and volute diameter are chosen based on the maximum available space in the rocket, see Subsection 4.3.2. The shaft speed of 70 krpm and shaft power of 24.4 kW follow directly from the RPM selection process, see Section 4.4.

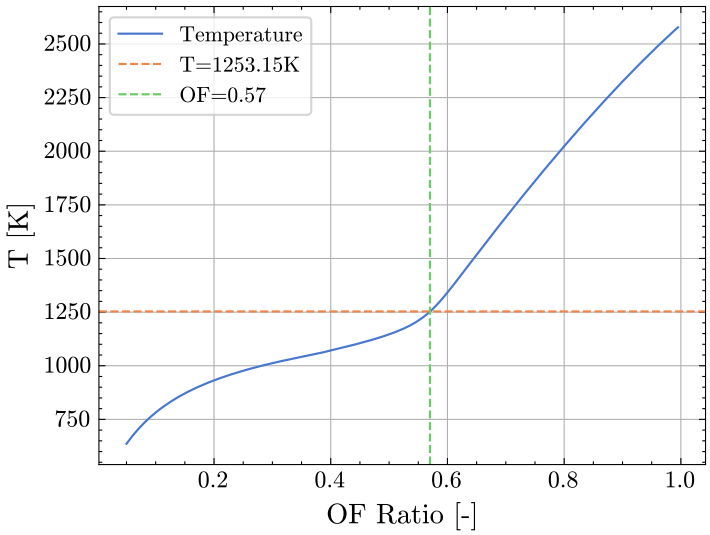

Figure 4.6: Gas generator adiabetic flame temperature as a function of the oxidizer-fuel (OF) ratio.

Table 4.3: Thermophysical properties of the gas mixture

Property	Symbol	Value
Ratio of specific heats [-]	γ	1.227
Molar weight [g/mol]	M	16.1839
Specific gas constant [J/(kg K)]	R	513.748
Viscosity [cP]	μ	4.86e2
Thermal conductivity [W/(cm K)]	k	0.00207
Specific heat at constant pressure [J/(kg K)]	C_p	2316.226

Table 4.4: Composition of the gas mixture

Species	Mass Fraction [-]	Molar Weight [g/mol]
CH_4	0.0047	16.042
CO	0.4596	28.010
CO_2	0.2386	44.010
q H_2	0.0526	2.016
H_2O	0.2446	18.015

For the vaneless turbine, a minimum outlet pressure of 2 bar was assumed to accommodate a choked outlet nozzle. For the vaned turbine, a minimum outlet pressure of 1 bar is used instead, as the flow is already choked by the stator nozzles. Several additional requirements are made, pertaining to the manufacturability of the turbine, in accordance with *Van Der Lee Turbo Systems*' recommendations. Particularly, the minimum stator throat size and stator leading edge radius are limited, since Inconel is a notoriously difficult material to machine, and a 0.3 mm rotor tip clearance is assumed. Additionally, the rotor blade inlet metal angle is constrained to 0°(defined wrt. the normal direction) to limit the bending deformation caused by the centrifugal loads. The maximum turbine and volute diameter are chosen based on the maximum available space in the rocket, see Subsection 4.3.2.

The preliminary turbine design explorations, used for the system-level trade study (Subsection 4.3.2),

were performed using an initial rotational speed assumption of 40 krpm, based on DARE's initial sizing estimates of the next-generation propellant pumps. Similarly, a maximum inlet temperature of only 950 °C was used.

The requirements for the axial turbine are also listed in Table 4.5. The turbine turbine is chosen to be a High Pressure (HP) stage, as it can efficiently extract energy from high pressure fluids using supersonic stators, and is therefore well-suited for single-stage turbines with high pressure ratios. The stator nozzles are of the Convergent-Divergent Vaned (CDV) type. While more difficult to manufacture than drilled nozzles, they result in a more compact design, as the drilled nozzles protrude outside the rotor tip diameter, requiring a larger volute. A partial admission turbine is chosen, for which the admission ratio is determined by AxStream.

Due to the axial placement of the volute, a larger rotor diameter of 82 mm can be used. Similarly to the vaned RIT, the minimum outlet static pressure is reduced to 1 bar. The leading and trailing edge radii are fixed at 0.25 mm, slightly more lenient than the radial inflow turbine[1].

Table 4.5: Turbine design requirements.

Property	Vaned RIT	Vaneless RIT	Axial
Material	Inconel 713C	Inconel 713C	Inconel 713C
Turbine inlet total temperature [°C]	980	980	980
Rotational velocity [krpm]	70	70	70
Minimum shaft power [kW]	24.37	24.37	24.37
Minimum hub diameter [mm]	10	10	10
Maximum rotor diameter [mm]	50	68	82
Inlet total pressure range [bar]	8 - 25	8 - 25	8-25
Outlet static pressure range [bar]	1 - 12	2 - 12	1 - 12
Minimum throat width [mm]	0.75 (stator)	None	0.75
Minimum edge radius [mm]	0.3 (stator TE)	None	0.25 (TE, LE)
Rotor tip clearance [mm]	0.3	0.3	0.3
Inlet metal angle [deg]	0	0	None

4.3. System-Level Trade Study

As explained in Subsection 4.2.2, a lower turbine mass flow maximises rocket engine efficiency in open-cycle systems, improving overall rocket performance. Initial design explorations showed that the optimal turbine designs (i.e., those requiring low mass flows) featured large rotor diameters, which were incompatible with the current rocket design. Increasing the rocket diameter would allow for a larger, more efficient turbine, but comes at the cost of increased drag, due to the larger frontal area. As such, the turbine efficiency needs to be balanced against the aerodynamic performance of the rocket.

To address this trade-off and find the optimal design point of the rocket and, correspondingly, the turbine, a system optimisation is performed. The process is as follows. First, simplified numerical fits are established in Subsection 4.3.1, which yield preliminary estimates of the turbine envelope, mass and

[1]This is because the axial turbine design was created at a later point in time, and this requirement was relaxed as per *Van Der Lee Turbo Systems*' recommendation.

mass flow as a function of the rocket diameter. Then, a rocket model is developed in Subsection 4.3.2, estimating the geometry (mass, length, center of gravity (CG), etc.) and performance (drag, mass flow, etc.) for every specified design point, using the original Stratos V design as baseline. Different rocket models are created for each engine cycle, i.e. pressure-fed, electric pump-fed and turbopump-fed. Finally, a trajectory simulation tool is used in Subsection 4.3.3 to compare the rocket architectures and trade off different design points, such as burntime and rocket diameter.

4.3.1. Turbine Diameter Correlation

Two methods are employed to obtain a simplified relationship, correlating the turbine diameter and the required mass flow.

For the first method, a design exploration is performed in AxStream for a range of turbine diameters, following the method explained in Subsection 4.5.1. This design exploration was performed for supersonic vaned turbines only, with the requirements presented earlier in Subsection 4.2.5. The results, shown in Figure 4.7, are filtered to include only designs that meet the minimum required power, with an upper limit of 5% above that, to avoid oversized designs requiring excessive mass flow.

A general trend can be observed, where larger rotor diameters require lower mass flows to generate the same power. A second-order polynomial is fitted to the datapoints, which is later used to size the rockets in Subsection 4.3.2.

Following this polynomial, the highest efficiencies are achieved with larger diameters and higher mass flows, until a minimum mass flow of 155 g/s is reached with a rotor diameter of 105 mm.

Several of the turbine designs generated in AxStream have been selected and transferred to CAD to obtain an empirical relationship between their rotor diameter and mass. Once again, Inconel 713C is assumed as the material, with a density of 7913 kg/m^3. As per *Van Der Lee Turbo Systems*' [56] recommendation, a wall thickness of 3 mm is assumed for the volute, hub and shroud.

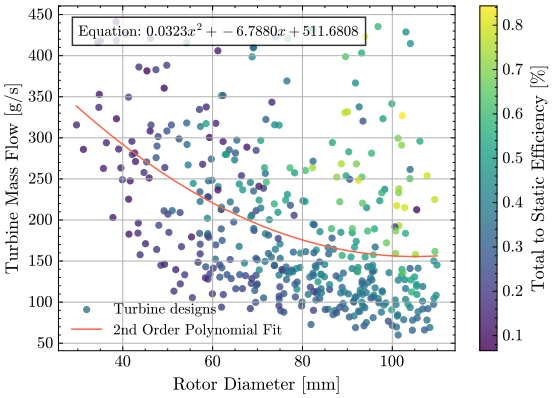

Figure 4.7: Preliminary design exploration of the vaned RIT in AxStream, showing the turbine mass flow as a function of the rotor diameter.

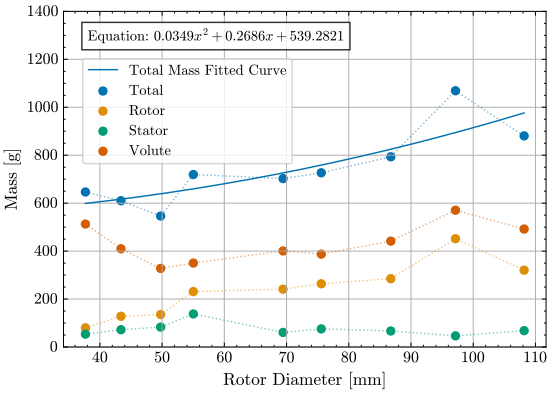

Figure 4.8: Estimated RIT masses as a function of rotor diameter, based on generated turbine designs.

The second method is based on the work by Mounier et al. [59], which introduces an updated version of the current non-dimensional Ns-Ds maps (such as Baljé's chart in Figure 2.5) for small-scale (supersonic) vaned RITs. This 0D map was generated using a 1D mean-line analysis model, validated against

CFD simulations and experimental data. While specifically developed for ORC applications, this non-dimensional map can still serve as a good initial estimate of turbine performance.

Equation 4.5-4.6 estimate the maximum attainable isentropic total-static efficiency η_{is} and optimal specific diameter D_S as a function of pressure ratio PR and specific speed N_S [59].

$$\begin{aligned}\eta_{\text{is}} &= 0.45 + 1.64NS - 0.05PR - 2NS^2 + 0.15NS\,PR + 0.63NS^3 \\ &\quad - 0.07NS^2PR - 0.003NS\,PR^2 \end{aligned} \tag{4.5}$$

$$\begin{aligned}DS &= 9.42 - 18.3NS - 0.16PR + 17.8NS^2 + 0.24NS\,PR \\ &\quad + 0.001PR^2 - 6.37NS^3 - 0.13NS^2PR + 0.001NS\,PR^2 \end{aligned} \tag{4.6}$$

For a given pressure ratio and outlet pressure, the relevant properties of the turbine are calculated as follows. The isentropic temperature at the outlet is calculated using Equation 4.1, resulting in the isentropic enthalpy change across the turbine Δh_{is} using Equation 4.7. The isentropic mass flow $\dot{m}_{is}$ and resulting isentropic volumetric flow rate Q_{is} are then found using Equation 4.8 and Equation 4.9, respectively, followed by the specific speed N_S using Equation 4.10, where ω is the rotational speed in rad/s. Consequently, the isentropic total-static efficiency η_{is} and specific diameter D_S are computed using Equation 4.5 and Equation 4.6. The turbine diameter is then found using Equation 4.12. Lastly, the actual outlet temperature T_{out}, enthalpy change Δh and mass flow $\dot{m}$ are calculated using Equation 4.2, Equation 4.13 and Equation 4.14, respectively.

$$\Delta h_{is} = C_p\,(T_{t,in} - T_{out,is}) \tag{4.7}$$

$$\dot{m}_{is} = \frac{P_{shaft}}{\Delta h_{is}} \tag{4.8}$$

$$Q_{is} = \frac{\dot{m}_{is}\,T_{out,is}\,R}{p_{out}} \tag{4.9}$$

$$N_S = \frac{\omega\,Q_{is}^{0.5}}{|\Delta h_{is}|^{0.75}} \tag{4.10}$$

$$D_S = \frac{D|\Delta h_{is}|^{0.25}}{Q_{is}^{0.5}} \tag{4.11}$$

$$D = \frac{D_S Q_{is}^{0.5}}{|\Delta h_{is}|^{0.25}} \tag{4.12}$$

$$\Delta h = C_p\,(T_{t,in} - T_{out}) \tag{4.13}$$

$$\dot{m} = \frac{P_{shaft}}{\Delta h} \tag{4.14}$$

The results of this design exploration are shown in Figure 4.9, along with a minimum-mass flow boundary. Iso-lines for constant outlet pressures and pressure ratios are shown in Figure 4.10. Once again, a similar general trend can be observed, where lower mass flows are achieved with larger rotor diameters. These results are more optimistic compared to those generated using AxStream, with the lowest mass flows of around 100 g/s being achieved with rotor diameters of around 90 mm, compared to 155 g/s and 105 mm. Additionally, the minimum mass flows occur at pressure ratios of around 4 and, for a given pressure ratio, lower outlet pressures result in lower mass flows, albeit with a larger rotor diameter.

The available size for the turbine is limited by the diameter of the rocket. As the turbopump needs to fit inside the fincan, next to the engine's throat, not much space is available. This is visualised using simple mock-ups, shown in Figure 4.11. While the turbopump can be mounted above the engine, this would extend the length of the engine bay, which can significantly affect the design of the rocket due to an increased length-diameter ratio, as explained in Subsection 4.3.3.

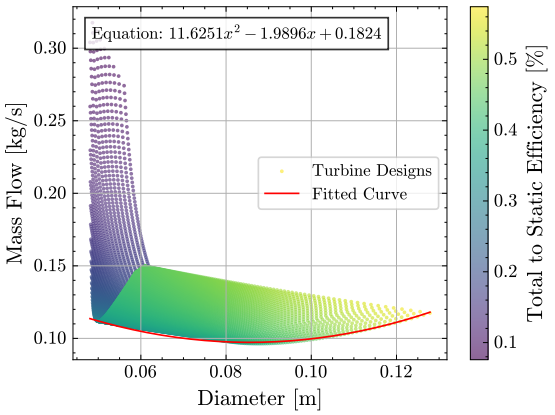

Figure 4.9: RIT design exploration based on Mounier et al.'s Ns-Ds map.

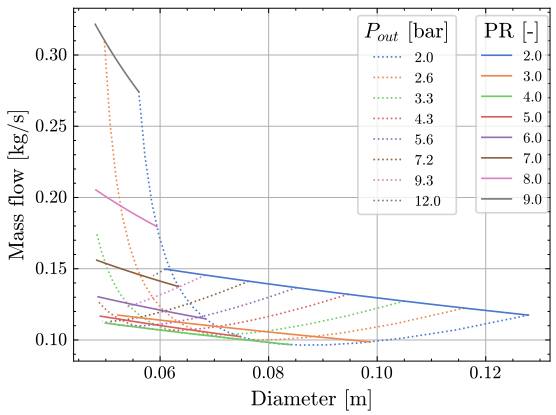

Figure 4.10: Iso-lines for constant outlet pressures and constant pressure ratios based on Mounier et al.'s Ns-Ds map.

In line with Stratos V's design, a 5 mm fincan thickness is assumed. The thickness of the volute casing is assumed to be 3 mm and, based on the geometries generated during the initial design exploration in AxStream, the radial span of the volute and stator are assumed to be 10 mm and 5 mm, respectively. Additionally, a clearance of 3 mm is maintained around the turbopump, as the turbine volute reaches high temperatures and should not make contact with the engine or fincan.

As the current fuel pump has a maximum span of around[2] 71 mm and the combustion chamber's outer diameter is 138 mm, a minimum outer diameter of 30 cm is required for pump-fed rockets (Figure 4.11a). As the rocket diameter increases, the volute can expand outwards until it approaches the throat of the engine, which happens at a rocket diameter of 35.5 cm (Figure 4.11b). After this, the turbopump assembly needs to be shifted outwards in order to maintain clearance with respect to the engine. The maximum allowable volute diameter and corresponding rotor diameter for every rocket diameter considered, i.e. up to 40 cm (Figure 4.11c), are shown graphically in Figure 4.12. In the rocket sizing tool, the largest possible turbine diameter is always selected, unless it results in a higher mass flow.

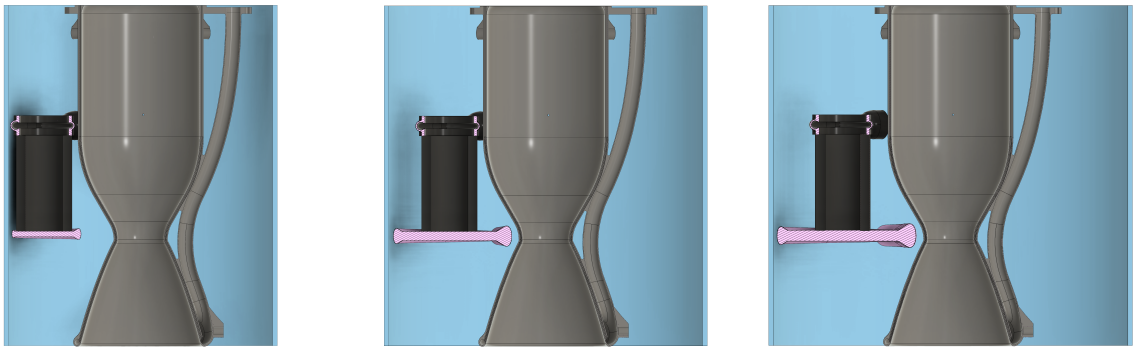

(a) 30 cm diameter. **(b)** 35.5 cm diameter. **(c)** 40 cm diameter.

Figure 4.11: Mock-ups of the engine bay's lower section for varying rocket diameters, showing the maximum available space for the turbine. Blue: fincan, grey: Firebolt engine, black: DTP-E74 fuel pump volute, purple: turbine volute.

An overview of the estimated turbine mass and mass flow as a function of the rocket diameter is shown

[2] As the volute channel has a spiral shape, the measured maximum width of the volute is dependent on the orientation of the pump. In this case, the pump is oriented in such a way to provide ample space to connect an L-shaped pipe and valve to the pump outlet.

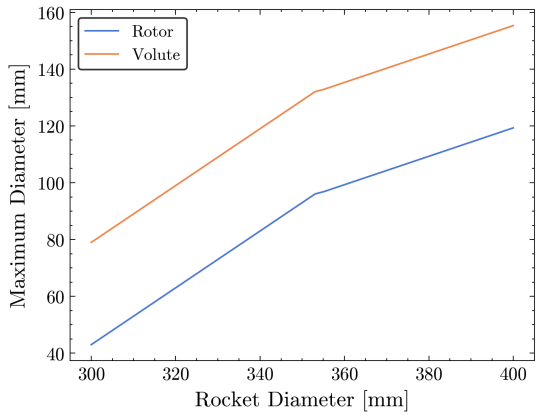

Figure 4.12: Maximum possible volute and rotor diameter as a function of the rocket's outer diameter.

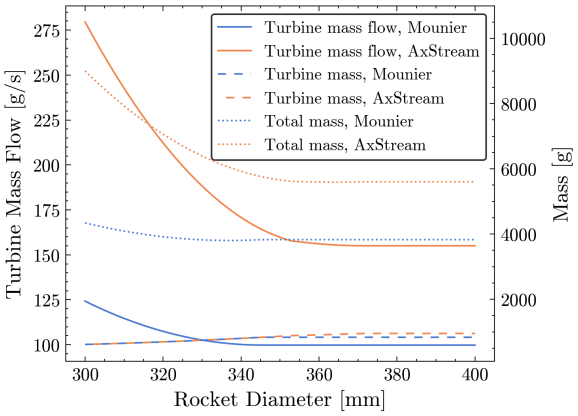

Figure 4.13: Estimated turbine mass, mass flow and total mass as a function of the rocket diameter, for a burntime of 30 s.

in Figure 4.13, for both the AxStream and Mounier et al. method. Additionally, the sum of the turbine mass and the propellant mass consumed by the turbine is shown for an assumed burntime of 30 s.

4.3.2. Rocket Design Parameters

Three different rocket architectures are considered: pressure-fed (like the original design), electric pump-fed and turbopump-fed. The former two are merely used as reference and do not influence the design of the turbines. All rockets are based on the original design of the Stratos V rocket, designed in 2022-2023, with the necessary adjustments specific to each architecture. The rocket is split up into several sections, housing different parts of the rocket, such as the avionics, payload and propulsion. A graphical overview of the rocket architecture is given in Figure 4.14.

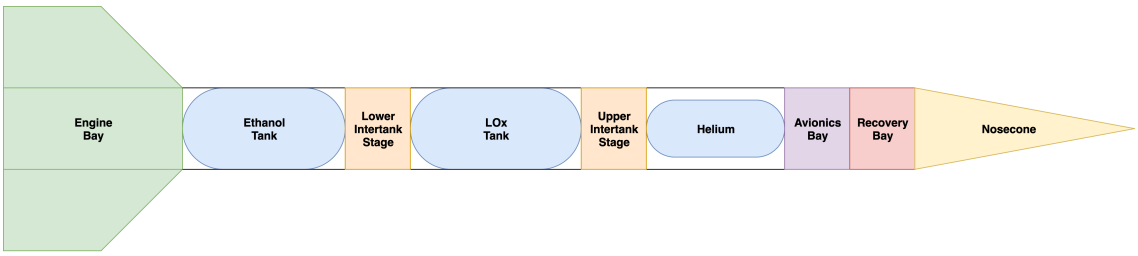

Figure 4.14: Graphical overview of the rocket's architecture.

Most internal masses, such as the feed system and avionics, are assumed to be constant, aside from minor changes inherent to the rocket architecture. The mass of the aerostructure (e.g. the cylindrical shells) is assumed to scale linearly with respect to the diameter and length of the section. In reality, the required thickness depends on the overall rocket mass and geometry, but the high safety factors on the rocket structure justify this assumption for this preliminary rocket sizing. The lengths of all sections are kept constant, irrespective of the diameter, except for the propellant tanks and pressurant tank.

The **nosecone and recovery bay**, which house the parachutes and deployment mechanisms, are considered to maintain a fixed length and internal mass. The mass of the aerostructure is scaled linearly with the diameter.

The **avionics bay**, which contains the flight computer, batteries and other electronics, follows a similar

logic. In the case of the electric pump-fed rocket, however, additional mass due to the batteries is added. The process of calculating these masses follows the same approach as [5] and [35], which is as follows.

Each pump is powered by a separate motor, due to the low availability of COTS high-power motors, which are each configured with a motor velocity constant K_V of 809.2 rpm/V. Dividing the desired rotational velocity by this value results in the required motor voltage V_{motor}. The operating current I is found using Equation 4.15, where P_{shaft} is the shaft power of the pump and η_{drive} is the drive efficiency, here assumed to be 90%. The voltage sag due to resistance losses V_{sag} is calculated with Equation 4.16, where $N_{parallel}$ is the number of parallel batteries (assumed 1), S is the number of cells in series per battery (assumed value between 6 and 8), n_2 is the phase current to battery current ratio (1.5) and R_{cell}, $R_{wires\,battery}$ and $R_{wires\,phase}$ are the internal resistance in the cells (3 $m\Omega$) and the wires (10 $m\Omega$). Based on the resulting total voltage requirement and the assumed amount of cells per battery, the amount of batteries in series N_{series} is found, assuming a voltage of 3.7 V per cell. The total battery power required $P_{battery}$, including the losses, is then found using Equation 4.17. The required total capacity Q_{total} (in mAh) and C-rating of the battery pack are calculated using Equation 4.18 and Equation 4.19, where t_{burn} is the burntime of the rocket (when the motors are powered on), SF is a safety factor (1.2) and D is the depth of discharge of the batteries (80%). The required capacity $Q_{battery}$ for each battery is then calculated by dividing Q_{total} by the amount of parallel strings[3]. In case the required C-rating is higher than 80, the capacity is increased such that the C-rating remains below the limit.

$$I = \frac{P_{shaft}}{\eta_{drive}\, V_{motor}} \tag{4.15}$$

$$V_{sag} = \frac{I}{N_{parallel}} \left(S\, R_{cell} + R_{wires\,battery}\right) + n_2\, I\, R_{wires\,phase} \tag{4.16}$$

$$P_{battery} = \frac{P_{shaft}}{\eta_{drive}} + I^2\, R_{cell}\, S + I^2 R_{wires\,battery} + (n_2\, I)^2\, R_{wires\,phase} \tag{4.17}$$

$$Q_{total} = P_{battery}\, t_{burn}\, SF \frac{1}{3.6\, D\, \left(V_{motor} + V_{sag}\right)} \tag{4.18}$$

$$C = 1000 \frac{I}{Q_{total}} \tag{4.19}$$

$$\tag{4.20}$$

The battery mass is estimated using an empirical relation based on a range of COTS batteries, as shown in Figure 4.15. Commercial batteries from [36] are selected, as they are DARE's preferred supplier for the electric pumps.

The **Upper Intertank Structure (U-ITS)** and the **Lower Intertank Structure (L-ITS)** contain the pressurisation system of the rocket and part of the feed system. Since the pressurisation system hardware requirements are less stringent for the pump-fed rockets due to the lower tank pressures, this system is also simplified[4], resulting in a very conservative estimated U-ITS mass and length decrease of 2 kg and 10 cm, respectively.

[3] A string is several batteries connected in series.

[4] In particular, active control can be omitted and only one spring-loaded regulator is required, as opposed to two dome-loaded regulators, one spring-loaded pilot regulator and two solenoid valves.

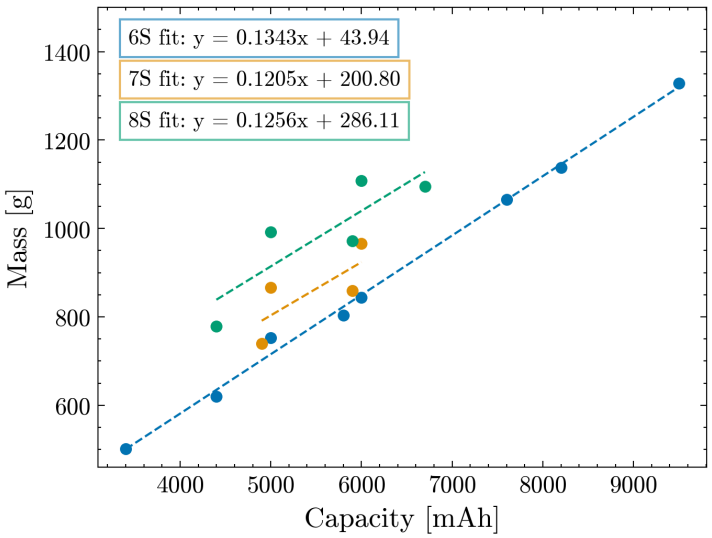

Figure 4.15: Battery mass as a function of capacity, for different cell counts. All batteries considered are from [36].

The **engine bay** houses the engine and part of the feed system, as well as the fincan which stabilises the rocket. The properties of the engine, excluding the turbine mass flow, are summarised in Table 4.6. While the thrust increases with the altitude due to the lower ambient pressure, the simulations assume a constant thrust level equal to 9888 N due to limitations of the trajectory simulator.

The mass of the cylindrical part of the fincan is scaled linearly with respect to the diameter, whereas the fins are assumed to remain the same for all rockets. The internal masses are also kept constant, aside from the addition of the pumps (1.35 kg each), as well as the motors and ESCs (1.77 kg per pump), or the turbine. The turbine diameter and resulting mass and mass flow are estimated using the methods presented in Subsection 4.3.1.

Table 4.6: Firebolt performance parameters at optimal thrust condition.

Property	Symbol	Value
Optimal Thrust [N]	$F_{T,\text{opt}}$	9888
Liquid Oxygen Mass Flow [kg/s]	$\dot{m}_{\text{LOx}}$	2.509
Ethanol Mass Flow [kg/s]	$\dot{m}_{\text{Eth}}$	1.696
Optimal Specific Impulse [s]	$I_{sp,\text{opt}}$	239.7

The **propellant tanks** are fully dependent on the burntime and total mass flow of the rocket. Ullage volumes of 5% and 10% of the required propellant volume are added to the fuel tank and LOx tank, respectively. The tanks are cylindrical with spherical domes, for which the thicknesses and corresponding masses are calculated using a tool developed within DARE [2], which assumes a yield design safety factor (FOSY) of 1.87 and an ultimate design safety factor (FOSU) of 2. The tanks are made of Aluminium alloy EN AW-6082-T6 (AlSi1MgMn) due to its combination of high strength and good weldability. The maximum expected operating pressures (MEOP) for the pressure-fed and pump-fed cycles are listed in Table 4.7, and are based on the original rocket design and the preliminary design of the new pumps. An additional fixed mass of 2.046 kg and 2.570 kg is added to the fuel tank and oxidizer tank, respectively, to account for internal feed lines, flanges and the capacitive LOx fill-level

sensor, based on the original Stratos V design. If the required propellant volume is too low to fill at least a spherical tank, resulting in either a negative cylinder length or a partially filled tank, the burntime is constrained to ensure a feasible tank geometry.

Table 4.7: Propellant tank maximum expected operating pressures.

Tank	**Pressure** [bar]
Pressure-fed LOx tank	45
Pressure-fed fuel tank	42
Pump-fed LOx tank	7.5
Pump-fed fuel tank	7.5

Similarly, the **pressurant tank** section is largely dependent on the total mass flows and tank pressures. The composite overwrapped pressure vessel (COPV) is sized as follows. For the pressure-fed rocket, the same Safer Cylinders COPV as Stratos V is assumed, which is the largest COTS COPV considered. This COPV has a volume of 40 l, with a length of 1.4 m and a maximum (initial) pressure of 400 bar, assuming a booster pump is used[5]. The maximum burntime is this limited by this volume.

The pump-fed rockets require a smaller COPV due to the lower propellant tank pressures. To avoid the need for a booster pump, the initial pressure is limited to 250 bar. To size the COPV volume, the method by Hermsen [60, p. 155] is used. The total required pressurant mass $m_{press,prop}$ for each propellant tank can be calculated using Equation 4.21, which assumes adiabatic heat transfer between the Helium pressurant and the propellant and where p_{prop} is the propellant tank pressure, V_{tank} is the volume of the propellant tank, R and γ are the specific gas constant and the ratio of specific heats of the pressurant gas, and $p_{COPV,final}$ and $p_{COPV,init}$ are the final and initial pressure of the COPV. T_{ullage} is the final temperature of the pressurant/ullage gas in the propellant tank, and has a significant influence on the required size of the COPV. If the pressurant mixes well with the cold ullage gas in the LOx tank, it results in a lower pressurant temperature and higher density, therefore requiring more pressurant mass. The heat transfer between these fluids is difficult to estimate and should ideally be tested. As a conservative estimate, the pressurant is assumed to cool down to the same temperature as the propellant as soon as it enters the tank. For the pressure-fed system, a higher, more realistic ullage temperature of 150 K is also considered. The residual pressurant mass remaining in the COPV $m_{press,COPV,resid}$ and propellants tanks $m_{press,prop,resid}$ after burn-out are found using Equation 4.22 and Equation 4.23. In the simulation, a constant mass flow is assumed from the COPV to the propellant tanks. This has no influence on the mass progression of the rocket, but only shifts the CG aftward.

[5]Booster pumps, or gas boosters, take a low pressure supply gas and compress it to obtain a high outlet pressure, allowing the COPV to be filled to much higher pressures than what is normally achievable with Helium supply bottles, which are limited to 300 bar. Booster pumps are ideally avoided due to the high cost and long filling time.

$$m_{press,prop} = \frac{p_{prop}\, V_{prop}}{R\, T_{ullage}} \frac{1}{1 - \left(p_{COPV,final}/p_{COPV,init}\right)^{1/\gamma}} \tag{4.21}$$

$$m_{press,COPV,resid} = \left(m_{press,LOx} + m_{press,fuel}\right) \left(\frac{p_{COPV,final}}{p_{COPV,init}}\right)^{1/\gamma} \tag{4.22}$$

$$m_{press,prop,resid} = \frac{p_{prop}\, V_{prop}}{R\, T_{ullage}} \tag{4.23}$$

The length and mass of the COPV are estimated empirically, based on a selection of 26 COTS COPVs. The relationship of the mass and length as a function of the volume are shown in Figure 4.16a and Figure 4.16b, respectively.

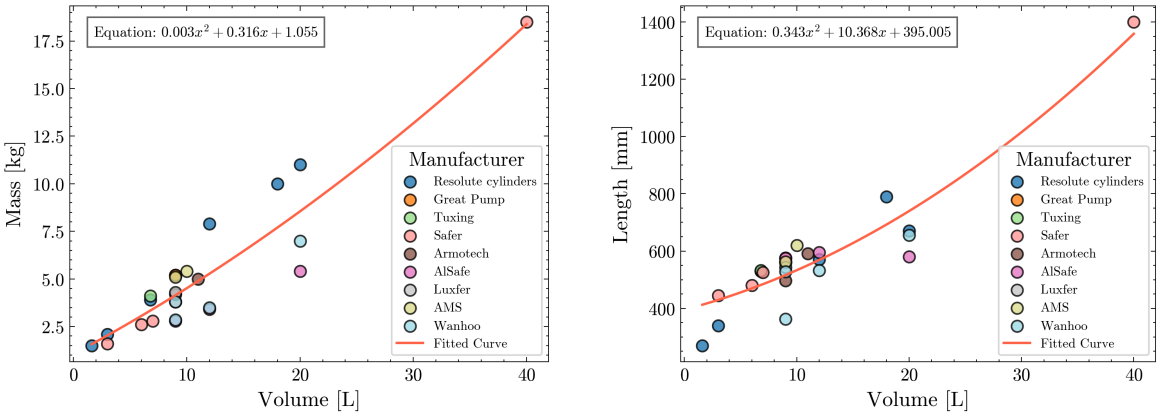

(a) COPV dry masses.

(b) COPV lengths.

Figure 4.16: Scatter plots of the length and dry mass as a function of the volume for the considered COPVs, with second order polynomial fits [61], [62], [63], [3], [64], [65], [66], [67], [68].

Unlike the propellant tanks, which double as structural airframe components, the COPV is housed within a composite cylinder similar to the ITSs, of which the mass is scaled linearly with respect to the length and diameter.

4.3.3. Rocket Trajectory Simulations

For each rocket engine cycle, i.e. pressure-fed, electric pump-fed and turbopump-fed, rocket designs are created for a range of burntimes and their trajectories are simulated. This is done using RocketPy, an open-source, Python-based six-degree-of-freedom simulation tool, which allows for high customisability and parametrisation and can be easily integrated with the rocket sizing tool [69]. The tool has been validated with real flight data from various rockets [70]. The International Standard Atmosphere (ISA) model with no wind is assumed and the drag coefficients of the rockets are computed for a range of Mach numbers up to 25, using a simplified model in RASAero, a COTS aerodynamic and trajectory simulation software for high power rockets [71].

An important consideration when assessing the performance of the rockets is the risk of inertial coupling. In rockets, inertial coupling refers to the resonant interaction where motion in pitch or yaw induces roll motion, and vice versa, caused by aerodynamic or inertial asymmetries and non-rigid body dynamics [72]. This is particularly relevant for liquid-fuelled rockets, whose large tanks allow sloshing, which

further contributes to these instabilities. An example of this is the Stratos III rocket, whose launch failure is thought to have been caused by this phenomenon [73]. An important design parameter that indicates susceptibility to these instabilities is the slenderness of the rocket, represented by the length-to-diameter (LD) ratio. According to Eppenga [72, p. 67], non-rigid body models are not required when LD < 20. This value was used as a requirement for the design of Stratos V [74], and is likewise applied in this study.

Another important parameter is the tower exit velocity (TEV), which is the velocity of the rocket directly after the lowest launch lug[6] leaves the launch rail. A minimum TEV of 30 m/s is required to ensure sufficient dynamic pressure for aerodynamic stabilisation during take-off [74]. The length of the launch rail can be extended to increase the TEV, but is limited to 16 m for practical considerations, such as stiffness and ease of transport. This is in line with the design of DARE's launch tower. Because the lower launch lug is located at the top of the engine bay, for structural reasons, the effective launch rail length is reduced to 15.09 m.

4.4. RPM Selection

After initial design explorations in AxStream, the generated turbine designs were found to be too inefficient. A primary reason for this is the low rotor tip speeds, which are a result of the small diameter and low shaft speed (rotational velocity). To combat this, the decision was made to increase the shaft speed.

While this may result in a more efficient turbine, it is important to consider the effects this has on the efficiency of the pumps, as explained in Section 2.4. For this reason, a design exploration is performed for the pumps, leading to a relationship between the shaft speed and the required pump power. This is discussed in Subsection 4.4.1. Next, a similar design exploration is performed for the turbines in Subsection 4.4.2, where a relationship is made between the shaft speed and ass flow, ultimately leading to a new design point.

4.4.1. Preliminary Pump Design Exploration

The design exploration is performed in AxStream, following a similar approach as for the turbine, which is explained in Subsection 4.5.1. The fluid properties of the propellants and the pump requirements, used as input for the design exploration, were established before in Subsection 4.2.1 and are listed in Table 4.1 and Table 4.2.

To avoid cavitation, a net positive suction head[7] (NPSH) requirement is imposed. The available $NPSH_a$ is found using Equation 4.24 and is dependent on the inlet pressure. A higher tank pressure reduces the risk of cavitation, but increases the mass of the tanks and pressurisation system. A margin of 25% is maintained with respect to the $NPSH_a$, resulting in a required $NPSH_r = NPSH_a/1.25$, leading to 79.7 and 57.2 m for the fuel pump and oxidizer pump, respectively [15].

[6] A launch lug is a protrusion that guides the rocket along the launch rail, ensuring stable ascent.

[7] Net Positive Suction Head (NPSH) is a measure of the pressure margin at the pump inlet, often used to determine the susceptibility to cavitation. The available NPSH ($NPSH_a$) must be higher than the required NPSH ($NPSH_r$). The margin between the two depends on the acceptable level of cavitation. $NPSH_R$ is often specified as the inlet pressure at which a 3% head drop occurs [15].

$$NPSH_a = \frac{p_{t,in}}{g_0 \rho} \tag{4.24}$$

The outcome of this design exploration is shown in Figure 4.17. The minimum power required is reached at 51.8 and 55.1 krpm for the fuel pump and oxidizer pump, respectively.

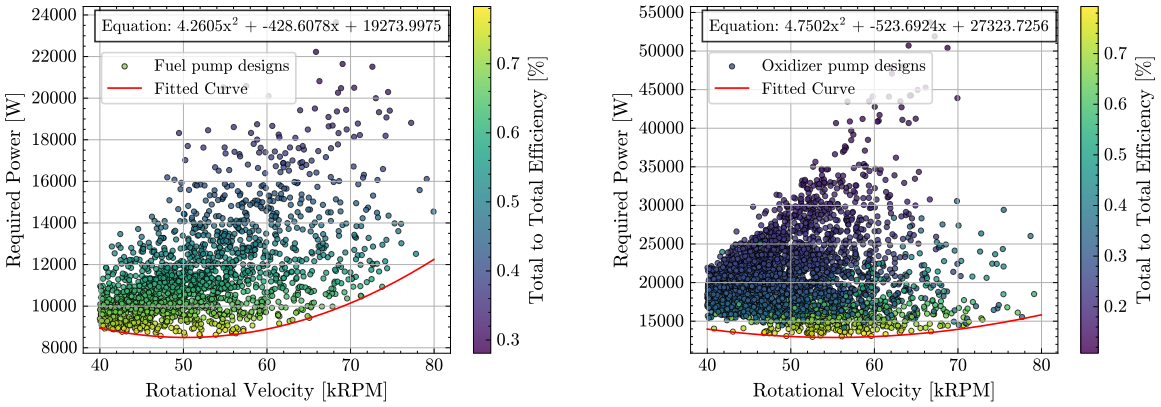

(a) Fuel pump.

(b) Oxidizer pump.

Figure 4.17: Preliminary design exploration of the propellant pumps, showing the required power as a function of the rotational velocity, with a second order polynomial fitted curve along the minimum power pareto front.

4.4.2. Turbine Design Exploration

A new design exploration is performed using the method in Subsection 4.5.1, for the same range of shaft speeds as the pumps. As per *Van Der Lee Turbo Systems*' [56] recommendation, the turbine inlet temperature is increased from 950 ° C to 980 ° C, to increase the power density of the turbines. This temperature and its resultant gas properties (see Subsection 4.2.4) are maintained for all subsequent design explorations and designs. The results, shown in Figure 4.18, are filtered to only include those delivering the required power at that shaft speed, based on the relations in Figure 4.17. While the lowest power requirement occurs at a shaft speed of 53.6 krpm, the ideal shaft speed is shifted to around 70.3 krpm due to the increasing turbine efficiency with respect to shaft speed.

As such, a shaft speed of 70 krpm is used for all subsequent turbine designs, for which a turbine power of 24.4 kW is required.

4.5. Turbine Design in AxStream

This section explains the turbine design methodology. In Subsection 4.5.1, the general methodology for the pump and turbine design explorations is explained. These are used to obtain simplified relationships between the pump or turbine properties, as well as to obtain the final turbine designs assessed in this thesis. The design process of the radial and axial turbines is further detailed in Subsection 4.5.2 and Subsection 4.5.3, respectively.

4.5.1. Design Exploration Methodology

In AxStream, the working fluid is first defined. For the turbines, an ideal gas is used, with the properties as described in Table 4.3. For the pumps, the fluid is defined based on the properties listed in

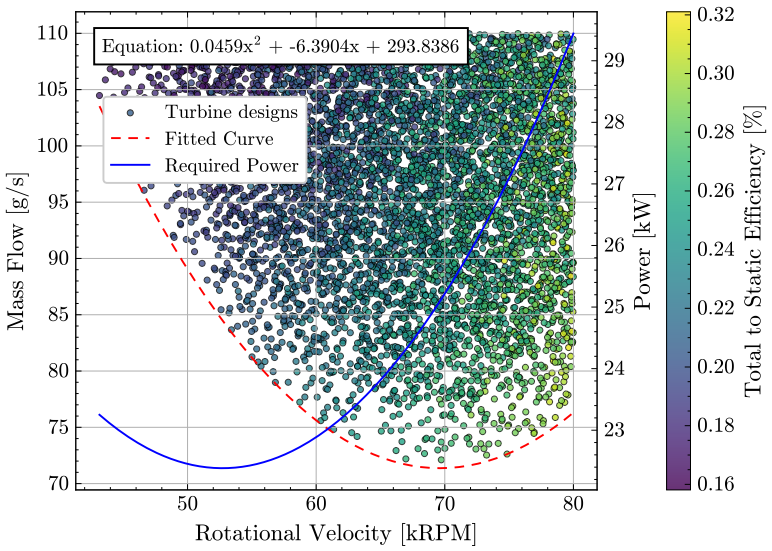

Figure 4.18: Second AxStream design exploration of the RIT. The required mass flow (left y-axis) is shown as a function of rotational velocity, with a second-order polynomial fit to the minimum mass flow Pareto front. Results are filtered by the required power at each velocity. The total required pump power (right y-axis) as a function of rotational velocity is also shown.

Table 4.1.

Then, a large set of pump or turbine geometries is generated in the Preliminary Design module using a preliminary set of input parameters. AxStream then uses an inverse solver to calculate their performance, based on empirical and mathematical models. The Design Space Explorer module is then used to filter out the designs that do not meet the requirements (e.g. turbine power) and to plot various input and output parameters. For the turbines in particular, the influence of the input parameters on the required mass flow is evaluated, based on which the design space is further narrowed down to obtain a dense design space centered around the minimum mass flow. Similarly for the pumps, the design space is narrowed down to optimise for a minimum power requirement.

4.5.2. Radial Inflow Turbine Design

The refined inputs for the vaned and vaneless turbines are listed in Table 4.8-4.9 and are based on the requirements established in Section 4.2.

The parameters for the RITs are largely similar and differ mostly in the pressures and diameters. The outlet static pressure of the vaneless turbine is maintained at 2 bar, to accommodate a choked nozzle, whereas the outlet pressure of the vaned turbine is decreased to 1 bar (absolute pressure), due to the supersonic outlet flow. While higher outlet pressures are allowed, the lowest values resulted in the more feasible results. Note that the inlet flow of the vaneless turbine's rotor was later also found to be supersonic as the flow is choked in the volute. The inlet pressure range was also adjusted accordingly, as a PR of higher than 15 did not yield usable designs. The rotor diameters have been adjusted slightly with respect to the initial estimates. Both turbines prefer a shallow volute exit angle of below 15 deg, i.e. with a large tangential velocity component. The minimum rotor leading edge height has been constrained to 2 mm, to maintain a reasonable rotor clearance-to-blade height ratio of at least 6.7, limiting rotor blade tip leakage.

Table 4.8: Refined AxStream Preliminary Design module inputs for the vaned radial inflow turbine.

Parameter	Min	Max
Boundary conditions		
Inlet total pressure [bar]	5.0	15.0
Inlet total temperature [K]	980.0	980.0
Outlet static pressure [bar]	1.0	1.0
Mass flow rate [kg/s]	0.060	0.075
Metal angle [deg]	0.0	0.0
Shaft rotational speed [rkpm]	70.0	70.0
Parameters		
Stator outlet mean diameter [mm]	50.0	50.0
Rotor blade height ratio (LTE/LLE) [-]	1.0	200.0
Rotor diameter ratio (D_1/D_2) [-]	1.01	3.00
Rotor LE height [mm]	2.0	9.0
Hub reaction [-]	0.01	0.70
Constraints		
Number of stages [-]	1	1
Exit angle of inlet volute [deg]	0.0	15.0
Rotor outlet hub diameter [mm]	10.0	45.0
Stator inlet diameter [mm]	45.0	75.0

After the design exploration, a suitable design is selected which meets the requirements and requires the lowest possible mass flow. Not all generated designs are suitable as-is, as some are generated without volute or feature undesirable geometries, such as a very large volute or unmanufacturable stator throats.

Once a suitable design has been selected, it can be modified and optimised. While most geometrical parameters are left as-is, some are adjusted to improve manufacturability or efficiency, particularly in the stator. After initial CFD simulations, the stator design was adjusted to better match the stator inlet metal angle to the volute exit flow angle, and the stator outlet flow angle to the rotor inlet metal angle, to reduce flow separation along the blade. The stator trailing edge radius is also restricted to 0.3 mm, to make the design more manufacturable.

4.5.3. Axial Turbine Design

The refined inputs for the axial turbine, based on the requirements in Table 4.5, are listed in Table 4.10. The axial turbine design follows a similar process to the RITs, but requires more manual adjustment, as all designs were generated with small rotor blade heights and rotor throat sizes, making them challenging to manufacture. The design space is filtered to remove designs with a blade height of less than 3 mm. Due to the larger rotor tip diameter of around 81-82 mm and low mass flow rate, a balance must be struck between sufficient blade height and throat width, both of which influence the total throat area. The chosen design is adjusted to reduce the blade count by roughly 2/3 to achieve a reasonable throat width. The rotor blade chord length is then also adjusted accordingly, to maintain the same blade

Table 4.9: Refined AxStream Preliminary Design module inputs for the vaneless radial inflow turbine.

Parameter	Min	Max
Boundary conditions		
Inlet total pressure [bar]	8.0	25.0
Inlet total temperature [K]	980.0	980.0
Outlet static pressure [bar]	2.0	2.0
Mass flow rate [kg/s]	0.040	0.055
Metal angle [deg]	0.0	0.0
Shaft rotational speed [krpm]	70.0	70.0
Parameters		
Stator outlet mean diameter [mm]	68.0	68.0
Rotor blade height ratio (LTE/LLE) [-]	1.0	200.0
Rotor diameter ratio (D_1/D_2) [-]	1.01	3.00
Rotor LE height [mm]	2.0	9.0
Hub reaction [-]	0.01	0.70
Constraints		
Number of stages [-]	1	1
Exit angle of inlet volute [deg]	0.0	15.0
Rotor outlet hub diameter [mm]	10.0	45.0
Stator inlet diameter [mm]	45.0	75.0

profile shape (particularly, the same chord to blade pitch ratio).

4.6. CFD Performance Assessment in Ansys CFX

Since the Preliminary Design module in AxStream is based on 1D meanline models, it is not well suited for turbine stages with very high work coefficients such as the ones considered here. As a result, AxStream's performance predictions may deviate substantially from the actual behaviour when applied beyond the typical operating range. Therefore, the performance is to be verified using computational fluid dynamics (CFD) simulations. Additionally, the CFD simulations give a better understanding of the flow behaviour inside the turbines, allowing for further optimisation of the geometry and operational conditions.

Both the vaneless and vaned RIT are simulated. Due to time constraints, the performance of the axial turbine is not verified and is therefore merely used as a preliminary comparison.

4.6.1. Simulation Setup

While AxStream provides its own CFD solver, the Ansys CFX [75] flow solver is used instead, as it is widely regarded as the industry standard for turbomachinery simulations and offers greater flexibility in terms of meshing, solver setup and analysis.

Steady-state Reynolds-averaged Navier-Stokes (RANS) simulations are performed using the Shear Stress Transport (SST) $k-\omega$ model as turbulence closure. During the simulations, the residuals and the mass

Table 4.10: Refined AxStream Preliminary Design module inputs for the axial turbine.

Parameter	**Min**	**Max**
Boundary conditions		
Inlet total pressure [bar]	10.0	25.0
Inlet total temperature [K]	980.0	980.0
Outlet static pressure [bar]	1.0	4.0
Mass flow rate [kg/s]	0.04	0.07
Inlet flow angle [deg]	20.0	40.0
Shaft rotational speed [rpm]	70000.0	70000.0
Parameters		
Mean diameter [mm]	65.0	80.0
Nozzle outlet flow angle near hub A_1 [deg]	14.0	24.0
Hub reaction [-]	0.0	0.2
Module admission ratio [-]	0.1	0.6
Constraints		
Number of stages [-]	1	1
Hub diameter limit [mm]	60.0	80.0
Tip diameter limit [mm]	70.0	83.0
Module axial length limit [mm]	10.0	100.0
Total blades mass [kg]	0.0	1.0

flow error (Equation 4.25) are monitored to evaluate convergence. The simulations are run until the root-mean-square (rms) residuals are reduced by at least 4 orders of magnitude and the absolute mass flow error is below 0.1%. While a higher order residual reduction is desirable, this could not always be achieved, likely due to the high Mach numbers and flow instabilities inside the rotor.

$$\epsilon_{\dot{m}} = \frac{\dot{m}_{out} - \dot{m}_{in}}{\dot{m}_{in}} \tag{4.25}$$

Ideally, real gas models would be employed to better represent the thermodynamic properties of the working fluid at high pressures and temperatures. However, the available real gas models for CO and H_2 are not valid at the turbine inlet temperature. Instead, gas-phase combustion models from the Ansys CFX material library are used, which approximate the real gas heat capacities using NASA SP-273 polynomial fits [76]. A fixed composition gas mixture is then defined, based on the mass fractions listed in Table 4.4.

Both RITs are modelled with the volute present, with a total pressure boundary condition (BC) applied at the inlet. The vaned turbine has an exhaust duct placed at the turbine exit. For the vaneless turbine, two separate cases are considered: one with a straight outlet duct, similar to the vaned turbine, and one with a choked nozzle. In the former case, a static outlet pressure BC of 2 bar is applied, whereas in the latter case, a static outlet pressure BC of 1 bar is applied. Due to time constraints, the configuration with the outlet nozzle has not been simulated and is therefore left for future work. To mitigate flow separation, shocks or unsteady phenomena at the rotor exit, a hemispherical hub cap is modelled in the

duct and nozzle domains, rotating with the rotor. An example of the setup for the vaned turbine is shown in Figure 4.19.

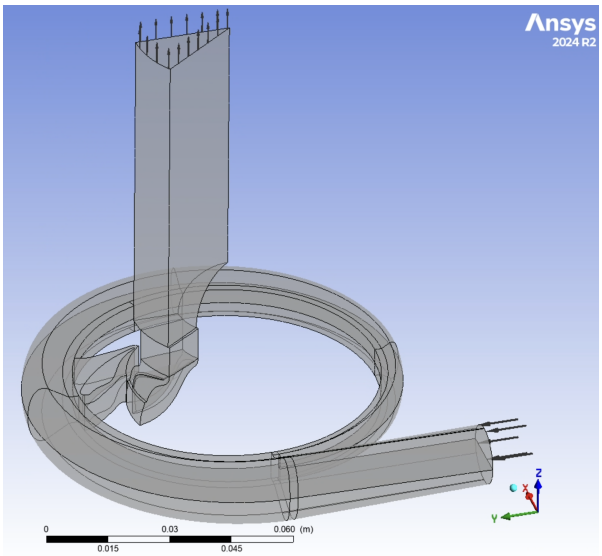

Figure 4.19: Computational domains of the vaned turbine in Ansys CFX, showing the volute, stator sector, rotor sector and outlet duct sector domains.

A frozen rotor interface is used between non-rotating domains, i.e. between the volute and stator. Between domains with relative motion, a mixing plane interface is used, with a pressure profile decay of 0.05 and implicit stage averaging.

Finally, to assess turbine performance under flight conditions, the turbines are evaluated at both sea-level conditions and near-vacuum conditions: $p_{out} = 0.11609$ bar, corresponding to the engine burn-out altitude, according to the trajectory simulations (see Section 5.1). The turbines are also evaluated at double the nominal shaft speed (140 krpm), to assess the influence of rotational velocity, and to assess the hypothesis that a higher shaft speed should result in a higher efficiency for this turbine.

4.6.2. Meshing

The stator and rotors are exported as single blade sectors and meshed in Ansys Turbogrid [77]. The meshes use proportional control, allowing the element count to be easily adjusted. Within the passage, a proportional spanwise blade distribution method is used, with proportionality factors of 1.1 and 1.5 for the rotors and stator, respectively. The inlets and outlets are defined using an H-grid with an expansion rate of 1.2 and a targeted maximum aspect ratio of 600. At the rotor blade tip near the shroud, matched expansion is applied. For boundary layer refinement, a first element offset of $y^+ = 1$ is imposed. Based on the mesh refinement study in Subsection 4.6.3, 1.6×10^6 elements are used for both rotors, and 0.6×10^6 elements for the stator.

The volutes are meshed in Ansys Meshing [78] with lower fidelity, as they are not the primary region of interest and are not expected to feature high turbulence or flow separation. To reduce element count and computational cost, the volutes are sliced in half and later mirrored. They are meshed with a 1 mm default element size and a growth rate of 1.15. An inflation of 12 layers with a first layer height of 0.01 mm is applied to the wall of the volute and the volute outlet, to better resolve the boundary layer and

volute-stator or volute-rotor interface. The volute cutwater is further refined using face sizing with an element size of 0.1-0.5 mm.

Similarly, the ducts and nozzle are divided into 10 axisymmetric sectors to reduce computational cost. They are meshed with a 1 mm default element size and inflation around the walls.

4.6.3. Mesh Refinement Study

A mesh refinement study is performed to assess the results' sensitivity to mesh density. The volute inlet mass flow, total-static efficiency η_{ts} (Equation 4.26), thermodynamic power P_{therm} (Equation 4.27) and mechanical power P_{mech} (Equation 4.28) are used as comparison metrics. The results of all simulations in this study are normalised with respect to the results of the finest mesh.

$$\eta_{ts} = \frac{h_{t,in} - h_{t,out}}{h_{t,in} - h_{out,is}} \tag{4.26}$$

$$P_{therm} = \dot{m}\left(h_{t,in} - h_{t,out}\right) \tag{4.27}$$

$$P_{mech} = \tau_{blade} N_{blades} \omega \tag{4.28}$$

where τ_{blade} is the torque subjected to a single blade and N_{blades} is the total number of rotor blades.

For the vaneless rotor, element counts between 0.8×10^6 and 4×10^6 are considered, for which the results are shown in Figure 4.20a. Simulations are performed at the nominal operating point, with a straight duct and outlet static pressure of 2 bar.

The 1.6×10^6 element rotor is considered to provide a good balance between accuracy and low computational cost, with an error of less than 1%. For the vaned rotor, the same element count is used to save time. This is considered acceptable, as the average element height $h_{element,avg}$, computed using Equation 4.29, deviates only 1.46% from the vaneless rotor [20].

$$h_{element,avg} = \sqrt[3]{\frac{V_{domain}}{n_{elements}}} \tag{4.29}$$

where V_{domain} is the volume of the considered rotor sector domain and $n_{elements}$ is the number of elements in said domain.

The same analysis is carried out for the stators, with element counts ranging from 0.3×10^6 to 2×10^6 , for which the results are shown in Figure 4.20b. The 0.6×10^6 element stator is considered optimal, with an error of less than 0.75%.

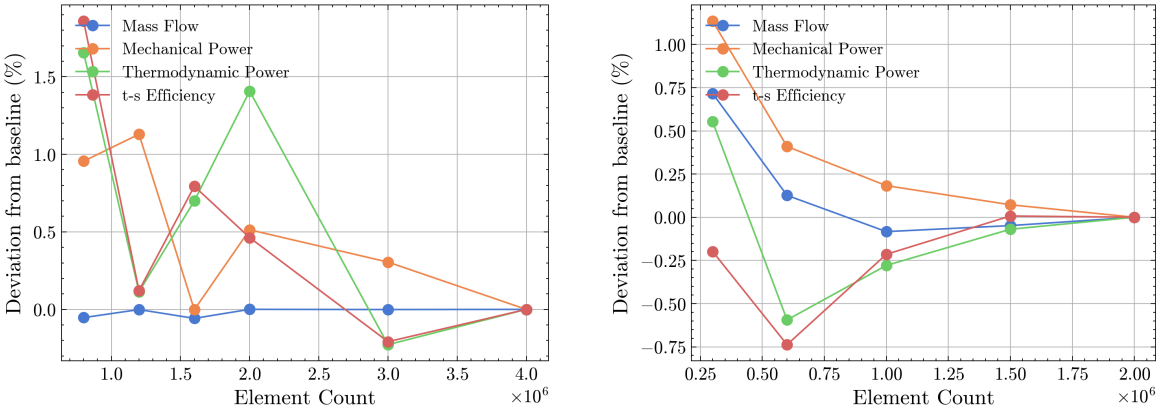

(a) Vaneless turbine rotor.

(b) Vaned turbine stator.

Figure 4.20: Convergence plots for the vaneless turbine rotor and the vaned turbine stator, showing the performance metrics normalised with respect to the results of the finest mesh.

5

Results and Discussion

This chapter presents the results of the work described in Chapter 4. In Section 5.1, the results of the system-level trade study are presented, which lead to the chosen turbine design point. Section 5.2 presents the selected turbine designs, generated by AxStream. As explained in Section 4.6, only the RITs have been evaluated in Ansys CFX due to time constraints. Section 5.3 presents the CFD results at the nominal operating point, i.e. at sea-level outlet conditions and with a shaft speed of 70 krpm, as decided on in the shaft speed trade-off. The CFD results for near-vacuum outlet pressure, corresponding to the atmospheric conditions of the rocket at engine burn-out, are presented in Section 5.4. Since the generated turbine designs feature higher-than-recommended duty coefficients, CFD simulations are also performed at double the shaft speed of 140 krpm, for which the results are also shown in Section 5.4.

5.1. System-Level Trade Study Results

This section presents the results of the system-level trade study. For brevity, only the full results of the turbopump-fed rockets are shown, as well as a comparison with the other rocket cycles. A full overview of the results for all rocket cycles can be found in Appendix A.

The results for the turbopump-fed rockets using the turbine relations obtained through AxStream and Mounier et al.'s work are shown in Figure 5.1 and Figure 5.2, respectively. Due to the large similarities, only the relevant results are shown for the latter.

Figure 5.1a shows the simulated apogee (i.e., the maximum altitude reached by the rocket) as a function of the burntime for varying rocket diameters. As expected, rockets with smaller diameters benefit from lower aerodynamic drag due to their decreased frontal area, leading to higher apogees. However, this advantage becomes less significant due to the imposed length-diameter (LD) ratio limit of 20. As this constraint limits the total rocket length for a given rocket diameter, and thus the volume of the propellant tanks, the burntime is limited as well. As a result, slender rockets may not fully benefit from their aerodynamic advantage.

Similarly, rockets with larger diameters can feature much larger tanks before reaching the LD ratio limit, therefore carrying more propellant to increase the burntime and altitude. At those longer burntimes, however, they eventually become limited by the minimum tower exit velocity (TEV) requirement due

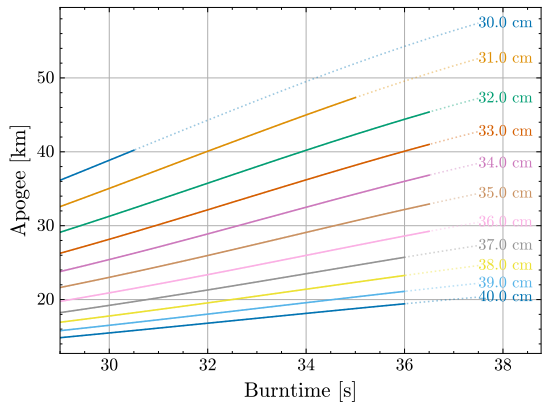

(a) Simulated apogee as a function of burntime, for varying rocket diameters. Dotted lines represent the apogee achieved without limitations, whereas solid lines are limited by the imposed TEV and LD ratio requirements.

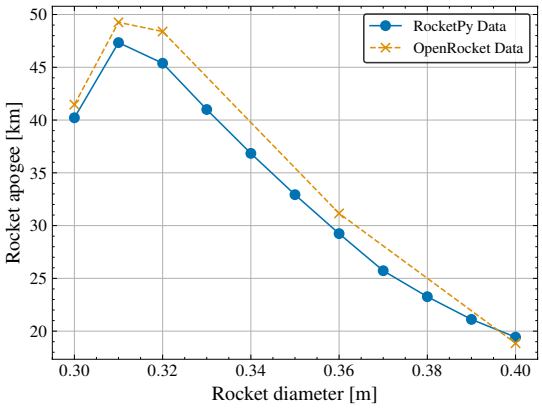

(b) Maximum simulated apogee as a function of rocket diameter, with verification data obtained through OpenRocket.

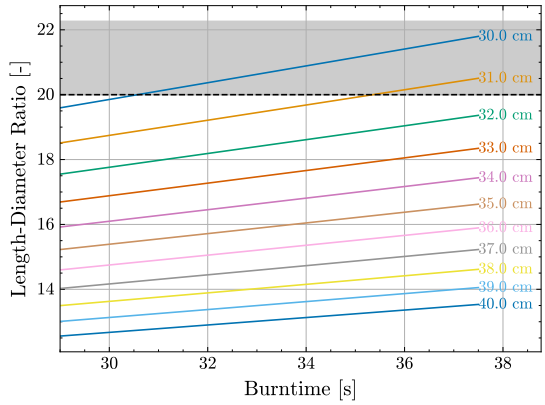

(c) LD ratio as a function of burntime, for varying rocket diameters. The grey area represents the maximum LD ratio requirement of 20.

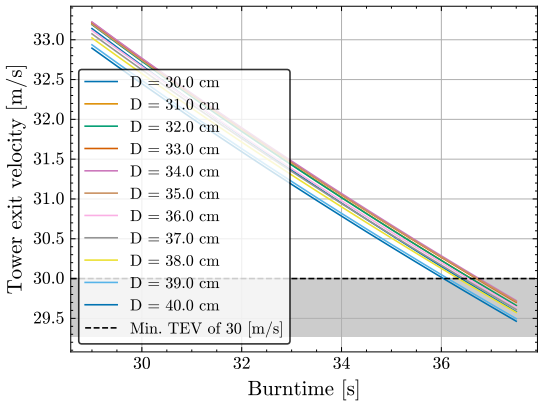

(d) Tower exit velocity (TEV) as a function of burntime, for varying rocket diameters. The grey area represents the minimum TEV requirement of 30 m/s.

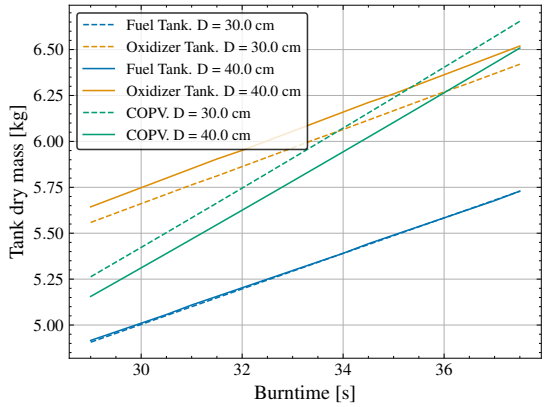

(e) Tank dry masses as a function of burntime, for varying rocket diameters.

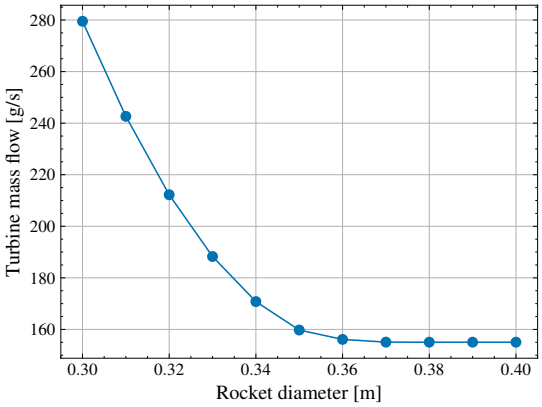

(f) Estimated turbine mass flow as a function of rocket diameter (AxStream).

Figure 5.1: System-level trade study results for the turbopump-fed rockets, using the relations obtained through AxStream.

to their higher mass at lift-off[1]. These limitations are illustrated in Figure 5.1c and Figure 5.1d, which show the LD and TEV as a function of burntime, for varying rocket diameters.

[1]This is because the TEV is primarily dependent on the thrust-weight ratio of the rocket, assuming a fixed rail length.

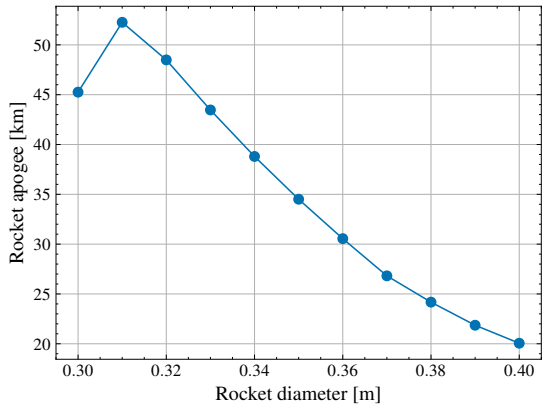

(a) Maximum simulated apogee as a function of rocket diameter, with verification data obtained through OpenRocket.

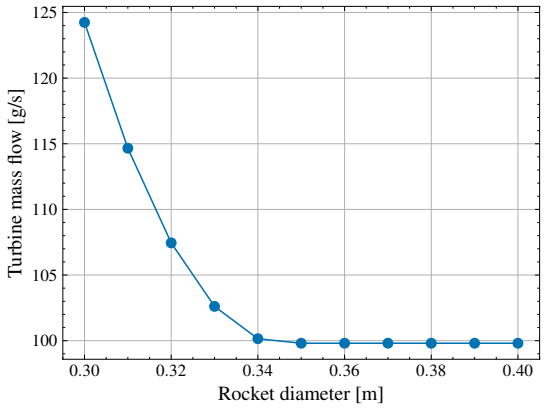

(b) Estimated turbine mass flow as a function of rocket diameter (Mounier et al.).

Figure 5.2: System-level trade study results for the turbopump-fed rockets, using the relations obtained through Mounier et al.'s methods.

The tank dry masses are shown in Figure 5.1e. As seen in Figure 5.1f and Figure 5.2b, the required turbine mass flows converge to a minimum value of 155 g/s and 100 g/s for a rocket diameter of 37 cm and 35 cm for the rockets using the AxStream relations and Mounier et al.'s relations, respectively.

Nonetheless, as seen in Figure 5.1b and Figure 5.1b, the maximum apogee is in both cases still reached with a small rocket diameter of 31 cm, due to the significant influence of the rocket diameter on the drag experienced throughout the flight. At this diameter, the estimated turbine mass flows are 243 g/s and 115 g/s for the rockets, resulting in an engine I_{sp} of 226.6 s and 233.3 s (baseline: 239.7 s) and an apogee of 47.3 km and 52.3 km, using the AxStream relations and Mounier et al.'s relations, respectively.

For the former case, the same simulations have been performed in OpenRocket with the same geometrical parameters as the winning configuration for several rocket diameters, to verify RocketPy's simulation results. These are also shown in Figure 5.1b. As seen there, the verification data is slightly more optimistic, with a maximum deviation of 4.06%, but closely resembles RocketPy's results. Importantly, the same general trend is observed, with the 31 cm rocket reaching the highest apogee, despite the higher turbine mass flow.

A comparison of the different rocket cycles is shown in Figure 5.3. The pressure-fed rocket is simulated with both a conservative LOx tank ullage temperature of 90 K and a more realistic temperature of 150 K[2]. The pressure-fed rockets achieve a much lower apogee of at most 14.3 and 18.3 km, respectively. The former case is limited by the maximum burntime of 21 s, due to the size of the COPV. The latter, with a more forgiving assumption, can reach higher burntimes, but is instead mainly limited by the combination of high LD ratios (due to the large COPV) and low TEVs (due to the high tank and pressurisation system masses).

The electric pump-fed rockets, on the other hand, fare very well against the turbopump-fed rockets, with a maximum apogee of 48.7 km, in-between the two predicted maximum apogees of the turbopump-fed rockets. This means that, in order for the turbopump-fed rocket to attain superior performance to

[2]As explained in Subsection 4.3.2, if the pressurant mixes well with the cold ullage, its density increases, requiring more pressurant to account for the pressure loss. This limits the burntime that is attainable with the given COPV. Two ullage temperatures are considered, to represent both the worst-case scenario and a more reasonable case.

the electric pump-fed rocket, a much lower turbine mass flow is required. Specifically, with a rocket diameter of 31 cm, a mass flow of at most 222 g/s is required to attain the same apogee as the electric pump-fed rocket, with a 35.5 s burntime.

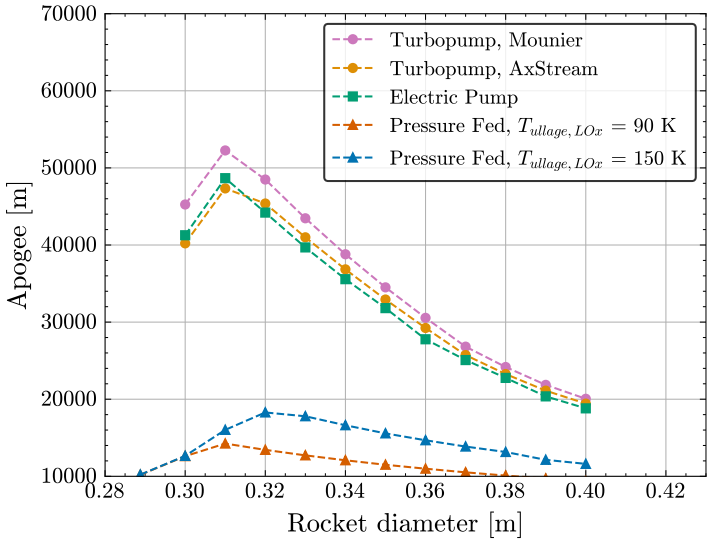

Figure 5.3: Comparison of the maximum predicted apogee as a function of burntime, for different rocket cycles. The pressure-fed cycle is simulated assumed LOx tank ullage temperatures of 90 K and 150 K.

5.2. Turbine Designs in AxStream

As a result of the system-level trade study in Section 5.1, a rocket diameter of 31 cm is chosen. Based on this, the turbines can be designed in AxStream. The design of the vaned RIT, vaneless RIT and axial turbine are presented in Figures 5.2.1-5.2.3.

5.2.1. Vaned Radial Inflow Turbine

Figure 5.4 shows the final design space for the vaned radial inflow turbine (RIT), generated using AxStream. The design space has been filtered to include only designs with a minimum power output of 24.4 kW and a total-to-static efficiency of at least 30%. Designs that do not meet these requirements are plotted with reduced opacity for context. The selected design is indicated in red.

A 3D view and meridional view of the selected vaned RIT design are shown in Figure 5.5 and Figure 5.6. A comparison between the original stator and new stator is shown in Figure 5.7. The relevant geometrical properties are summarised in Table 5.1, followed by the performance parameters estimated by AxStream in Table 5.2. As the size of the volute and stator are larger than initially estimated, the rotor diameter is made smaller than the value that followed from Subsection 4.3.1, at roughly 48 mm compared to 55 mm, to ensure that the turbine can still fit within the rocket.

The turbine features a low total inlet pressure of only 8.15 bar, which results in an equal total-to-static pressure ratio of 8.15 due to the 1 bar outlet static pressure. A relatively low mass flow of 73.0 g/s is required, below the initial estimates that resulted from the system-level trade study, despite the low total-to-static efficiency of 31.2%. The duty coefficients of $(\psi_2, \phi_2) = (20.1, 2.1)$ at the rotor inlet are significantly higher than the maximum duty coefficients of $(\psi_{2,opt}, \phi_{2,opt}) \approx (1.3, 0.43)$ for supersonic

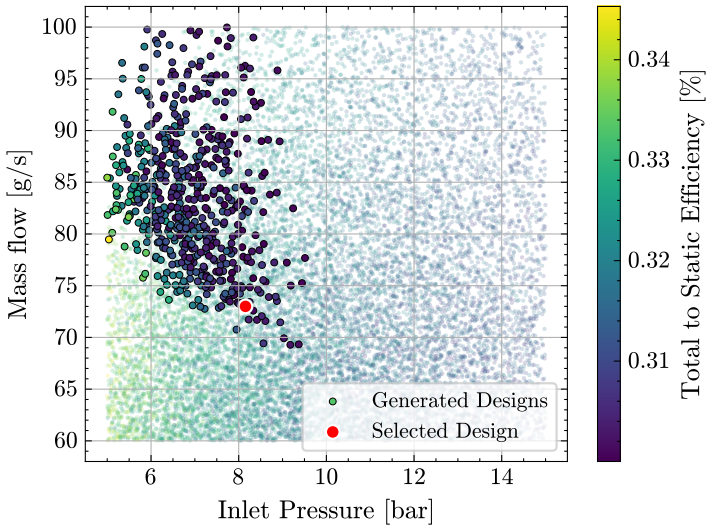

Figure 5.4: Filtered design space for the vaned radial inflow turbine, generated using AxStream. Designs meeting the minimum requirements (24.4 kW power and 30% total-to-static efficiency) are shown with full opacity. The selected design point is indicated in red.

ORC RITs[3] recommended by Majer et al. [79, p. 55]. This is largely caused by the low rotor tip speed U of 175 m/s. Combined with the high isentropic spouting velocity due to the high pressure ratio and high $T_{t,in}$ (as per Equation 5.1 [21]), the low tip speed leads to an isentropic velocity ratio of 0.088 that is noticeably lower than the ideal value of $U/C_0 = 1/\sqrt{2} \approx 0.707$ recommended by Dixon and Hall [21, p. 326].

$$C_0 = \sqrt{2\Delta h_{is}} = \sqrt{2c_p T_{t,in}\left(1 - \left(\frac{p_{out}}{p_{t,in}}\right)^{(\gamma-1)/\gamma}\right)} \tag{5.1}$$

As some turbines are predicted to generate a higher power output than others, a specific fuel consumption metric SFC is used, as defined in Equation 5.2, equal to 2.856 g/(kW s) for this turbine.

$$SFC = \frac{\dot{m}_{turbine}}{P_{therm}} \tag{5.2}$$

5.2.2. Vaneless Radial Inflow Turbine

Figure 5.11 shows the final design space for the vaned RIT. Once again, the design space has been filtered to include only designs with a minimum power output of 24.4 kW and a total-to-static efficiency of at least 30%. Designs that do not meet these requirements are plotted with reduced opacity for context. While turbine designs with lower mass flows were generated, not all designs resulted in feasible geometries and some were generated without volute, requiring some manual filtering. Like before, the rotor diameter was maximised, while ensuring the turbine can still fit within the rocket, leading to a 68 mm diameter. The final selected design is indicated in red.

[3]While the exact values recommended by Majer et al. [79, p. 55] are dependent on several design parameters and specifically tailored towards ORC applications, the values presented here are valid for low molecularly complex fluids (in this case with γ = 1.15) and high volume ratios.

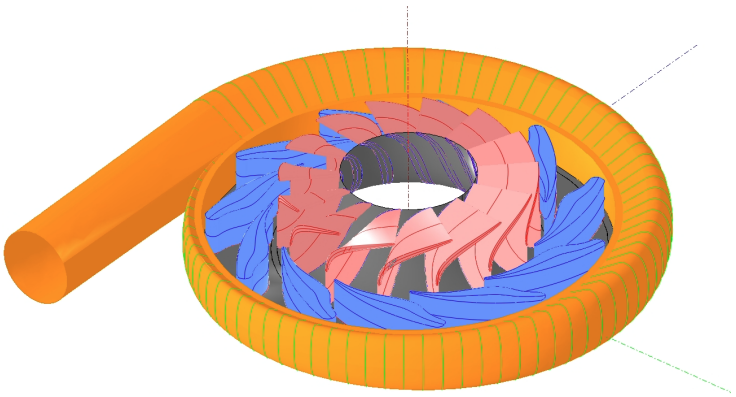

Figure 5.5: 3D view of the selected vaned radial inflow turbine in AxStream.

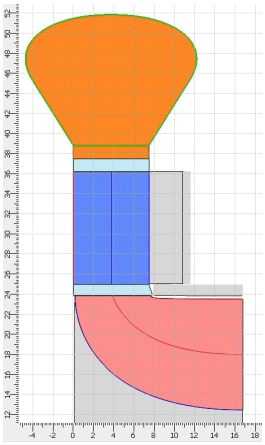

Figure 5.6: Meridional view of the selected vaned radial inflow turbine in AxStream.

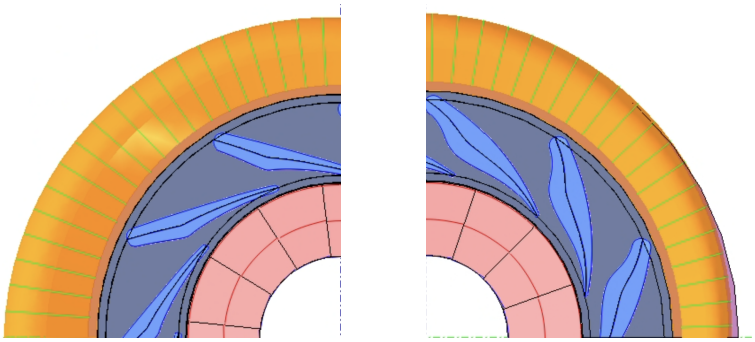

(a) Original stator. **(b)** New stator.

Figure 5.7: Comparison of the original stator design generated by AxStream and the adjusted stator.

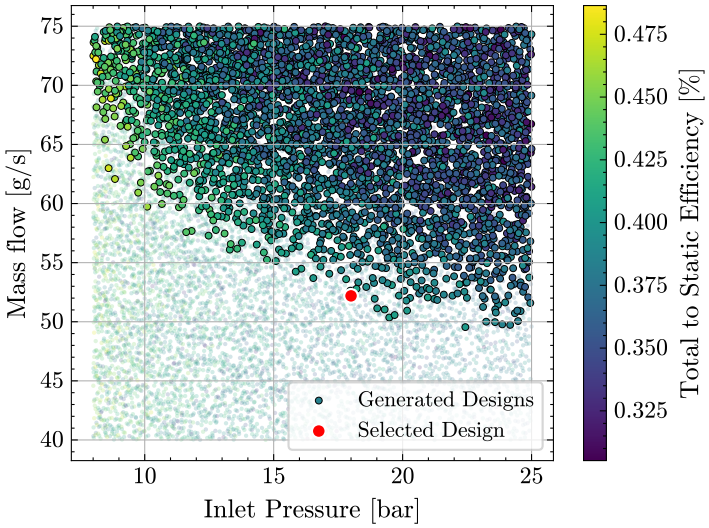

Figure 5.8: Filtered design space for the vaneless radial inflow turbine, generated using AxStream. Designs meeting the minimum requirements (24.4 kW power and 30% total-to-static efficiency) are shown with full opacity. The selected design point is indicated in red.

Table 5.1: Geometrical properties of the selected vaned radial inflow turbine design. Angles are defined wrt. the normal.

Property	Value
Number of rotor blades [-]	14
Rotor inlet diameter D_2 [mm]	47.76
Rotor outlet tip diameter D_{3s} [mm]	47.07
Rotor outlet hub diameter D_{3h} [mm]	24.94
Rotor blade height at inlet b_2 [mm]	7.48
Rotor blade height at outlet b_3 [mm]	11.07
Rotor axial length L_{ax} [mm]	16.90
Rotor tip-shroud clearance [mm]	0.3
Rotor inlet metal angle β_2[deg]	0.00
Rotor outlet metal angle β_3 [axial deg]	78.42
Rotor throat width at midspan [mm]	1.622
Number of stator vanes [-]	11
Stator inlet diameter D_0 [mm]	72.44
Stator outlet diameter D_1 [mm]	50.00
Stator inlet metal angle β_0 [deg]	55.00
Stator outlet metal angle β_1 [deg]	70.00
Stator throat width [mm]	2.31

Table 5.2: Performance properties of the vaned radial inflow turbine, predicted by AxStream's preliminary design module.

Property	Value
Rotational velocity ω [krpm]	70
Rotor tip speed U [m/s]	175.05
Inlet total pressure $p_{t,in}$ [bar]	8.15
Outlet static pressure p_{out} [bar]	1.00
Total-static pressure ratio PR [-]	8.15
Inlet total temperature $T_{,in}$ [K]	1253.15
Outlet total temperature $T_{t,out}$ [K]	1117.45
Mass flow rate $\dot{m}_{turbine}$[g/s]	73.00
Power output $P_{turbine}$ [kW]	25.556
Specific speed N_S [-]	0.183
Specific fuel consumption SFC [g/(kW s)]	2.856
Total-static efficiency η_{ts} [%]	31.20
Work coefficient ψ_2 [-]	20.090
Flow coefficient ϕ_2 [-]	2.144
Isentropic velocity ratio U/C_0 [-]	0.088

A 3D view and meridional view of the selected vaneless radial inflow turbine design are shown in Figure 5.9 and Figure 5.10. The relevant geometrical properties are summarised in Table 5.3, followed by the performance parameters estimated by AxStream in Table 5.4.

While the vaneless turbines in this design space generally feature higher efficiencies at lower inlet pressures and higher mass flows, similarly to the vaned ones, the lowest mass flow is still achieved at a higher inlet pressure. Additionally, the vaneless turbines allow for much higher inlet pressures (with the given requirements), resulting in even lower mass flows. With an inlet pressure of 18 bar and an outlet pressure of 2 bar, a total-to-static pressure ratio of 9 is reached, only slightly higher than the vaned turbine ($PR = 8$). As seen in Figure 5.9, the turbine has a rather unconventional design, which can be attributed to the low mass flow, high inlet pressure and large diameter, which lead to a considerably lower rotor inlet blade height and smaller volute.

The vaneless turbine requires a mass flow of only 52.2 g/s, around 21 g/s lower than the vaned turbine, resulting in a 28% lower specific fuel consumption of 2.071 g/(kW s). This can be largely attributed to the larger rotor diameter, which results in a higher tip speed of 249 m/s and a higher isentropic velocity ratio. The flow coefficient of 0.75 is much closer to the recommended range, while the work coefficient of 18 is only slightly lower than the vaneless turbine. As a result, the total-to-static efficiency, while still low, is around 10 percentage points higher than the vaned RIT, at 41.5%.

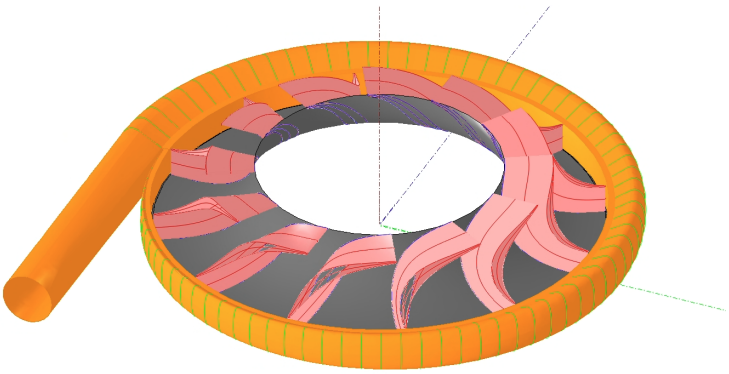

Figure 5.9: 3D view of the selected vaneless radial inflow turbine in AxStream.

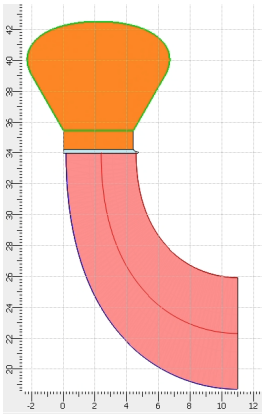

Figure 5.10: Meridional view of the selected vaneless radial inflow turbine in AxStream.

Table 5.3: Geometrical properties of the selected vaneless radial inflow turbine design. Angles are defined wrt. the normal.

Property	Value
Number of rotor blades [-]	12
Rotor inlet diameter D_2 [mm]	68.00
Rotor outlet tip diameter D_{3s} [mm]	51.89
Rotor outlet hub diameter D_{3h} [mm]	37.43
Rotor blade height at inlet b_2 [mm]	4.42
Rotor blade height at outlet b_3 [mm]	7.23
Rotor axial length L_{ax} [mm]	10.85
Rotor tip-shroud clearance [mm]	0.3
Rotor inlet metal angle β_2[deg]	0.00
Rotor outlet metal angle β_3 [axial deg]	84.68
Rotor throat width at midspan [mm]	1.085

Table 5.4: Performance properties of the vaneless radial inflow turbine, predicted by AxStream's preliminary design module.

Property	Value
Rotational velocity ω [krpm]	70
Rotor tip speed U [m/s]	249.23
Inlet total pressure $p_{t,in}$ [bar]	18.00
Outlet static pressure p_{out} [bar]	2.00
Total-static pressure ratio PR [-]	9.00
Inlet total temperature $T_{t,in}$ [K]	1253.15
Outlet total temperature $T_{t,out}$ [K]	1066.02
Mass flow rate $\dot{m}_{turbine}$[g/s]	52.19
Power output $P_{turbine}$ [kW]	25.193
Specific speed N_S [-]	0.091
Specific fuel consumption SFC [g/(kW s)]	2.071
Total-static efficiency η_{ts} [%]	41.46
Work coefficient ψ_2 [-]	18.017
Flow coefficient ϕ_2 [-]	0.745
Isentropic velocity ratio U/C_0 [-]	0.107

5.2.3. Axial Turbine

Figure 5.11 shows the final design space for the axial turbine. The design space has been filtered to include only designs with a minimum power output of 24.4 kW and a total-to-static efficiency of at least 30%. Designs that do not meet these requirements are plotted with reduced opacity for context. The selected design is indicated in red.

A 3D view and meridional view of the selected axial turbine design are shown in Figure 5.12 and Figure 5.13. The relevant geometrical properties are summarised in Table 5.5, followed by the performance parameters estimated by AxStream in Table 5.6.

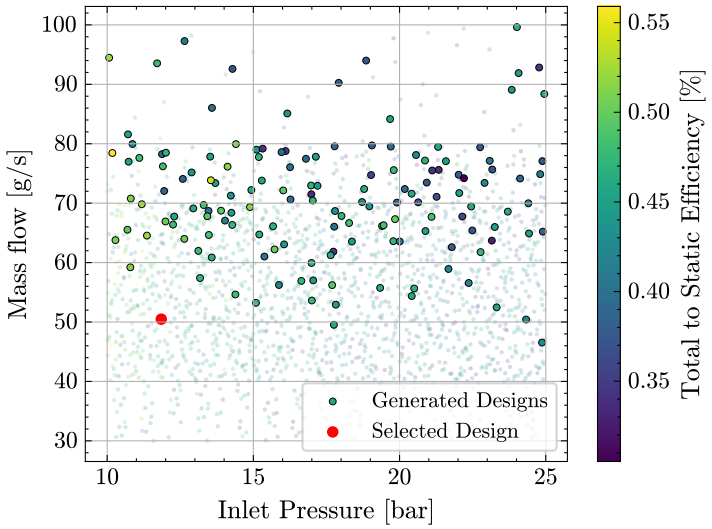

Figure 5.11: Filtered design space for the axial turbine, generated using AxStream. Designs meeting the minimum requirements (24.4 kW power and 30% total-to-static efficiency) are shown with full opacity. The selected design point is indicated in red.

Due to the axial placement of the volute (for which AxStream did not generate any geometry), the axial turbine tip diameter has been increased to 82.7 mm, resulting in a tip speed of 302 m/s. While a similar or slightly lower mass flow could be achieved at different inlet pressures, a design with a lower inlet total pressure of 11.85 bar was selected, as it resulted in stator and rotor blades that are more favourable for manufacturing and feature lower clearance-to-blade-height ratios, compared to the other generated designs with similar performance. This design also features a higher outlet static pressure of 3.43 bar, resulting in a relatively low pressure ratio of 3.45.

As explained in Subsection 4.5.3, the geometry of the selected design was further adjusted in AxStream to ensure that it meets the manufacturing requirements. Specifically, the rotor blade count is reduced and the chord length is adjusted accordingly. This is because the combination of larger diameter and low mass flow rate results in either low blade heights, small throats, or both. The stator has not been adjusted, as the partial admission ratio of 0.23 allows for a larger stator throat width of 2.98 mm at the midspan.

The axial turbine features similar performance to the vaneless turbine, with a mass flow of 50.5 g/s, total-to-static efficiency of 51.8% and specific fuel consumption of 2.0 g/(kW s). Due to the higher blade tip speed of $U = 302$ m/s and the lower pressure ratio (leading to a lower Δh_{is}), the duty coefficients are more reasonable at $(\psi_2, \phi_2) = (6.42, 1.21)$, while Dixon and Hall [21, p. 150] recommend $\psi_2 = 2$ and $\phi_2 < 0.2$ for axial impulse turbines. Naturally, the isentropic velocity ratio has also increased to 0.2, roughly twice that of the vaneless turbine.

5.3. CFD Results at Nominal Operating Point

This section presents the CFD results of the RITs at nominal design conditions, i.e. at 70 krpm and with an outlet static pressure of 1 bar[4]. The results for the vaned and vaneless RIT are presented and discussed in Subsection 5.3.1 and Subsection 5.3.2, respectively.

[4]While an outlet static pressure of 1 atm = 1.01325 bar would be more representative of sea-level conditions, this difference is considered negligible for this analysis and 1 bar has been used for simplicity.

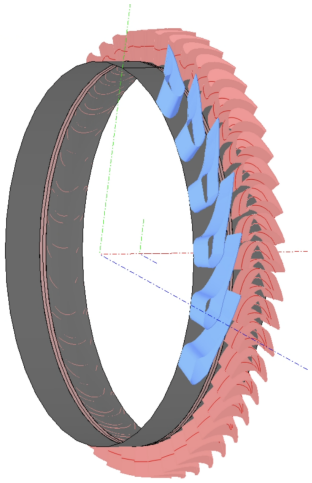

Figure 5.12: 3D view of the selected axial turbine in AxStream.

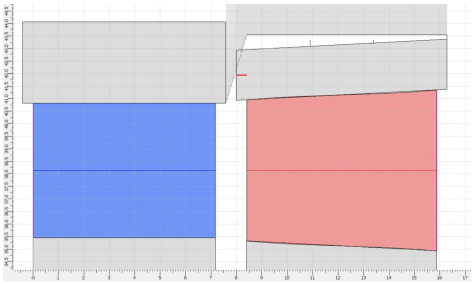

Figure 5.13: Meridional view of the selected axial turbine in AxStream.

Table 5.5: Geometrical properties of the selected axial turbine design. Angles are defined wrt. the rotation axis.

Property	Value
Number of rotor blades [-]	48
Rotor inlet tip diameter D_{2s} [mm]	81.90
Rotor outlet tip diameter D_{3s} [mm]	82.70
Rotor inlet hub diameter D_{2h} [mm]	70.65
Rotor outlet hub diameter D_{3h} [mm]	69.86
Rotor blade height at inlet b_2 [mm]	5.625
Rotor blade height at outlet b_3 [mm]	6.42
Rotor chord c [mm]	7.47
Rotor tip-shroud clearance [mm]	0.3
Rotor inlet metal angle β_2[deg]	68.51
Rotor outlet metal angle β_3 [axial deg]	-72.36
Rotor throat width at midspan [mm]	1.51
Admission ratio [-]	0.23
Number of stator vanes [-]	6
Stator tip diameter D_{0s} [mm]	81.65
Stator hub diameter D_{0h} [mm]	70.91
Stator blade height b_0 [mm]	5.37
Stator inlet metal angle β_0 [deg]	0.00
Stator outlet metal angle β_1 [deg]	73.30
Stator throat width at midspan [mm]	2.98

Table 5.6: Performance properties of the axial turbine, predicted by AxStream's preliminary design module.

Property	Value
Rotational velocity ω [krpm]	70
Rotor tip speed (at mid-chord) U [m/s]	301.65
Inlet total pressure $p_{t,in}$ [bar]	11.85
Outlet static pressure p_{out} [bar]	3.43
Total-static pressure ratio PR [-]	3.45
Inlet total temperature $T_{t,in}$ [K]	1253.15
Outlet total temperature $T_{t,out}$ [K]	785.45
Mass flow rate $\dot{m}_{turbine}$[g/s]	50.48
Power output $P_{turbine}$ [kW]	25.284
Specific speed N_S [-]	0.097
Specific fuel consumption SFC [g/(kW s)]	2.000
Total-static efficiency η_{ts} [%]	51.80
Work coefficient ψ_2 [-]	6.42
Flow coefficient ϕ_2 [-]	1.208
Isentropic velocity ratio U/C_2 [-]	0.200

5.3.1. Vaned Radial Inflow Turbine Results

The results of the CFD simulations of the vaned RIT are summarised and compared to AxStream's results in Table 5.7. Like in Subsection 4.6.3, both the thermodynamic power P_{therm} (Equation 4.27) and

mechanical power P_{mech} (Equation 4.28) are evaluated. Parameters that are evaluated at specific stations are mass flow averaged. The total-to-static efficiency (Equation 4.26) and thermodynamic power are evaluated with the volute inlet and duct outlet as reference inlet and outlet stations. The produced thermodynamic and mechanical power are within 5% of the predicted power, but a significantly higher mass flow of 103.56 g/s is required to reach this point, resulting in a 49.7% higher specific fuel consumption SFC (calculated using P_{therm}). The total-to-static efficiency is 9.6 percentage points lower than predicted, at 21.6%. This mass flow results in a rocket apogee of 54.8 km, around 2.5 km or 4.9% higher than the highest turbopump-fed apogee found in Section 5.1.

Table 5.7: Comparison of the performance parameters of the vaned radial inflow turbine, found through CFD simulations and AxStream. N/A represents parameters not available in AxStream.

Property	**CFD**	**AxStream**
Outlet total temperature $T_{t,out}$ [K]	1151.06	1117.45
Outlet static temperature T_{out} [K]	1047.94	N/A
Mass flow rate $\dot{m}_{turbine}$[g/s]	103.56	73.00
Thermodynamic Power P_{therm} [kW]	24.341	25.556
Mechanical Power P_{mech} [kW]	24.584	25.556
Specific fuel consumption SFC (therm.) [g/(kW s)]	4.212	2.856
Total-static efficiency η_{ts} [%]	21.60	31.20
Rotor tip leakage $\dot{m}_{leak}$ [g/s]	14.98	0

The main contributing factor to the reduced efficiency is the significant flow separation in the stator and rotor passage, which AxStream is not expected to account for. This is easily visualised by plotting streamlines and Mach number contours as well as the normalised[5] entropy contours along the mid-span blade-to-blade surface, see Figure 5.14-5.17. As can be seen here, the flow already attains a very high (tangential) velocity in the volute and reaches the stator at a shallow angle of $\beta_0 = 76.5°$. As the stator inlet metal angle of 55 does not match this flow angle, a large recirculation zone appears on the suction side of the stator, causing a large static entropy increase.

Similarly, the flow exits the stator at a shallow angle of $\beta_1 = 76.5$ and enters the rotor with a relative flow inlet angle of $\beta_2 = 69.6$. This is in part due to the low tip speed $U_0 = 175.1$ m/s. More importantly, though, due to the stator geometry generated by AxStream, the asymmetric diverging section of the stator does not adequately guide the flow, resulting in a more tangential outflow than designed for. As a result, another large recirculation zone appears on the suction side of the rotor, where again a large static entropy increase can be observed.

Another possible contributing factor to lower efficiency could be the leakage from the pressure side to the suction side of the rotor, through the 0.3 mm blade tip to shroud clearance. While AxStream did not predict any leakage, the CFD simulations show a 14.98 g/s blade tip leakage; 14.46% of the total mass flow. However, as explained in Subsection 5.3.2, this leakage flow may not have as much of an impact for this particular turbine as it normally would. For the vaneless turbine, which features a proportionally higher leakage rate than the vaned one, conducting the same simulation with zero clearance results in a very minor increase in performance of less than one percentage point. While this

[5]Normalised with respect to the minimum and maximum static entropy encountered within the turbine domains.

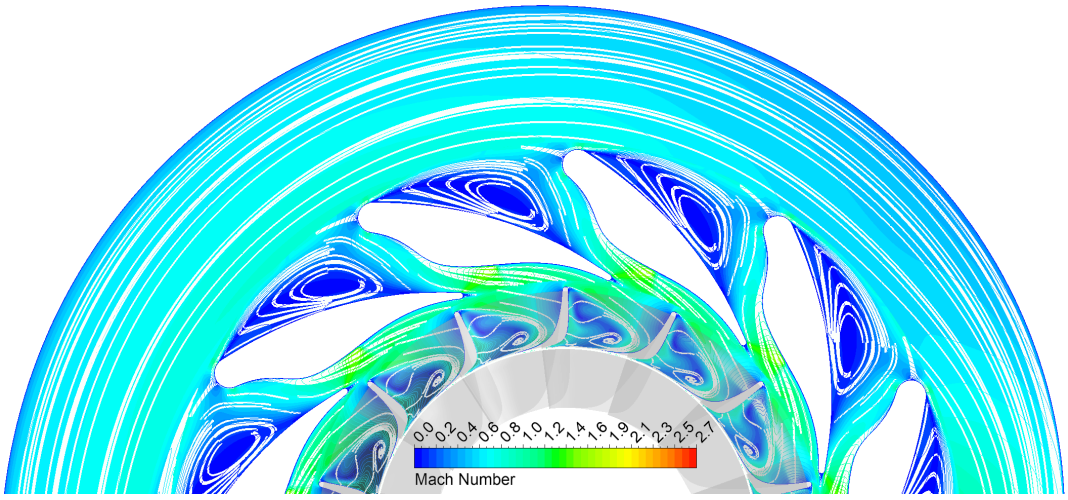

Figure 5.14: Mach number contours of the vaned radial inflow turbine, along the mid-span blade-to-blade surface.

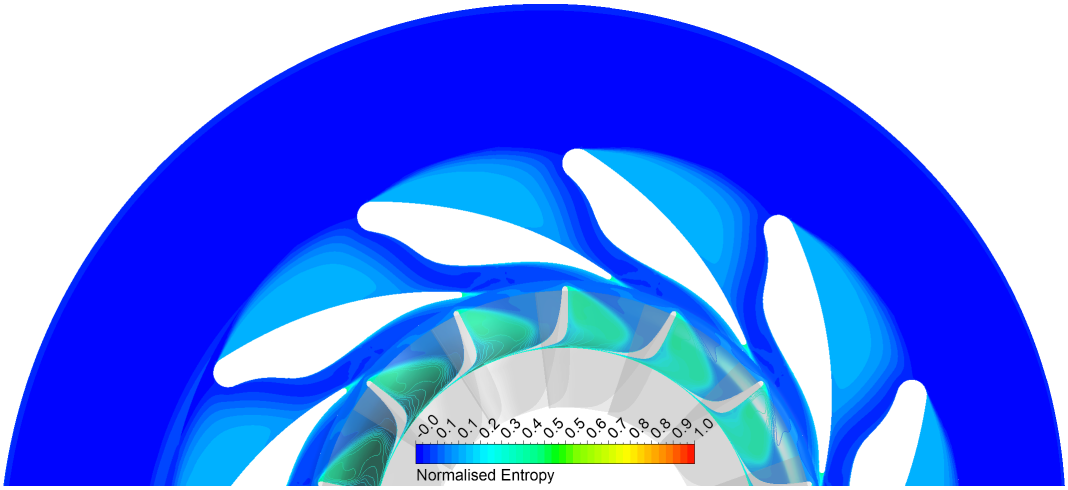

Figure 5.15: Normalised entropy contours of the vaned radial inflow turbine, along the mid-span blade-to-blade surface.

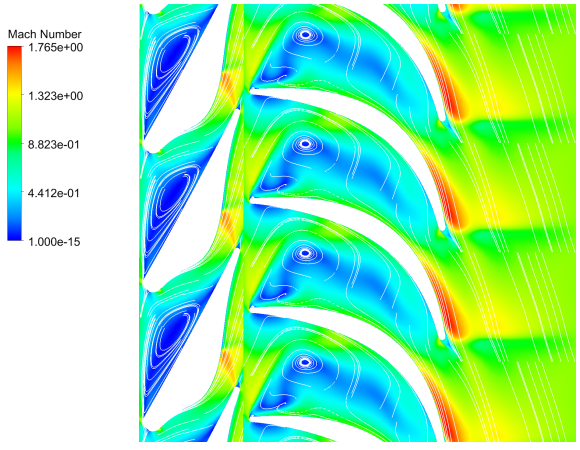

Figure 5.16: Blade to blade view of the Mach number contours of the vaned radial inflow turbine.

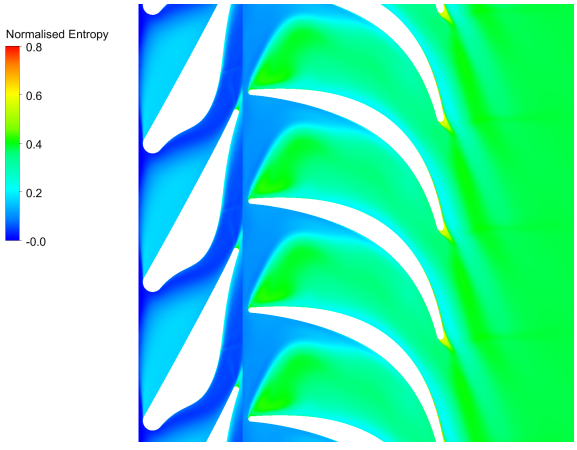

Figure 5.17: Blade to blade view of the normalised entropy contours of the vaned radial inflow turbine.

comparison was not made for this turbine[6], the outcome is expected to be similar.

As shown in Figure 5.18, the turbine features a strong outlet swirl downstream of the rotor, in the opposite direction of the rotor rotation. At the inlet of the duct domain, around 10 mm downstream of the rotor trailing edge, the flow angle is approximately 43 relative to the axial direction, with a swirl coefficient N_θ of 0.69. This swirl coefficient is calculated using Equation 5.3, with C_θ the circumferential flow velocity and C the absolute flow velocity. This swirl can also be seen in the blade to blade Mach contours in Figure 5.16. This swirl represents a major loss source, as this kinetic energy is not converted to useful work and cannot be recovered by a diffuser. This high tangential velocity can be attributed to the relatively steep outlet metal angle of 78°, as well as the low circumferential speed of the rotor trailing edge, which is a result of the small diameter and low shaft speed. Additionally, as seen in Figure 5.16, the flow is choked in the rotor throat. The recirculation zones in the flow passage further reduce the effective throat area of the rotor, leading to supersonic flow on the suction side of the blades near the leading edge. Combined with the steep outlet metal angle, this results in a very high tangential velocity, increasing the swirl.

$$N_\theta = C_\theta / C \tag{5.3}$$

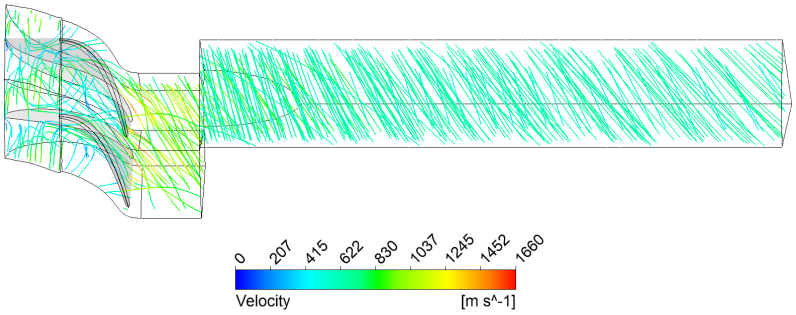

Figure 5.18: Velocity streamlines in the rotor and outlet duct of the vaneless turbine. The streamlines are plotted in the local reference frame, i.e. rotating for the rotor and stationary for the duct.

An overview of the contributions to the normalised entropy within each turbine section is shown in Figure 5.19. Here, the entropy is normalised with respect to the static entropy at the inlet of the volute and outlet of the duct, opposed to the minimum and maximum values encountered within the domains. As expected, the largest contributors are the stator and rotor. Notably, the contribution of the duct is larger than expected, at 14.6%. The likely cause for this is flow separation along the hemispherical turbine exit hub cap. This is visualised in Figure 5.20. It is recommended to change the hub cap geometry to optimise flow attachment and reduce these losses.

5.3.2. Vaneless Radial Inflow Turbine Results

The results of the CFD simulations of the vaneless RIT are summarised and compared to AxStream's results in Table 5.8.

[6]This is because the vaneless turbine has a shroud diameter ratio of close to 1, with a very sharp leading edge to blade tip transition. When removing the clearance, Ansys TurboGrid is unable to compute the blade geometry. This is not the case for the vaneless turbine.

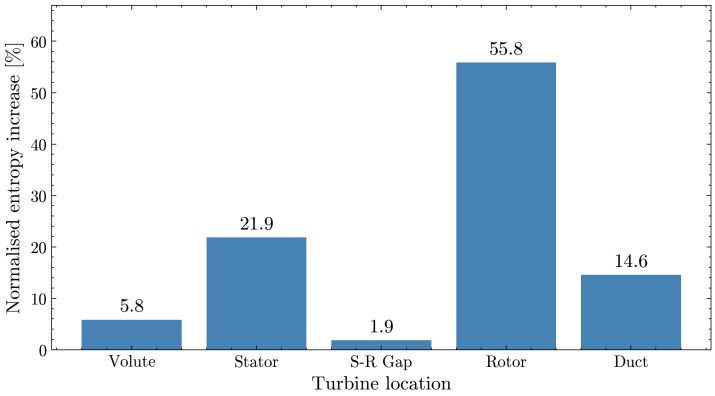

Figure 5.19: Histogram showing the contributions of each turbine section to the normalised static entropy increase in the vaned radial inflow turbine.

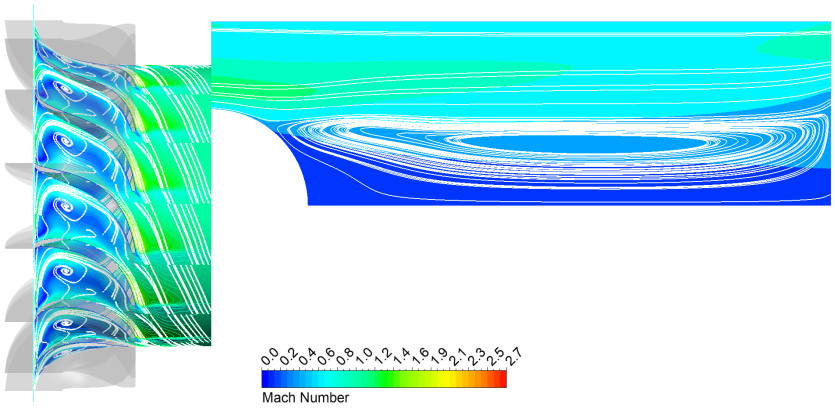

Figure 5.20: Mach number contours and streamlines along the mid-span blade-to-blade surface of the stator and rotor, and symmetry plane of the outlet duct, showing the flow separation at the rotor exit hub cap.

Table 5.8: Comparison of the performance parameters of the vaneless radial inflow turbine, found through CFD simulations and AxStream. N/A represents parameters not available in AxStream.

Property	**CFD**	**AxStream**
Outlet total temperature $T_{t,out}$ [K]	1065.23	1066.02
Outlet static temperature T_{out} [K]	1040.09	N/A
Mass flow rate $\dot{m}_{turbine}$[g/s]	72.45	52.19
Thermodynamic Power P_{therm} [kW]	31.115	25.193
Mechanical Power P_{mech} [kW]	26.712	25.193
Specific fuel consumption SFC (therm.) [g/(kW s)]	2.328	2.071
Total-static efficiency η_{ts} [%]	37.26	41.46
Rotor tip leakage $\dot{m}_{leak}$ [g/s]	16.16	0

The produced mechanical power is around 6% higher than predicted, and meets the imposed power requirement. Interestingly, the thermodynamic power is significantly higher than expected, by 23.5%, while the total outlet temperature closely matches the prediction. Nonetheless, this is achieved with an increased mass flow of 72.45 g/s, resulting in a higher specific fuel consumption of 2.328 g/s, a 12.4% increase. Like the vaned turbine, the total-to-static efficiency is lower than predicted by AxStream, but

less significantly, with a 4.2 percentage point decrease to 37.26%. This mass flow results in a rocket apogee of 55.6 km, around 3.3 km or 6.3% higher than the highest turbopump-fed apogee found in Section 5.1.

The streamlines, Mach number contours and normalised entropy contours are once again plotted to analyse the flow behaviour inside the turbine, see Figure 5.21-5.24, where very high flow velocities are again observed in the volute. As seen in Figure 5.21, the flow reaches M = 1 at the volute cut-water and accelerates as it expands into the scroll and rotor volume, indicating that the volute functions as a converging-diverging nozzle. This again leads to an extremely high tangential velocity component and a shallow volute outlet flow angle $\beta_1 = 81.5°$. With the higher tip speed, this results in a relative rotor inlet angle of 67.6°, similar to the one in the vaned turbine (69.6°). This again leads in a large recirculation zone on the suction side of the rotor, causing a large increase in entropy.

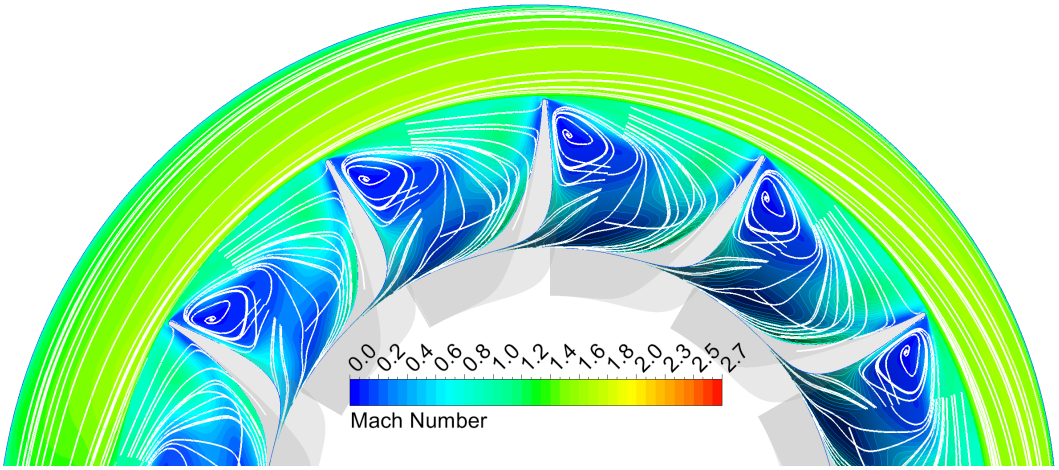

Figure 5.21: Mach number contours of the vaneless radial inflow turbine, along the mid-span blade-to-blade surface.

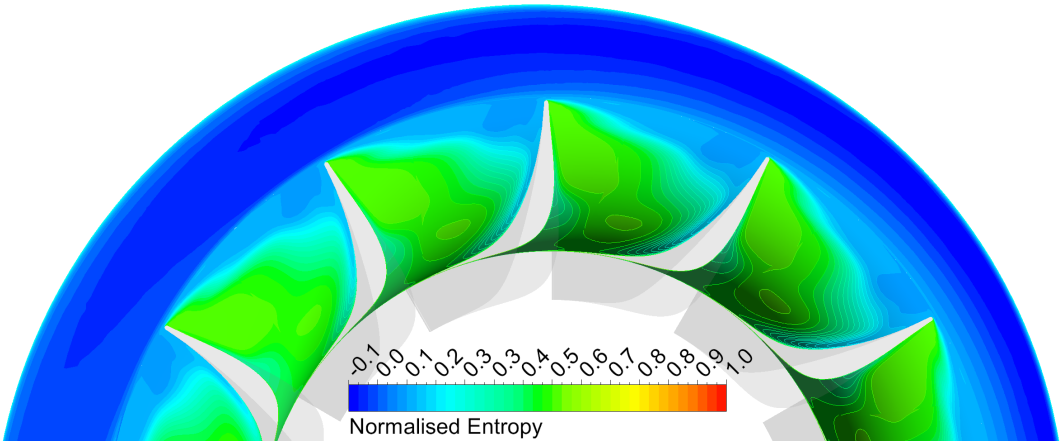

Figure 5.22: Normalised entropy contours of the vaneless radial inflow turbine, along the mid-span blade-to-blade surface.

Similarly to the vaned RIT, the vaneless RIT exhibits strong exit swirl and high outlet Mach numbers, as the recirculation bubbles once again reduce the effective area of the flow passage. In this case, however, the flow is not quite choked in the rotor, reaching an outlet Mach number of around 0.7. Compared to the vaned turbine, the axial velocity at the rotor exit is lower, at around 195 m/s compared to 510 m/s. The resultant outlet flow angle is 24.3°with respect to the axial direction, and $N_\theta = 0.89$.

Another possible contributing factor to the lower efficiency could be the leakage from the pressure side to the suction side of the rotor, through the 0.3 mm blade tip to shroud clearance. While AxStream did not predict any leakage, the CFD simulations show a 16.16 g/s blade tip leakage; 22.30% of the total mass flow. However, the same simulation with zero clearance predicts similar performance, with an unchanged total mass flow and only a 0.9 percentage point increase in total-to-static efficiency and 1.4% increase in thermodynamic power. A possible explanation for this marginal difference is as follows. Typically, when tip leakage flow occurs across turbine blade tips, the flow forms turbulent streams that mix with the passage flow [80]. In a typical turbine with well-attached main flow, the tip leakage reduces efficiency as it bypasses the rotor blades and dissipates energy in vortices instead of contributing to work. In the turbine considered here, however, the flow passage is already dominated by strong recirculation regions, swallowing a portion of the leakage flow, which then mixes with the main flow. This masks the adverse effects that would otherwise be observed in a typical turbine.

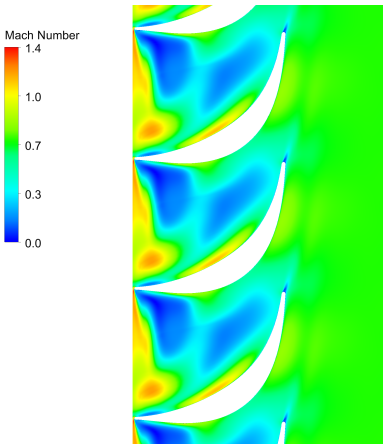

Figure 5.23: Blade to blade view of the Mach number contours of the vaneless radial inflow turbine.

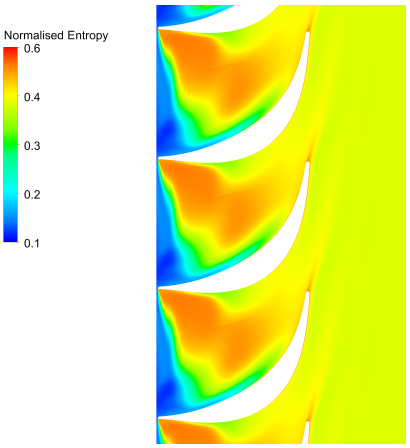

Figure 5.24: Blade to blade view of the normalised entropy contours of the vaneless radial inflow turbine.

An overview of the contributions to the normalised entropy within each turbine section is shown in Figure 5.25. The largest contributor is again the rotor, followed by the volute. The relative entropy increase in the duct is lower than for the vaned turbine, as the axial flow velocity at the rotor outlet is lower, allowing for better flow attachment to the hub cap. Nonetheless, it is recommended to redesign the hub cap to accommodate the flow better.

5.4. CFD Results at Off-design Conditions

Following the CFD simulations at the nominal design point, the turbines were also simulated under various off-design operating conditions. This includes a near-vacuum outlet pressure boundary condition to represent operation at high altitude and an increased shaft speed of 140 krpm to assess the effect of lower duty coefficients. This twofold increase of shaft speed reduces the flow coefficient by a factor of two and the work coefficient by a factor of 4. The off-design results of the vaned turbine are presented in Subsection 5.4.1, followed by those of the vaneless turbine in Subsection 5.4.2.

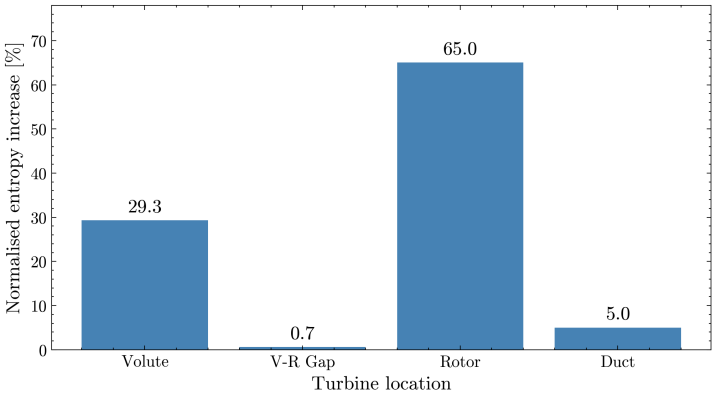

Figure 5.25: Histogram showing the contributions of each turbine section to the normalised static entropy increase in the vaneless radial inflow turbine.

5.4.1. Vaned Turbine

The results of the CFD simulations of the vaned RIT with the reduced outlet pressure and increased shaft speed are summarised and compared to the nominal case in Table 5.9. An overview of the entropy increase in each section for each case is shown in Figure 5.26.

Table 5.9: Comparison of the performance parameters of the vaned radial inflow turbine at sea-level conditions, near-vacuum outlet conditions and 140 krpm.

Property	**Nominal**	**Near-Vacuum**	**140 krpm**
Outlet total temperature $T_{t,out}$ [K]	1151.06	1145.75	1062.99
Outlet static temperature T_{out} [K]	1047.94	690.87	986.703
Mass flow rate $\dot{m}_{turbine}$[g/s]	103.56	103.49	103.62
Thermodynamic Power P_{therm} [kW]	24.341	25.580	45.025
Mechanical Power P_{mech} [kW]	24.584	25.950	45.321
Specific fuel consumption SFC (therm.) [g/(kW s)]	4.212	4.046	2.301
Total-static efficiency η_{ts} [%]	21.60	26.40	39.98
Rotor tip leakage $\dot{m}_{leak}$ [g/s]	14.98	14.90	13.31

The turbine with near-vacuum outlet static pressure has increased performance compared to the sea-level case, with a 4.8 percentage point increase in total-to-static efficiency, despite having the same mass flow, as the flow is still choked by the stator and therefore dependent on the upstream pressure. The thermodynamic and mechanical power are also slightly higher, by around 4-5%. Looking at the Mach number contours in Figure 5.27, one can see that the choking effect in the rotor has become more pronounced downstream of the rotor, as the flow expands to a much lower pressure. As a result, the flow reaches Mach numbers of up to 3, leading to high losses, as is apparent when looking at the normalised entropy contour at the trailing edge of the blades in Figure 5.28. The effect of this is also seen in the outlet static temperature, which is over 350 K lower than the nominal case. The flow is more axial compared to the turbine operating at nominal conditions, resulting in lower whirl and therefore lower losses in the duct.

The flow inside the stator and rotor passage, however, is very similar to the nominal case, again exhibiting strong recirculation zones.

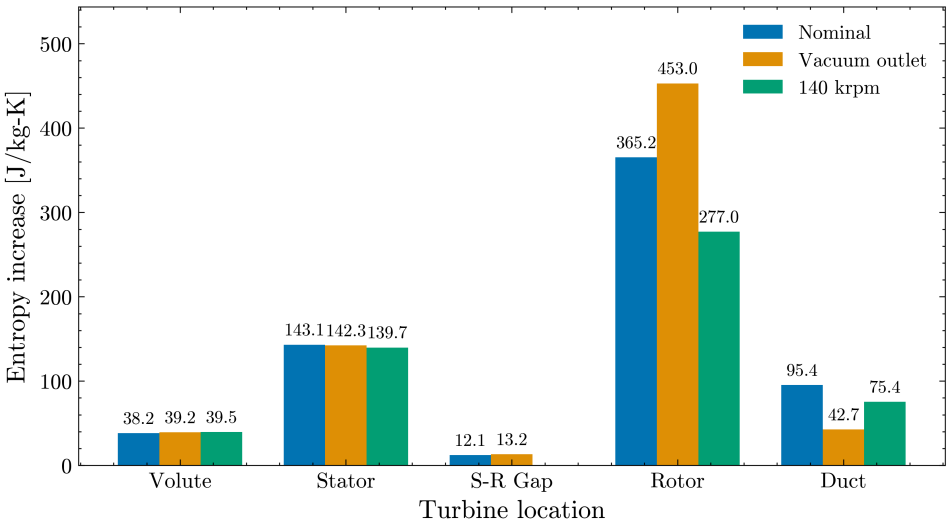

Figure 5.26: Histogram showing the contributions of each turbine section to the static entropy increase in the vaned radial inflow turbine.

As expected, the turbine rotating at 140 krpm has significantly higher performance, with an 18.4 percentage point increase in total-to-static efficiency, and an 85% increase in thermodynamic and mechanical power. With the same mass flow rate as before, this results in a 55% reduction in specific fuel consumption. The turbine also has a lower leakage rate of 13.31 g/s compared to 14.98 g/s. This increased performance confirms that the turbine design benefits from a higher shaft speed (and likely an increased diameter), pushing the design towards more typical duty coefficients and U/C_0.

Nonetheless, the streamlines and Mach number contours in Figure 5.29 still show similar behaviour as before, with large recirculation zones inside the rotor, and better but still non-ideal flow angles. More so, the supersonic region near the trailing edge of the blades is more pronounced, causing high losses. This is also seen in the normalised entropy contours in Figure 5.30, where the main rotor passage now has a lower relative contribution to the normalised entropy, but the flow separation at the trailing edge has a significant contribution.

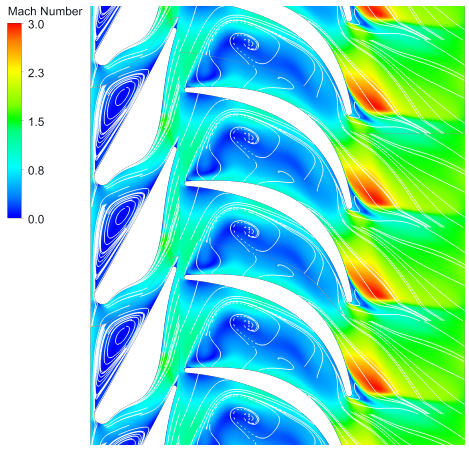

Figure 5.27: Blade to blade view of the Mach number contours of the vaned radial inflow turbine at near-vacuum outlet conditions.

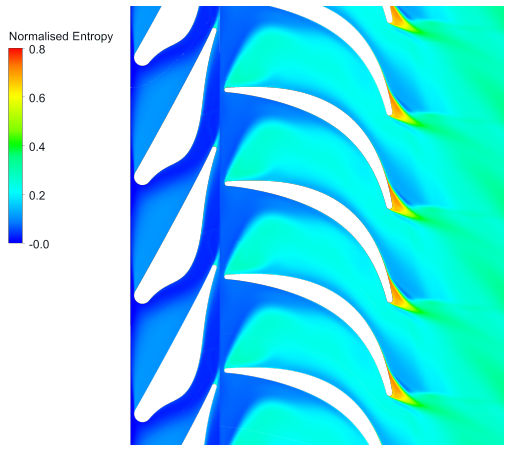

Figure 5.28: Blade to blade view of the normalised entropy contours of the vaned radial inflow turbine at near-vacuum outlet conditions.

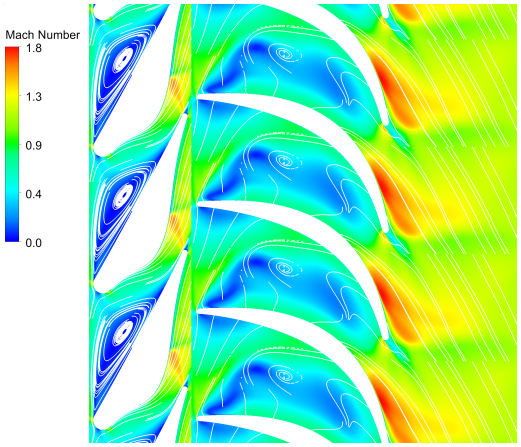

Figure 5.29: Blade to blade view of the Mach number contours of the vaned radial inflow turbine at 140 krpm.

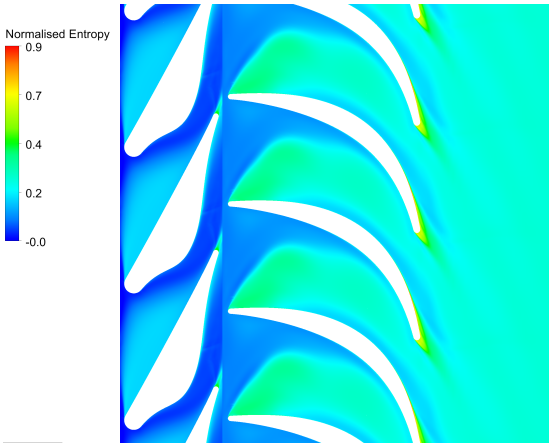

Figure 5.30: Blade to blade view of the normalised entropy contours of the vaned radial inflow turbine at 140 krpm.

5.4.2. Vaneless Turbine

The results of the CFD simulations of the vaneless RIT with no outlet nozzle and with the reduced outlet pressure and increased shaft speed are summarised and compared to the nominal case in Table 5.9. The turbine has also been simulated with a choked nozzle at the outlet, but needs more adjustment to obtain usable results. Due to time constraints, these adjustments have not been performed, and as such these results are not included in this work.

An overview of the entropy increase in each section for each case is shown in Figure 5.31.

Table 5.10: Comparison of the performance parameters of the vaneless radial inflow turbine at sea-level conditions, near-vacuum outlet conditions and 140 krpm.

Property	Nominal	Near-vacuum	140 krpm
Outlet total temperature $T_{t,out}$ [K]	1065.23	1037.86	936.382
Outlet static temperature T_{out} [K]	1040.09	666.934	927.263
Mass flow rate $\dot{m}_{turbine}$[g/s]	72.45	72.49	72.45
Thermodynamic Power P_{therm} [kW]	31.115	35.580	51.828
Mechanical Power P_{mech} [kW]	26.712	31.057	48.530
Specific fuel consumption SFC (therm.) [g/(kW s)]	2.328	2.037	1.398
Total-static efficiency η_{ts} [%]	37.26	25.06	62.37
Rotor tip leakage $\dot{m}_{leak}$ [g/s]	16.16	15.65	16.64

As opposed to the vaned turbine, the vaneless turbine with near-vacuum outlet static pressure has decreased performance compared to the sea-level case, with a 12.2 percentage point lower total-to-static efficiency. Despite this, the thermodynamic and mechanical power are significantly higher, by 14.3% and 16.3% respectively, and the total outlet temperature is around 28 K lower.

A likely explanation for this decrease in efficiency and increase in power is as follows. As the flow is only choked in the volute, the lower back-pressure results in higher flow acceleration in the volute. This results in an even more shallow relative flow angle, making the recirculation bubble more pronounced, as seen in Figure 5.32 and Figure 5.33. Additionally, the lower back-pressure raises the pressure ratio

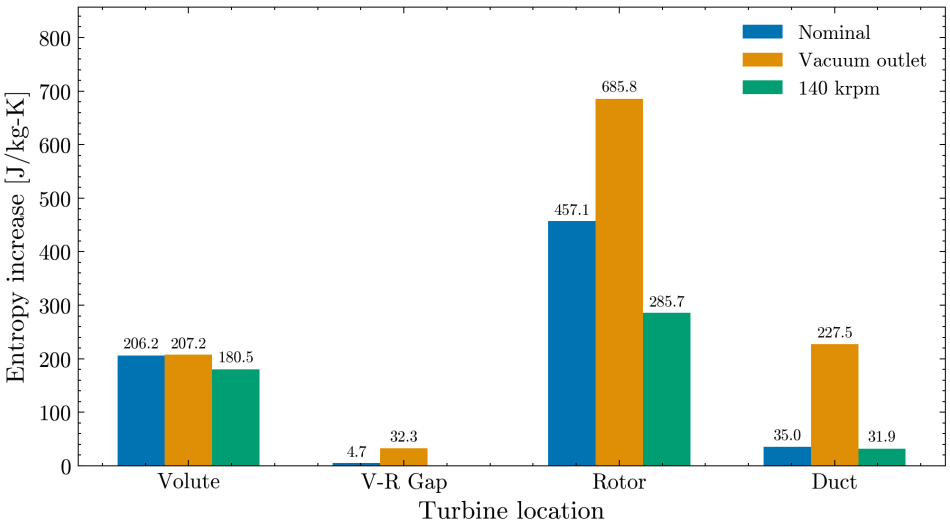

Figure 5.31: Histogram showing the contributions of each turbine section to the static entropy increase in the vaneless radial inflow turbine.

between the rotor passage and the duct above the critical pressure ratio, causing choked flow in the rotor throat with a maximum Mach number of 3, which was not the case with the 2 bar outlet pressure. This causes significant flow separation at the trailing edge, which also becomes apparent when looking at the relative entropy increase downstream of the rotor.

At 140 krpm, the turbine does perform as expected, again almost doubling the performance. The total-to-static efficiency is increased by 25.1 percentage points to 63.4% and the thermodynamic and mechanical power are increased by 66.6% and 81.7%, respectively, resulting in a SFC of only 1.4 g/(kW s). The leakage rate is only slightly higher, by about 0.5 g/s. This increased performance once again confirms that also the vaneless turbine design benefits from an increased shaft speed (and likely an increased diameter), pushing the design towards more typical duty coefficients and U/C_0.

The rotor still shows significant recirculating flow and requires more optimisation. However, as opposed to two distinct recirculation bubbles, the rotor now has one large bubble.

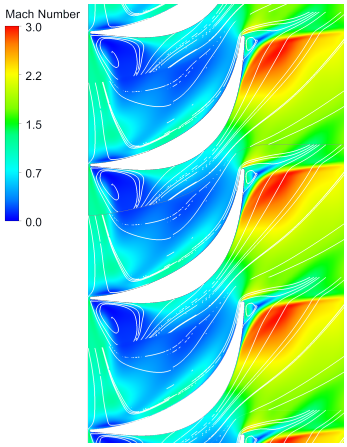

Figure 5.32: Blade to blade view of the Mach number contours of the vaneless radial inflow turbine at near-vacuum outlet conditions.

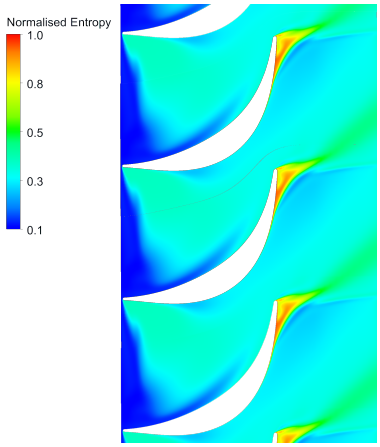

Figure 5.33: Blade to blade view of the normalised entropy contours of the vaneless radial inflow turbine at near-vacuum outlet conditions.

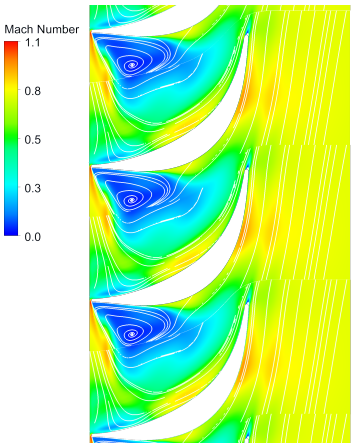

Figure 5.34: Blade to blade view of the Mach number contours of the vaneless radial inflow turbine at 140 krpm.

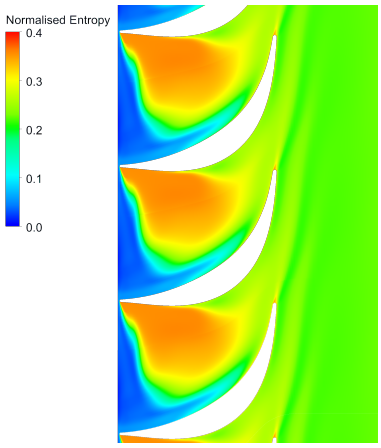

Figure 5.35: Blade to blade view of the normalised entropy contours of the vaneless radial inflow turbine at 140 krpm.

6

Conclusion

The research objective of this thesis was "to investigate whether a radial inflow turbine can be a suitable solution for a small-scale open-cycle rocket engine and whether it can provide a performance advantage compared to a typical axial turbine". A hypothetical scenario was made, with a next generation DARE Stratos VI rocket aiming to reach the highest altitude possible, with the same Firebolt engine and a similar overall architecture as Stratos V. The research question that followed from that is:

> ***Are radial inflow turbines a viable solution for powering the Firebolt engine in the DARE Stratos VI rocket?***

To answer this question, the sub-questions below will be treated first in Section 6.1, followed by the main research question in Section 6.2.

6.1. Sub-Research Questions

1. What turbine performance is required to outperform electric pump-fed systems in terms of apogee for Stratos VI?

A tool was developed to size the main parameters of the Stratos VI rocket for varying burntimes and rocket diameters and to simulate the trajectory of the rockets, enabling a comparison between the pressure-fed, electric pump-fed and turbopump-fed architectures. Simplified relationships were made to obtain preliminary estimates of the turbine performance with respect to the rocket parameters.

As expected, both pump-fed rocket architectures showed significant performance gains over the pressure-fed architecture due to mass savings from a simplified pressurisation system, a smaller pressurant tank and lighter propellant tanks. Additionally, the smaller pressurant tank allows for larger propellant tanks, while keeping the diameter small and staying within the imposed rocket length constraints. Unexpectedly, the electric pump-fed rockets showed similar performance to the turbopump-fed rockets, as their battery mass is not as prohibitive as initially assumed within DARE.

It was established that, in this context, the most important metric for turbine performance is the mass flow $\dot{m}$, as it has a direct influence on the rocket engine specific impulse I_{sp} and thereby the rocket apogee. In order to attain a higher altitude than the pump-fed rocket configuration, 48.7 km, a turbine mass flow of less than 222 g/s is required, with a total burntime of at least 35.5 s.

2. Can radial inflow turbines meet the performance requirements under the geometric and operational constraints of Stratos VI?

The constraints of the rocket proved to be a severe limitation on the turbine design, restricting the rotor diameter and therefore the achievable tip speed. This, combined with the high pressure ratio required for a power dense design, led to unusually high duty coefficients and low U/C_0, pushing the turbines far outside the recommended design space, with low efficiency as a result. To improve feasibility, the shaft speed was increased from 40 krpm to 70 krpm, which increased the rotor tip speed and lowered the duty coefficients, which still remained outside of conventional ranges.

Despite these challenges, two radial turbine designs were made, which both meet the shaft power requirement of 24.4 kW, with mass flows of below 222 g/s. A vaned turbine and a vaneless turbine were designed, which, at their nominal operating point, with a respective mass flow of 103.6 g/s and 72.5 g/s and a total-to-static efficiency of 21.6% and 37.3%, as found through CFD simulations. The vaneless turbine even delivered power than required, with a thermodynamic power estimate of 31.1 kW and a mechanical power estimate of 26.7 kW[1].

These results confirm that radial inflow turbines can meet the performance requirements for the hypothetical Stratos VI rocket, under the imposed constraints. This was, however, achieved with very low total-to-static efficiencies, indicating that the turbines can benefit from further optimisation.

3. How do vaned and vaneless radial inflow turbines compare in terms of performance and aerodynamic flow behaviour?

The vaneless RIT outperforms the vaned turbine at nominal conditions. Without a stator, the vaneless turbine allows for larger rotor diameters within the constraints of the rocket, leading to more reasonable stage parameters, yielding a 30% lower mass flow, 28% higher thermodynamic power output and 55% lower specific fuel consumption at a comparable pressure ratio. This indicates that, in the context of the Stratos VI constraints, the vaneless turbine is the more suitable of the two options.

However, CFD simulations showed that both turbines perform much more poorly than what was predicted by AxStream's loss models. Both suffer from tip leakage, outlet swirl and substantial flow separation within both the rotor and stator passages resulting from poorly matched flow angles, limiting their efficiency.

For the vaned turbine, this flow angle mismatch was observed in two locations. The volute significantly accelerates the flow, reaching a mass-flow averaged Mach number of 0.76 with a highly tangential velocity component at the volute-stator interface, resulting in flow separation and high losses in the stator. Further downstream, the stator introduces similar problems. The stator geometry generated by AxStream provides inadequate guidance to the flow, producing a very tangential flow at the stator-rotor interface, which combined with the low rotor tip speed, again causes mismatched flow angles and flow separation at the rotor inlet.

While the stator severely limited the performance of the current design, it also means the vaned turbine has significant potential for improvement. A redesigned volute and more conventional converging-

[1]The thermodynamic power is calculated using the mass flow and enthalpy at the inlet and outlet of the turbine, whereas the mechanical power is calculated using the torque and rotational velocity of the turbine.

diverging stator should provide more control over the expansion and flow angles, reducing flow separation and improving efficiency. The rotor inlet metal angle can also be adjusted, provided that the structural stresses in the blades remain at an acceptable level.

The vaneless turbine, on the other hand, avoids these losses in the stator, but exhibits the same behaviour in the rotor. As the flow is choked at the inlet of the volute scroll, it produces a highly tangential supersonic flow at the volute-rotor interface, which is unguided due to a lack of stator/guide vanes. This makes the flow behaviour difficult to control, especially at off-design conditions, even with careful adjustment of the volute geometry. As a result, the vaneless turbine is more challenging to optimise, while the vaned design provides a better means to adjust the flow angles and prevent losses.

4. How do radial inflow turbines compare to single-stage axial turbines in the context of small-scale open-cycle rocket engines?

For this specific design case, the preliminary axial turbine design performs similarly to the vaneless radial inflow turbine. AxStream predicted a similar mass flow of 50.5 g/s compared to the vaneless RIT's 52.2 g/s, but with a roughly 10 percentage point higher total-to-static efficiency. This improvement is a result of the axial placement of the volute, which allows for a larger rotor with higher tip speeds and therefore more typical duty coefficients.

As with the RITs, the axial design is constrained by manufacturability, limiting the number of rotor blades to keep the throat width above the imposed minimum.

It must be noted that the performance of the axial turbine was not validated against CFD simulations and, given the significant discrepancies observed between AxStream's predictions and the CFD simulations for the radial turbines, it is possible the actual performance of the axial turbine may deviate as well. Particularly, the partial admission losses may be more pronounced than what is estimated by AxStream. On the other hand, given the relatively low predicted efficiency of the axial turbine, there is likely to be significant potential for further improvement, just like the radial turbines. Moreover, the axial turbine was designed for the same design point as the RITs, i.e. 70 krpm and 24.4 kW, whereas a more optimal design point may exist for this turbine. Furthermore, it is important to emphasise that these findings are only valid for this specific design case of the hypothetical Stratos VI rocket, which is greatly driven by unique constraints such as the small diameter. Therefore, no conclusions can be confidently drawn about the comparison of axial and radial turbines for small-scale open-cycle rocket engines in general.

Nevertheless, axial turbines do offer some clear advantages over radial turbines. Given their extensive historical use in rocket engines, their design and behaviour is well understood. Additionally, they may be cheaper and easier to manufacture. Lastly, they allow for easier staging compared to radial inflow turbines to increase power extraction.

5. How sensitive is the performance of radial inflow turbines to the changing atmospheric conditions during a rocket launch?

The off-design CFD simulations showed that the turbine performance is indeed sensitive to varying outlet conditions. Without a choked outlet nozzle, both turbines experienced much stronger expansion at the rotor outlet at near-vacuum conditions, leading to outlet Mach numbers of up to 3.0.

In the vaned turbine, the flow is already choked at both the stator and the rotor trailing edge at sea-level conditions. As a result, the flow behaviour inside the rotor does not change significantly at near-vacuum conditions. Directly downstream of the rotor, however, the increased flow expansion and high Mach numbers lead to increased losses within the outlet duct. Nonetheless, the turbine reaches a lower total outlet temperature, allowing it to deliver a 5% higher power output with a 4.8 percentage point increase in total-to-static efficiency compared to sea-level conditions. As the turbine maintains the same mass flow, this results in a lower specific fuel consumption.

The vaneless turbine, on the other hand, proved to be less robust if no choked outlet nozzle is used, as the flow inside the rotor is still mostly subsonic, despite the increased flow velocity in the volute. Lowering the back-pressure therefore further expands the flow within the rotor (increasing the pressure ratio), until it starts choking at the rotor exit, again leading to Mach numbers of up to 3.0 and high losses in the duct. As a result, the vaneless turbine reaches a roughly 15% higher power output and therefore a lower specific fuel consumption, but with a 12 percentage point decrease in total-to-static efficiency.

This sensitivity to varying outlet conditions can be mitigated by replacing the outlet duct with a choked nozzle, as originally intended. However, preliminary CFD simulations showed that further adjustment of the throat size is needed to achieve the correct pressure ratio, and more simulations are needed across varying outlet conditions to confirm its effectiveness.

6.2. Main Research Question

Are radial inflow turbines a viable solution for powering the Firebolt engine in the DARE Stratos VI rocket?

The results of the work conducted in this thesis demonstrate that the use of radial turbines is feasible within the imposed constraints of this application. Both the vaned and vaneless turbine met the imposed shaft power requirement of 24.4 kW, with the latter requiring a mass flow of 72.5 g/s. This is roughly a third of the maximum allowable mass flow required to outperform the electric pump-fed rocket configuration, achieving a 6.3% (3.3 km) higher altitude.

However, due to the restrictive geometry of the rocket, in particular its diameter which restricts the maximum diameter of the turbine, the rocket is not able to use the radial inflow turbines at their full potential. As a result of this, the turbine efficiencies remained low, requiring further optimisation to minimise the mass flow and improve the overall performance of the rocket.

That being said, while radial turbines are certainly usable in this application, axial turbines may still be a more suitable solution at this scale, taking into account their design flexibility, ease of manufacturing and the potential for multi-stage high pressure ratio configurations. Additionally, their extensive and well-documented heritage in space applications makes them a more suitable option in a student team context.

In conclusion, the answer to the research question is that, yes, radial inflow turbines are a viable solution for powering the Firebolt engine in the DARE Stratos VI rocket. However, they should not be regarded as the only or necessarily the optimal solution, but rather as one of several feasible turbomachinery options for this class of rocket.

7

Recommendations

Based on the work conducted in this thesis, a number of recommendations can be made for further research. In Section 7.1, system-level recommendations are made pertaining to the overall use of turbines for this rocket and how to obtain a more performant rocket design. In Section 7.2, general recommendations are made for the turbopump assembly, such as the choice of turbine and the design process. In Section 7.3, recommendations are made for further work on the radial inflow turbines. Lastly, in Section 7.4, several recommendations are made for the CFD analysis of the turbines.

7.1. System-Level Recommendations

Considering the comparable predicted performance of the turbopump-fed rockets and electric pump-fed rockets, it may be more practical in the near term to focus on the development of the latter configuration. This would allow DARE to focus on gaining more experience with propellant pump design, mechanical design and rotordynamics. If, at a later stage, the rocket and/or engine is upscaled, switching to the turbopump-fed architecture may become more attractive. Nevertheless, the development of turbines within DARE remains worthwhile, but it may be more beneficial to iterate on several prototypes first, without the strict rocket constraints, in order to to build experience without being overly limited.

The system-level trade studies in this thesis were largely based on the current Stratos V architecture and the Firebolt DLX150C engine. For future development, however, more flexibility in the engine design point should be considered. It is recommended to repeat the trade studies or optimisations with varying thrust levels and chamber pressures (and therefore required pump outlet pressure), as these have a significant impact on the required pump power and rocket performance. The optimal rocket design is highly constrained by drag and the minimum tower exit velocity requirement (TEV), which can be mitigated with a higher thrust level, though at the cost of increased turbine power demand.

Finally, as the design of the rocket matures, more detailed analysis will be needed at the system level. In particular, it is recommended to analyse the pitch–roll coupling dynamics to investigate whether the slenderness ratio of the rocket can be increased to further improve overall performance of the rocket.

7.2. General Turbopump Recommendations

Several recommendations are made in Section 7.3 on how to further improve the radial inflow turbine designs. This section, however, focuses on the general turbopump architecture and design process.

While AxStream is a powerful tool that is useful for exploring design spaces of turbomachines and assessing the influence of certain design parameters, it is also a black-box tool. For future work, it would be more valuable to complement or replace the use of AxStream with more flexible (in-house developed) reduced-order design software, such as the TurboSim model developed by the TU Delft Aerospace Engineering faculty's Propulsion & Power department. This allows for more flexibility and can be further extended with features or loss models, e.g. for partial admission, and gives more control over the turbine design process.

Additionally, a more structured iterative design workflow should be developed, which includes a parametric blade modeller, directly linked to TurboSim and Ansys CFX (or other CFD solvers), to efficiently iterate on turbine designs with minimal manual work.

Both turbine configurations studied in this thesis require further optimisation and CFD validation before a final decision can be made on which one is more performant for this design case. Nonetheless, axial turbines may still be a more suitable solution at a student team level, due to their design flexibility, ease of manufacturing and extensive and well-documented heritage in launchers. The possibility of staging should be investigated to operate at high pressure ratios and increase power density, while maintaining favourable design points at each turbine stage. Partial admission effects should also be further studied through loss models and CFD.

If the radial turbine configuration is pursued instead, a vaned turbine is recommended, as a well-designed stator provides better control over the supersonic expansion upstream of the rotor and the flow angles at the stator-rotor interface. Partial admission could also be investigated for radial turbines, as it would allow for more flexibility in the stator design, e.g. with larger throats. However, it may introduce unsteady blade loading and rotordynamic instabilities.

For all turbine configurations, more analysis is required on the choked outlet nozzle's impact across varying ambient pressures. It is recommended to evaluate whether the nozzle is truly necessary, or if the engine can tolerate the varying turbine performance throughout the flight. Nonetheless, the nozzle may recover some wasted energy from the turbine exhaust in the form of additional thrust.

Another area for future work is shaft speed, as it has had a major influence on the turbine design. While increasing the turbine shaft speed may further reduce the required mass flow through the turbine, its influence on the overall turbopump system should not be neglected. More analysis is needed on whether the pumps can operate at such high shaft speeds, without encountering issues such as cavitation, rotordynamic instabilities, unavailability of high-speed and high-thrust bearings, or unacceptably low blade heights. Moreover, the reliability of the mechanical seals should be evaluated, as they may suffer from leakage or excessive wear under these conditions. Alternatively, geared pumps can also be considered. While mechanically and rotordynamically more complex and risky, they would decouple turbine and pump speeds, allowing both to run at their optimal design point.

It is also recommended to reconsider the manufacturing aspect of the turbines. Inconel 713C was selected for its excellent structural properties at high temperatures, but it is difficult and expensive

to machine. Alternative materials may be considered, while keeping in mind their influence on the turbine design. If cost is not a limiting factor, more advanced techniques such as EDM (electric discharge machining) could be considered to reduce the stator throat width and trailing edge radius.

Finally, it is recommended to consider the structural aspect of the turbines early on in the design. This includes evaluating the centrifugal and aerodynamic blade loads, as well as thermal stresses and expansion, and high-cycle fatigue. For example, the rotor blades of the radial turbine may be made thinner to decrease the solidity and reduce weight.

7.3. Radial Turbine Design Recommendations

For future work on the radial turbine, the main priority is to redesign the stator. It is recommended to use a more conventional converging-diverging nozzle design, which provides better control over the outlet Mach number and stator outlet flow angles, preventing flow separation and recirculation in the rotor passage. The rotor inlet metal angle may also be adjusted, provided that the structural stresses in the blades remain at an acceptable level. It is further recommended to resize the volute, provided enough space is available in the rocket, to reduce the flow velocity at the volute-stator interface and reduce flow separation at the stator inlet.

As significant tip leakage was observed in the radial turbines, it is recommended to reduce tip clearance if possible, while accounting for thermal expansion, tolerance stack-up and play in the turbopump assembly, as well as the machining capabilities available to the team, because tighter tolerances come with higher costs. A reduced tip clearance may also allow for smaller blade heights while maintaining the same clearance-to-blade-height ratio. This may allow for larger stator throats while preserving the same total throat area.

The hub cap geometry should also be revised. Instead of the current hemispherical cap, a less steep design may reduce losses caused by flow separation in the duct.

Finally, more optimisation is needed to minimize the turbine exit swirl. This includes adjusting the rotor outlet metal angles and throat size, and potentially implementing exit guide vanes [30].

7.4. CFD Recommendations

For future CFD work, it is recommended to model non-axisymmetric effects caused by the non-uniform flow in the volute and, by extension, the stator. While initial simulations can still be performed using frozen rotor and mixing plane interfaces, they should be supplemented with a full-annulus model to fully capture the unsteady effects and further optimise the turbine geometry. This is particularly important for the axial turbine, as the partial-admission stator design is inherently non-axisymmetric. Additionally, transient URANS simulations can be conducted to capture the unsteady flow phenomena, which are particularly important for the structural design of the turbines, as they directly influence the blade loading, high-cycle fatigue, and rotordynamic behaviour. Additionally, it may be worthwhile to consider higher-fidelity methods, such as LES or hybrid RANS–LES, to gain a more detailed understanding of the turbulence structures that RANS cannot resolve.

References

[1] *Delft Aerospace Rocket Engineering*. URL: https://dare.tudelft.nl (visited on 08/03/2024).

[2] Marcel Kwapień, Luca Elbracht, and Andrei Petrache. *Stratos V Tanks Detailed Design Report*. Tech. rep. Stratos V, Delft Aerospace Rocket Engineering, Aug. 2024.

[3] Safer Cylinders. *Our Products*. URL: https://www.safercylinders.com/products (visited on 07/09/2025).

[4] D.K. Huzel and D.H. Huang. *Modern Engineering for Design of Liquid-Propellant Rocket Engines*. Progress in Astronautics and Aeronautics. AIAA, 1992. ISBN: 1600864007, 9781600864001.

[5] Jan Struziński et al. *DTP-E74 Preliminary Design Report*. Tech. rep. Sparrow, Delft Aerospace Rocket Engineering, Sept. 2021.

[6] George Sutton. "Turbopumps, a Historical Perspective". In: *42nd AIAA/ASME/SAE/ASEE Joint Propulsion Conference & Exhibit*. July 2006. DOI: 10.2514/6.2006-5033. eprint: https://arc.aiaa.org/doi/pdf/10.2514/6.2006-5033. URL: https://arc.aiaa.org/doi/abs/10.2514/6.2006-5033.

[7] NASA. *SP-8107: Turbopump systems for liquid rocket engines*. Tech. rep. NASA, 1974.

[8] Loren Grush. *A 3D-Printed, Battery-Powered Rocket Engine*. Ed. by Popular Science. URL: https://www.popsci.com/rocket-labs-got-3d-printed-battery-powered-rocket-engine/ (visited on 08/05/2024).

[9] Juyeon Lee et al. "Performance Analysis and Mass Estimation of a Small-Sized Liquid Rocket Engine with Electric-Pump Cycle". In: *International Journal of Aeronautical and Space Sciences* 22.1 (Feb. 2021), pp. 94–107. ISSN: 2093-2480. DOI: 10.1007/s42405-020-00325-z. URL: https://doi.org/10.1007/s42405-020-00325-z.

[10] Rocket Lab. *Reusable Rockets*. URL: https://www.rocketlabusa.com/launch/reusable-rockets/ (visited on 08/03/2024).

[11] Byron Wood. "Propulsion for the 21st Century - RS-68". In: *38th AIAA/ASME/SAE/ASEE Joint Propulsion Conference & Exhibit*. DOI: 10.2514/6.2002-4324. eprint: https://arc.aiaa.org/doi/pdf/10.2514/6.2002-4324. URL: https://arc.aiaa.org/doi/abs/10.2514/6.2002-4324.

[12] Alessandro Battegazzore et al. *Turbomachinery Development Team Detailed Design Report*. Tech. rep. Stratos V, Delft Aerospace Rocket Engineering, Aug. 2023.

[13] Meherwan P. Boyce. "8 - Radial-Inflow Turbines". In: *Gas Turbine Engineering Handbook (Fourth Edition)*. Ed. by Meherwan P. Boyce. Fourth Edition. Oxford: Butterworth-Heinemann, 2012, pp. 357–383. ISBN: 978-0-12-383842-1. DOI: https://doi.org/10.1016/B978-0-12-383842-1.00008-1. URL: https://www.sciencedirect.com/science/article/pii/B9780123838421000081.

[14] *Shuttle Crew Operations Manual*. Available at https://web.archive.org/web/20230411024639/https://www.nasa.gov/centers/johnson/pdf/390651main_shuttle_crew_operations_manual.pdf. United Space Alliance. Dec. 2008.

[15] J.F. Gülich. *Centrifugal Pumps*. Springer Berlin Heidelberg, 2007. ISBN: 9783540736950. URL: https://books.google.nl/books?id=eurAVC3_Pk4C.

[16] O. E. Baljé. "A Study on Design Criteria and Matching of Turbomachines: Part A—Similarity Relations and Design Criteria of Turbines". In: *Journal of Engineering for Power* 84 (1962), pp. 83–102. URL: https://api.semanticscholar.org/CorpusID:110879337.

[17] NASA. *SP-290: Turbine Design and Application*. Tech. rep. NASA, 1972.

[18] SoftInWay. *Role of AxSTREAM in Radial Turbine Design*. URL: https://blog.softinway.com/role-of-axstream-in-radial-turbine-design/ (visited on 09/15/2024).

[19] Emiliano Casati et al. "Centrifugal Turbines for Mini-Organic Rankine Cycle Power Systems". In: *Journal of Engineering for Gas Turbines and Power* 136 (July 1, 2014), 122607 (11 pages). DOI: 10.1115/1.4027904.

[20] Alessandro Cappiello et al. "On the Influence of Stator-Rotor Radial Gap Size on the Fluid-Dynamic Performance of Mini-ORC Supersonic Turbines". In: *Volume 10B: Turbomachinery — Axial Flow Turbine Aerodynamics; Deposition, Erosion, Fouling, and Icing; Radial Turbomachinery Aerodynamics*. ASME Turbo Expo 2022: Turbomachinery Technical Conference and Exposition. Rotterdam, Netherlands: American Society of Mechanical Engineers, June 13, 2022, V10BT35A015. ISBN: 978-0-7918-8610-6. DOI: 10.1115/GT2022-83309. URL: https://asmedigitalcollection.asme.org/GT/proceedings/GT2022/86106/V10BT35A015/1149283 (visited on 09/09/2024).

[21] S.L. Dixon and C.A. Hall. "Chapter 8 - Radial Flow Gas Turbines". In: *Fluid Mechanics and Thermodynamics of Turbomachinery (Sixth Edition)*. Ed. by S.L. Dixon and C.A. Hall. Sixth Edition. Boston: Butterworth-Heinemann, 2010, pp. 265–302. ISBN: 978-1-85617-793-1. DOI: https://doi.org/10.1016/B978-1-85617-793-1.00008-0. URL: https://www.sciencedirect.com/science/article/pii/B9781856177931000080.

[22] Latitude. *LinkedIn Post*. URL: https://www.linkedin.com/posts/latitude-eu_turbopump-rocketengine-components-activity-7175768548563144704-hUcr?utm_source=share&utm_medium=member_desktop (visited on 09/15/2024).

[23] Astron Systems. *Aurora*. URL: https://astronsystems.com/aurora.jsp (visited on 08/23/2025).

[24] Astron Systems. *LinkedIn Post*. URL: https://www.linkedin.com/posts/astron-systems_hardware-highlight-rocket-engine-turbopump-activity-7361053252538228736-ggEy?utm_source=social_share_send&utm_medium=member_desktop_web&rcm=ACoAADeOguQBP5pHnhiur0_vfKe9nndJkUWTo3s (visited on 08/23/2025).

[25] Davide Cozzi et al. "Potential of Radial Turbines in Liquid Rocket Engines: a comparative study with classical axial Turbines". In: *Proceedings of the 74th International Astronautical Congress (IAC)*. IAC-24,C4,IP,88,x84628. Milan, Italy: American Society of Mechanical Engineers, 2024. URL: https://iafastro.directory/iac/archive/browse/IAC-24/C4/IP/84628/ (visited on 09/09/2024).

[26] Angelo Leto and Aldo Bonfiglioli. "Preliminary Design of a Radial Turbine for Methane Expander Rocket-Engine". In: *Energy Procedia*. ATI 2017 - 72nd Conference of the Italian Thermal Machines Engineering Association 126 (Sept. 1, 2017), pp. 738–745. ISSN: 1876-6102. DOI: 10.1016/j.egypro.2017.08.221. URL: https://www.sciencedirect.com/science/article/pii/S1876610217337 27X (visited on 09/15/2024).

[27] Aki Grönman and Antti Uusitalo. "Analysis of radial-outflow turbine design for supercritical CO2 and comparison to radial-inflow turbines". In: *Energy Conversion and Management* 252 (2022), p. 115089. ISSN: 0196-8904. DOI: https://doi.org/10.1016/j.enconman.2021.115089. URL: https://www.sciencedirect.com/science/article/pii/S0196890421012656.

[28] P. Drużdżel. *Fluid-dynamic characterisation of small- scale organic Rankine cycle radial-outflow turbine for renewable energy application*. Master's thesis. Available at https://repository.tudelft.nl/record/uuid:1ff626fb-177d-44b1-8095-091923eb8f3a. Delft, Jan. 2017.

[29] Enhua Wang and Ningjian Peng. "A Review on the Preliminary Design of Axial and Radial Turbines for Small-Scale Organic Rankine Cycle". In: *Energies* 16.8 (Jan. 2023). Number: 8, p. 3423. ISSN: 1996-1073. DOI: 10.3390/en16083423. URL: https://www.mdpi.com/1996-1073/16/8/3423 (visited on 10/03/2024).

[30] NASA. *SP-8110: Liquid Rocket Engine Turbines*. Tech. rep. NASA, 1974.

[31] Bhupinder Singh Sanghera et al. "Adjoint-Based Optimisation of Rocket Engine Turbine Blades". In: *Volume 2D: Turbomachinery — Multidisciplinary Design Approaches, Optimization, and Uncertainty Quantification; Radial Turbomachinery Aerodynamics; Unsteady Flows in Turbomachinery*. ASME Turbo Expo 2021: Turbomachinery Technical Conference and Exposition. Virtual, Online: American Society of Mechanical Engineers, June 7, 2021, V02DT36A013. ISBN: 978-0-7918-8493-5. DOI: 10.1115/GT2021-59580. URL: https://asmedigitalcollection.asme.org/GT/proceedings/GT2021/84935/V02DT36A013/1119822 (visited on 10/04/2024).

[32] CFturbo. URL: https://cfturbo.com (visited on 08/14/2024).

[33] Lehner Motoren. *LMT 3060*. URL: https://www.lehner-shop.com/en/inrunner/series-30/3060 (visited on 09/10/2024).

[34] Trampa. *VESC 75 / 300 MKIV*. URL: https://trampaboards.com/vesc-75v-300a-black-anodised-non-conductive-cnc-housing--350-each-p-36236.html (visited on 10/02/2024).

[35] Dominic Campbell-Pitt, Atanas Dzhurkov, and Jakub Maszkowski. *Electronics Summary*. Tech. rep. Stratos V, Delft Aerospace Rocket Engineering, Dec. 2023.

[36] SMC Racing. *Company Website*. URL: https://www.smc-racing.com (visited on 07/23/2025).

[37] *LinkedIn: Mario Hernández Méndez*. URL: https://www.linkedin.com/in/mario-h-mendez/.

[38] *X: Mario Hernandez*. URL: https://x.com/AStarryDawn (visited on 08/03/2024).

[39] Joseph F. Wasserbauer and William Tabata. *Performance of small (100-lb thrust) rocket motors using coaxial injection of hydrazine and nitrogen tetroxide*. Tech. rep. TN D-1162. Cleveland, Ohio: NASA Lewis Research Center, Dec. 1961, p. 27. URL: https://ntrs.nasa.gov/citations/19980227821.

[40] Samuel Stein. *A HIGH -PERFORMANCE 250-POUND-THRUST ROCKET ENGINE UTILIZING COAXIAL-FLOW INJECTION OF JP-4 FUEL AND LIQUID OXYGEN*. Tech. rep. TN D-126. Cleveland, Ohio: NASA Lewis Research Center, Oct. 1959, p. 14. URL: https://babel.hathitrust.org/cgi/pt?id=uiug.30112106742346&view=1up&seq=10.

[41] Raphael Timbó et al. "ROSS - Rotordynamic Open Source Software". In: *Journal of Open Source Software* 5.48 (2020), p. 2120. DOI: 10.21105/joss.02120. URL: https://doi.org/10.21105/joss.02120.

[42] Tobias Traudt et al. "LUMEN Turbopump - Status of the Development and Testing". In: Mar. 2021.

[43] Tobias Traudt et al. "Status of the Turbopump Development in the LUMEN Project". In: Oct. 2018.

[44] Robson Henrique dos Santos Hahn et al. "LUMEN Turbopump - Preliminary Design of Supersonic Turbine". In: June 2019.

[45] Mateusz T. Gulczyński et al. "Turbine Blades for Reusable Liquid Rocket Engines (LRE) - Numerical Fatigue Life Investigation". In: *2023 IEEE Aerospace Conference*. 2023, pp. 1–11. DOI: 10.1109/AERO55745.2023.10115912.

[46] Tobias Traudt et al. “LUMEN Turbopump -Design and Manufacturing of the LUMEN LOX and LNG Turbopump components”. In: June 2019.

[47] George Paul Sutton and Oscar Biblarz. *Rocket propulsion elements*. 7th. New York: John Wiley and Sons, 2001.

[48] SoftInWay. *AxSTREAM For Turbomachinery Design*. URL: https://www.softinway.com/software-solutions/turbomachinery-design/ (visited on 12/05/2024).

[49] Andrew Price et al. *Turbomachinery DTP-E45 Critical Design Review*. Tech. rep. 2025.

[50] E. W. Lemmon et al. *NIST Standard Reference Database 23: Reference Fluid Thermodynamic and Transport Properties-REFPROP, Version 10.0, National Institute of Standards and Technology*. 2018. DOI: https://doi.org/10.18434/T4/1502528. URL: https://www.nist.gov/srd/refprop.

[51] Oscar Junius et al. *Stratos V DLX-150C Design Report*. Tech. rep. Stratos V, Delft Aerospace Rocket Engineering, Apr. 2023.

[52] S. Trollheden et al. “Development of the turbines for the Vulcain 2 turbopumps”. In: *35th Joint Propulsion Conference and Exhibit*. DOI: 10.2514/6.1999-2342. eprint: https://arc.aiaa.org/doi/pdf/10.2514/6.1999-2342. URL: https://arc.aiaa.org/doi/abs/10.2514/6.1999-2342.

[53] Ulf Wahlen. “The aerodynamic design of the turbines for the Vulcain rocket engine”. In: *31st Joint Propulsion Conference and Exhibit*. DOI: 10.2514/6.1995-2536. eprint: https://arc.aiaa.org/doi/pdf/10.2514/6.1995-2536. URL: https://arc.aiaa.org/doi/abs/10.2514/6.1995-2536.

[54] SpaceX. *Space Exploration Technologies Corp.* https://www.spacex.com. Accessed: 2025-07-16. 2025.

[55] European Space Agency. *Ariane 6’s Vulcain engine set for first firing*. 2017. URL: https://www.esa.int/Enabling_Support/Space_Transportation/Ariane/Ariane_6_s_Vulcain_engine_set_for_first_firing (visited on 06/21/2025).

[56] *Van Der Lee Turbo Systems*. URL: https://www.vdlee.com.

[57] RocketCEA. *RocketCEA Wraps The NASA FORTRAN CEA Code And Provides Some Useful Tools*. URL: https://rocketcea.readthedocs.io/en/latest/ (visited on 12/05/2024).

[58] Bonnie J. Mcbride and Sanford Gordon. *Computer program for calculating and fitting thermodynamic functions*. NTRS Author Affiliations: NASA Lewis Research Center, Gordon, Sanford, Cleveland NTRS Report/Patent Number: E-5894 NTRS Document ID: 19930003779 NTRS Research Center: Legacy CDMS (CDMS). Nov. 1, 1992. URL: https://ntrs.nasa.gov/citations/19930003779 (visited on 12/05/2024).

[59] Violette Mounier, Luis Eric Olmedo, and Jürg Schiffmann. “Small scale radial inflow turbine performance and pre-design maps for Organic Rankine Cycles”. In: *Energy* 143 (Jan. 2018), pp. 1072–1084. ISSN: 0360-5442. DOI: 10.1016/j.energy.2017.11.002. URL: https://www.sciencedirect.com/science/article/pii/S0360544217318510 (visited on 11/21/2024).

[60] R.J.G. Hermsen. *Cryogenic propellant tank pressurization*. Master’s thesis. Available at https://resolver.tudelft.nl/uuid:048e34e9-9af6-4b3c-9249-576d192fa7bd. Delft, June 2017.

[61] Resolute Cylinders. *Carbon Fiber Cylinders*. URL: https://resolutecylinders.com/service/carbon-fiber-cylinders/ (visited on 07/09/2025).

[62] TUDIVING. *Competitive Price Long-Term Use High Pressure 9L 300bar 4500psi 30mpa PCP Paintball Scuba Diving Carbon Fiber Air Tank*. URL: https://www.alibaba.com/product-detail/GP-High-Pressure-9L-300bar-4500psi_1600655648052.html?spm=a2700.galleryofferlist.normal_offer.d_title.75615b5e66VoUD (visited on 07/09/2025).

[63] TUXING. *Factory Wholesale Customized 6.8L 30mpa 300bar 4500psi HPA Breathing Compressed Gas Bottle Cylinder Carbon Fiber Air Tank*. URL: https://www.alibaba.com/product-detail/TUXING-High-Pressure-6-8L-4500psi_60612647806.html?spm=a2700.galleryofferlist.normal_offer.d_title.75615b5e66VoUD (visited on 07/09/2025).

[64] ARMOTECH. *Product catalogue: high pressure composite cylinders*. URL: http://www.armotech.cz/files/armotech-catalog.pdf (visited on 07/09/2025).

[65] Alsafe. *Hydrogen Storage Cylinder*. URL: https://www.alsafechina.com/html/product/show/?id=182 (visited on 07/09/2025).

[66] Luxfer. *Soecification Tables*. URL: https://www.luxfercylinders.com/specifications/ (visited on 07/09/2025).

[67] AMS Composite Cylinders. *Lightweight Composite Gas Cylinders*. URL: https://ams-composites.com/lightweight-carbon-composite-cylinders/ (visited on 07/09/2025).

[68] Alsafe. *Hydrogen Storage Cylinder*. URL: https://www.alsafechina.com/html/product/show/?id=182 (visited on 07/09/2025).

[69] Giovani H. Ceotto et al. "RocketPy: Six Degree-of-Freedom Rocket Trajectory Simulator". In: *Journal of Aerospace Engineering* 34.6 (Aug. 2021). DOI: 10.1061/(ASCE)AS.1943-5525.0001331. URL: https://github.com/github/linguist.

[70] RocketPy. *Flight simulated with RocketPy*. URL: https://docs.rocketpy.org/en/latest/examples/index.html (visited on 07/23/2025).

[71] Charles E. Rogers and David Cooper. *Rogers Aeroscience RASAero Aerodynamic Analysis and Flight Simulation Software*. URL: https://www.rasaero.com (visited on 07/05/2025).

[72] K. L. Eppenga. *Necessity of non-rigid body models for launch vehicles*. Master's thesis. Available at https://repository.tudelft.nl/record/uuid:4dc937c1-819e-4801-afe4-f654b03dce65. Delft, May 2021.

[73] Rolf Wubben et al. *Investigation of the In-Flight Failure of the Stratos III Sounding Rocket*. Proceedings of ISASI 2019 Conference. Available from Delft Aerospace Rocket Engineering: https://dare.tudelft.nl/about/research/. Stevinweg 1, 2628 CN Delft, South Holland, The Netherlands, 2019.

[74] Aaron Bracke et al. *Stratos V: Systems Requirements*. Tech. rep. Nov. 2022.

[75] *Ansys® Academic Research CFX, Release 24.2*. Ansys Inc. 2024.

[76] *Ansys® Academic Research CFX, Release 24.2, CFX Solver Modelling Guide*. Ansys Inc. 2024.

[77] *Ansys® Academic Research TurboGrid, Release 24.2*. Ansys Inc. 2024.

[78] *Ansys® Academic Research Meshing, Release 24.2*. Ansys Inc. 2024.

[79] Matteo Majer and Matteo Pini. "Design guidelines for high-pressure ratio supersonic radial-inflow turbines of organic rankine cycle systems". en. In: *Journal of the Global Power and Propulsion Society* 9 (Apr. 2025). Publisher: Global Power and Propulsion Society, pp. 19–46. ISSN: 2515-3080. DOI: 10.33737/jgpps/195437. URL: https://journal.gpps.global/Design-guidelines-for-high-pressure-ratio-supersonic-radial-inflow-turbines-of-organic,195437,0,2.html (visited on 07/19/2025).

[80] Piotr Lampart. "Tip leakage flows in turbines". In: *TASK QUARTERLY* 10 (Jan. 2006), pp. 139–175.

A

Full System-Level Trade Study Results

The full results of the system-level trade study are presented in this appendix. In Section A.1 the results of the pressure-fed cycle are shown, for two different assumptions of ullage temperature (90 K and 150 K). The results for the pump-fed cycle are shown in Section A.2. Finally, the results for the turbopump-fed cycle using the relations from AxStream and Mounier et al. are shown in Section A.3 and Section A.4, respectively. The results in the former are identical to those presented in Chapter 5, but duplicated here for easier comparison.

A.1. Pressure-Fed Cycle

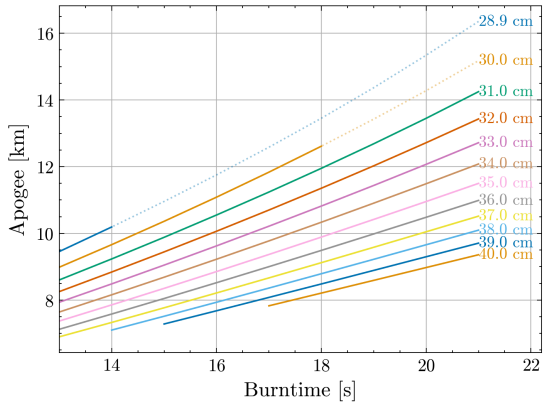

(a) Simulated apogee as a function of burntime, for varying rocket diameters. Dotted lines represent the apogee achieved without limitations, whereas solid lines are limited by the imposed TEV and LD ratio requirements.

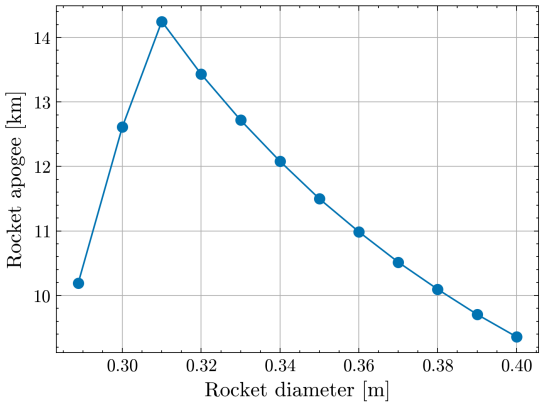

(b) Maximum simulated apogee as a function of rocket diameter.

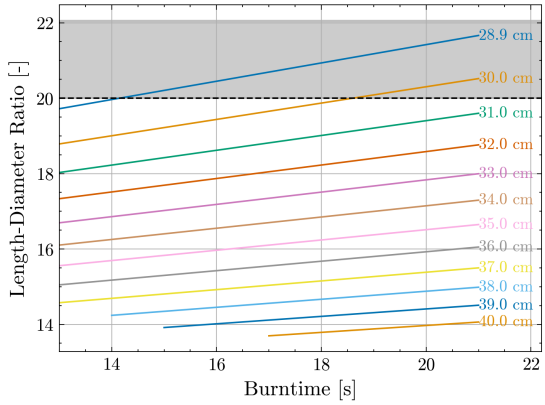

(c) LD ratio as a function of burntime, for varying rocket diameters. The grey area represents the maximum LD ratio requirement of 20.

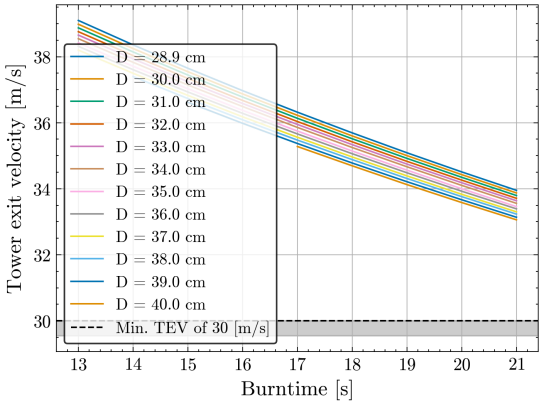

(d) Tower exit velocity (TEV) as a function of burntime, for varying rocket diameters. The grey area represents the minimum TEV requirement of 30 m/s.

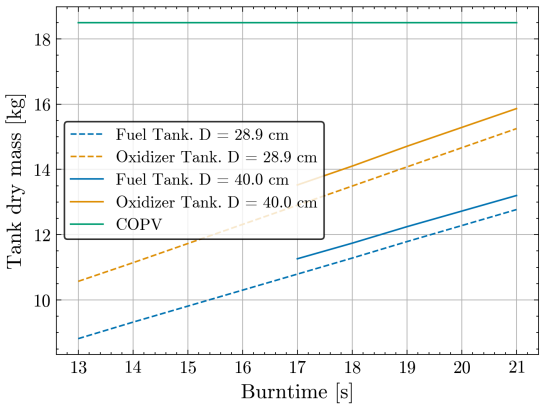

(e) Tank dry masses as a function of burntime, for varying rocket diameters.

Figure A.1: System-level trade study results for the pressure-fed rockets, with an assumed LOx tank ullage temperature of 90 K.

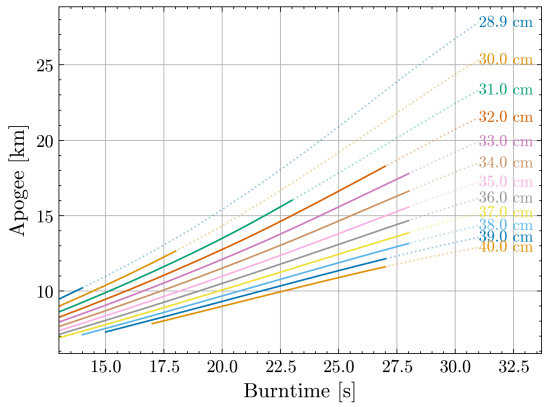

(a) Simulated apogee as a function of burntime, for varying rocket diameters. Dotted lines represent the apogee achieved without limitations, whereas solid lines are limited by the imposed TEV and LD ratio requirements.

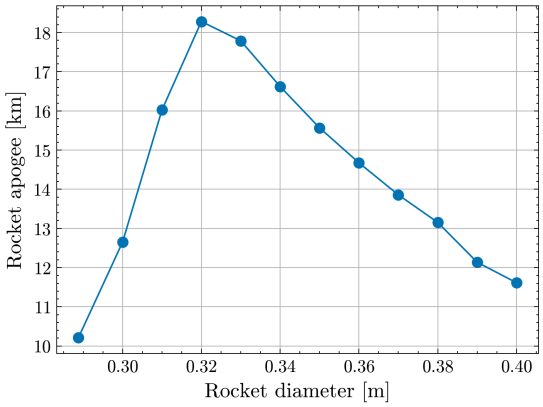

(b) Maximum simulated apogee as a function of rocket diameter.

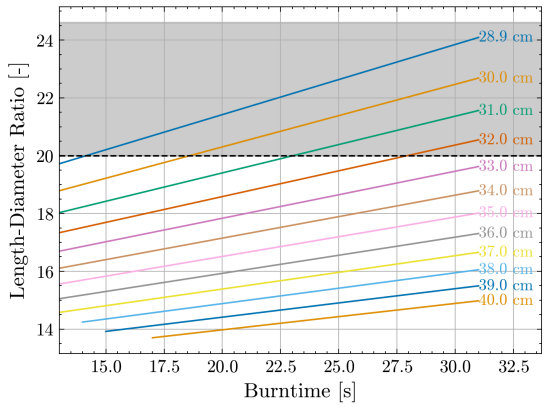

(c) LD ratio as a function of burntime, for varying rocket diameters. The grey area represents the maximum LD ratio requirement of 20.

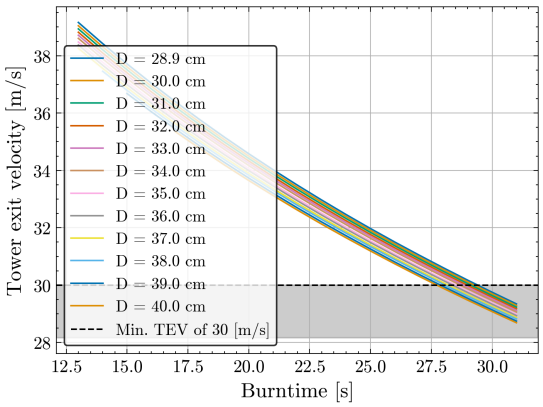

(d) Tower exit velocity (TEV) as a function of burntime, for varying rocket diameters. The grey area represents the minimum TEV requirement of 30 m/s.

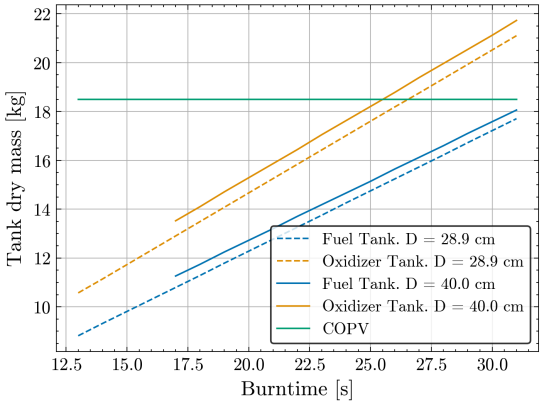

(e) Tank dry masses as a function of burntime, for varying rocket diameters.

Figure A.2: System-level trade study results for the pressure-fed rockets, with an assumed LOx tank ullage temperature of 150 K.

A.2. Electric Pump-Fed Cycle

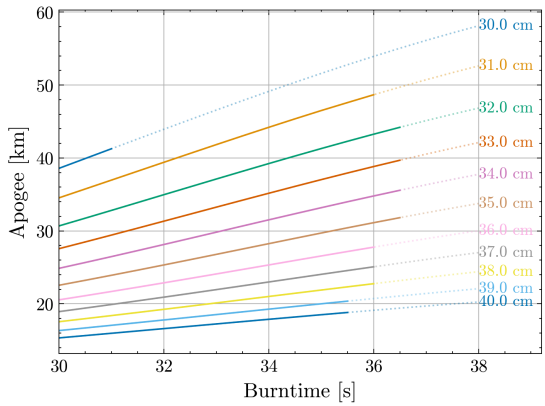

(a) Simulated apogee as a function of burntime, for varying rocket diameters. Dotted lines represent the apogee achieved without limitations, whereas solid lines are limited by the imposed TEV and LD ratio requirements.

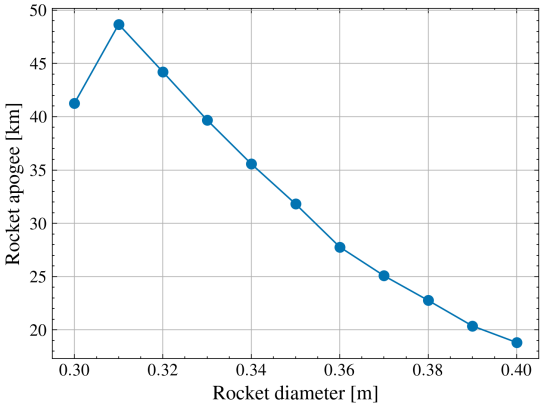

(b) Maximum simulated apogee as a function of rocket diameter.

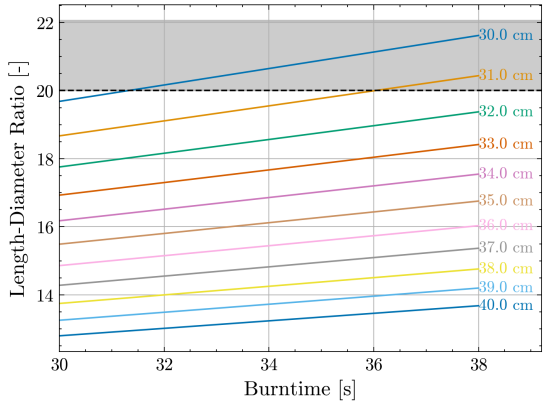

(c) LD ratio as a function of burntime, for varying rocket diameters. The grey area represents the maximum LD ratio requirement of 20.

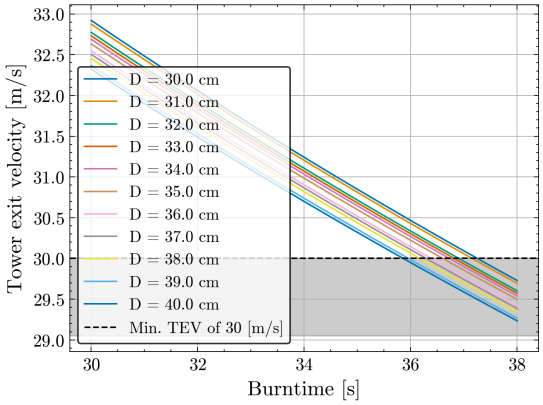

(d) Tower exit velocity (TEV) as a function of burntime, for varying rocket diameters. The grey area represents the minimum TEV requirement of 30 m/s.

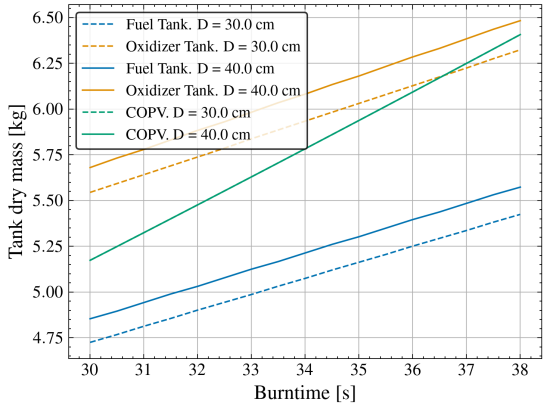

(e) Tank dry masses as a function of burntime, for varying rocket diameters.

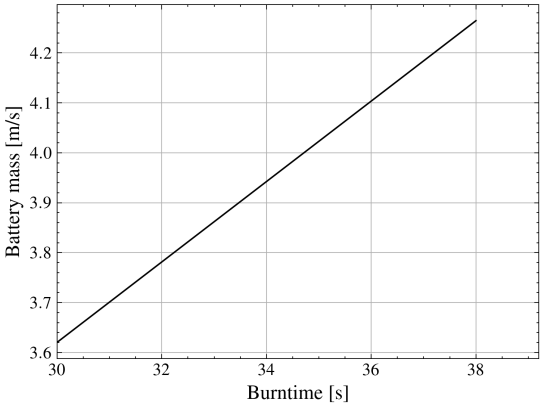

(f) Estimated battery mass as a function of rocket diameter.

Figure A.3: System-level trade study results for the electric pump-fed rockets.

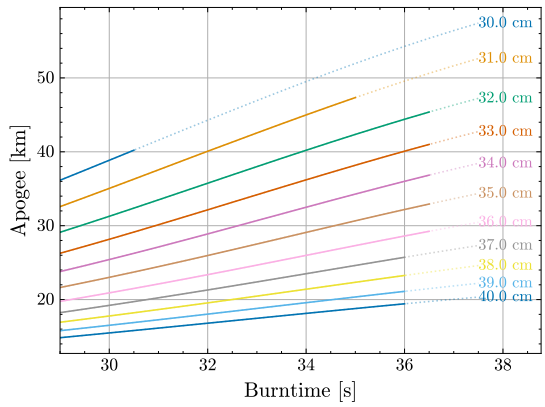

(a) Simulated apogee as a function of burntime, for varying rocket diameters. Dotted lines represent the apogee achieved without limitations, whereas solid lines are limited by the imposed TEV and LD ratio requirements.

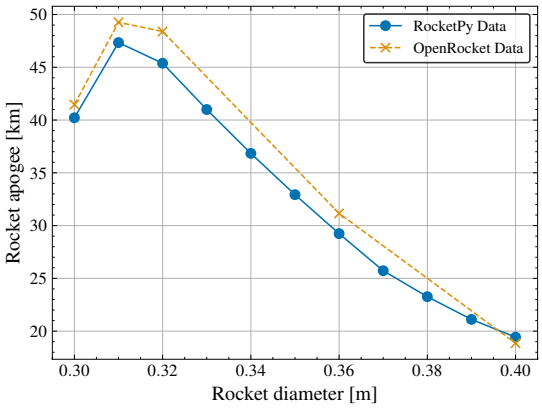

(b) Maximum simulated apogee as a function of rocket diameter, with verification data obtained through OpenRocket.

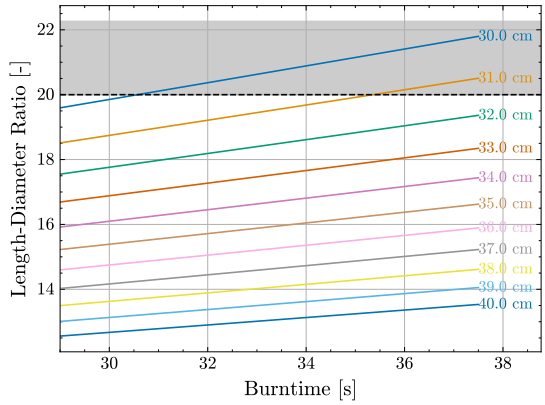

(c) LD ratio as a function of burntime, for varying rocket diameters. The grey area represents the maximum LD ratio requirement of 20.

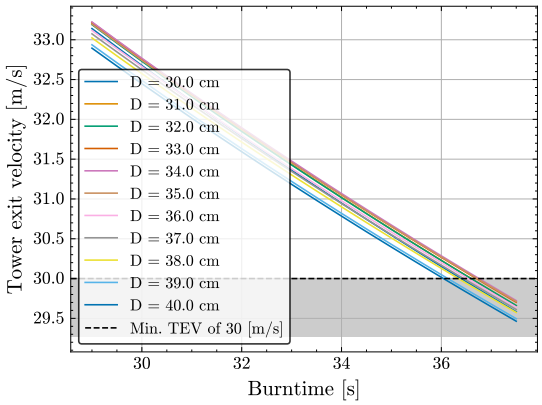

(d) Tower exit velocity (TEV) as a function of burntime, for varying rocket diameters. The grey area represents the minimum TEV requirement of 30 m/s.

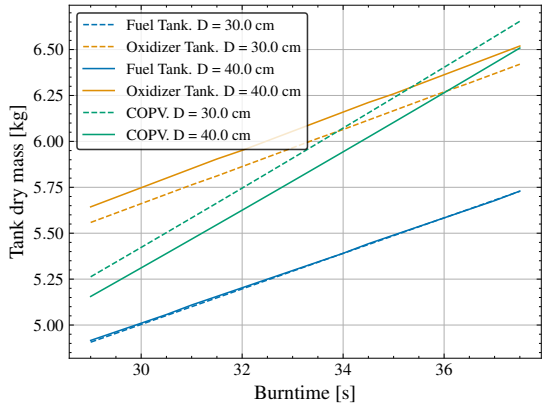

(e) Tank dry masses as a function of burntime, for varying rocket diameters.

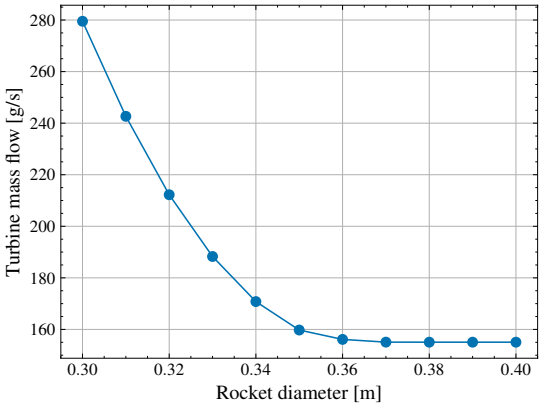

(f) Estimated turbine mass flow as a function of rocket diameter (AxStream).

Figure A.4: System-level trade study results for the turbopump-fed rockets, using the relations obtained through AxStream.

A.3. Turbopump-Fed Cycle: AxStream-based

A.4. Turbopump-Fed Cycle: Mounier-based

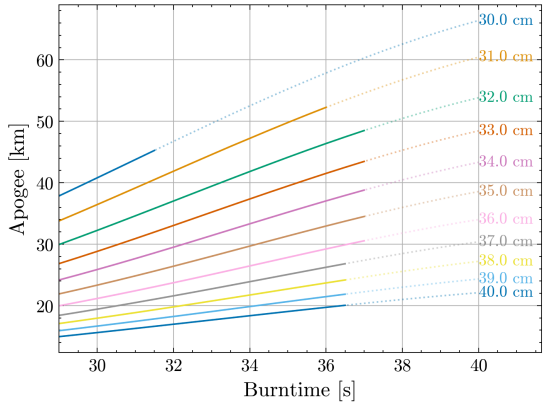

(a) Simulated apogee as a function of burntime, for varying rocket diameters. Dotted lines represent the apogee achieved without limitations, whereas solid lines are limited by the imposed TEV and LD ratio requirements.

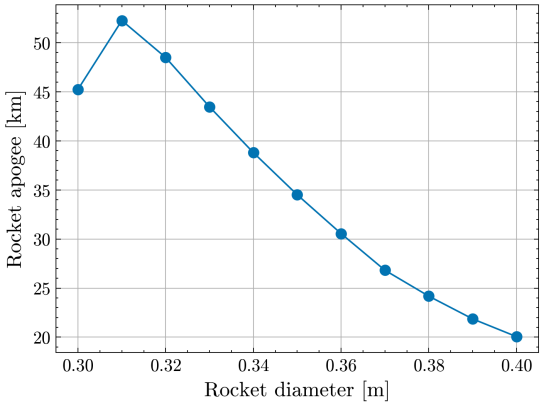

(b) Maximum simulated apogee as a function of rocket diameter.

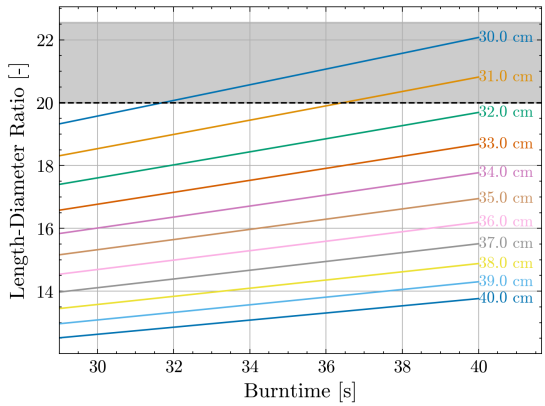

(c) LD ratio as a function of burntime, for varying rocket diameters. The grey area represents the maximum LD ratio requirement of 20.

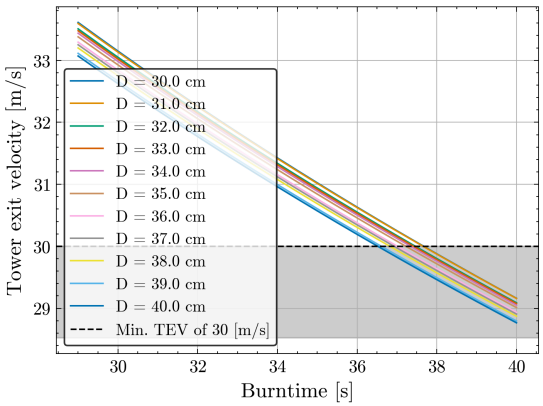

(d) Tower exit velocity (TEV) as a function of burntime, for varying rocket diameters. The grey area represents the minimum TEV requirement of 30 m/s.

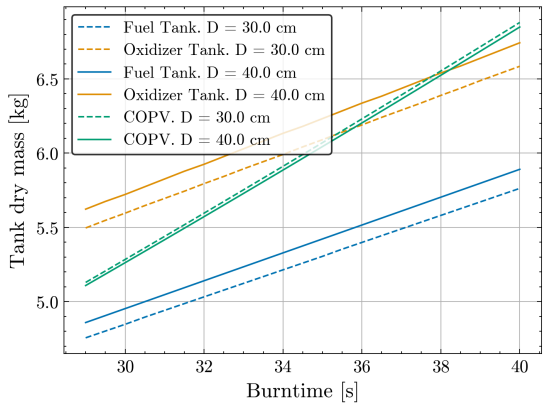

(e) Tank dry masses as a function of burntime, for varying rocket diameters.

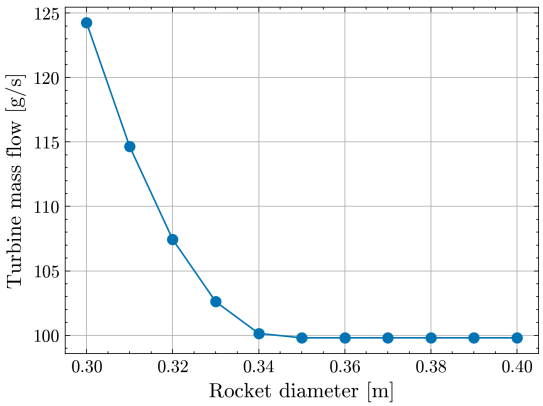

(f) Estimated turbine mass flow as a function of rocket diameter (Mounier et al.).

Figure A.5: System-level trade study results for the turbopump-fed rockets, using the relations obtained through Mounier et al.'s methods.